

Review

Infrared Spectral Energy Distribution and Variability of Active Galactic Nuclei: Clues to the Structure of Circumnuclear Material

Jianwei Lyu *  and George Rieke * 

Steward Observatory, University of Arizona, 933 North Cherry Avenue, Tucson, AZ 85721, USA

* Correspondence: jianwei@arizona.edu (J.L.); grieke@arizona.edu (G.R.)

Abstract: The active galactic nucleus (AGN) phenomenon results from a supermassive black hole accreting its surrounding gaseous and dusty material. The infrared (IR) regime provides most of the information to characterize the dusty structures that bridge from the galaxy to the black hole, providing clues to the black hole growth and host galaxy evolution. Over the past several decades, with the commissioning of various ground, airborne and space IR observing facilities, our interpretations of the AGN circumnuclear structures have advanced significantly through an improved understanding of how their dust emission changes as a function of wavelength and how the heating of the dusty structures responds to variations in the energy released from the central engine. In this review, we summarize the current observational knowledge of the AGN IR broad-band spectral energy distributions (SEDs) and the IR time variability behavior covering large ranges of AGN luminosity and redshift, and discuss some first-order insights into the obscuring structures and host galaxy IR properties that can be obtained by integrating the relevant observations into a coherent picture.

Keywords: active galactic nuclei; dust continuum emission; spectral energy distribution; reverberation mapping; Seyfert galaxies; quasars; AGN host galaxies; IR galaxies; IR astronomy; time domain astronomy



Citation: Lyu, J.; Rieke, G. Infrared Spectral Energy Distribution and Variability of Active Galactic Nuclei: Clues to the Structure of Circumnuclear Material. *Universe* **2022**, *8*, 304. <https://doi.org/10.3390/universe8060304>

Academic Editors: Anna Sajina and Asantha R. Cooray

Received: 22 April 2022

Accepted: 24 May 2022

Published: 27 May 2022

Publisher's Note: MDPI stays neutral with regard to jurisdictional claims in published maps and institutional affiliations.



Copyright: © 2022 by the authors. Licensee MDPI, Basel, Switzerland. This article is an open access article distributed under the terms and conditions of the Creative Commons Attribution (CC BY) license (<https://creativecommons.org/licenses/by/4.0/>).

1. Introduction

Stars and supermassive black holes (SMBHs) in the form of active galactic nuclei (AGNs) are the two main sources of radiation energy in the Universe. Our understanding of stars stands on a foundation (the Russell–Vogt Theorem) that their properties to first order depend only on the initial composition, mass, and age. AGNs, at least with our current understanding, are more complex. Unification theories relate the different manifestations of this phenomenon into a general picture. However, the variety of observable properties at all spatial scales and wavelength ranges can differ significantly in ways not predicted *a priori* by theory, nor is their evolution well understood.

A number of reviews of the AGN phenomenon have focused on separate aspects. For example, Ulrich et al. [1] focus on the time variability of their outputs; Alexander & Hickox [2] address the vexing issue of how supermassive black holes (SMBHs) grow to their immense masses; Heckman & Best [3] discuss the interactions between the evolution of host galaxies and their SMBHs; Netzer [4] discuss the unified model, largely from a theoretical perspective; Padovani et al. [5] present a discussion of the unified model across the entire electromagnetic spectrum, with emphasis on the observational parameters; Ramos Almeida & Ricci [6] describe the current understanding of how obscuration by circumnuclear material alters the observable parameters of AGNs; Hickox & Alexander [7] discuss AGNs that are heavily obscured by or even embedded in dense clouds of interstellar gas and dust; Lacy & Sajina [8] focus on the advances in understanding AGNs made with the *Spitzer* Space Telescope; and Cackett et al. [9] review the reverberation mapping technique, where time delays in variations in different AGN components provide insights

into the structure—they focus largely on the X-ray, UV, optical, and broad line regions (BLRs), where this technique has been applied extensively.

Where does this review fit in? The central engines of AGNs are surrounded by a complex set of gaseous and dusty structures, which affect the appearance of the AGN in virtually every direction. In addition, these structures trace the inflows and outflows of material to the central engine, providing important clues to the growth of the central SMBH and its relation with the host galaxy. This review summarizes how our knowledge of these structures has grown through extensive infrared (IR) observations and synthesizes the current understanding into a coherent picture. As a guide, Figure 1 gives an overview of the relevant structures that can contribute to the AGN IR emission across different wavelengths, along with their relative scales, as inferred from various current observations. Figure 2 zeros in on the possible dusty structures in the immediate region of the central engine of the AGN, whose observed empirical properties and their immediate implications will occupy much of our discussion.

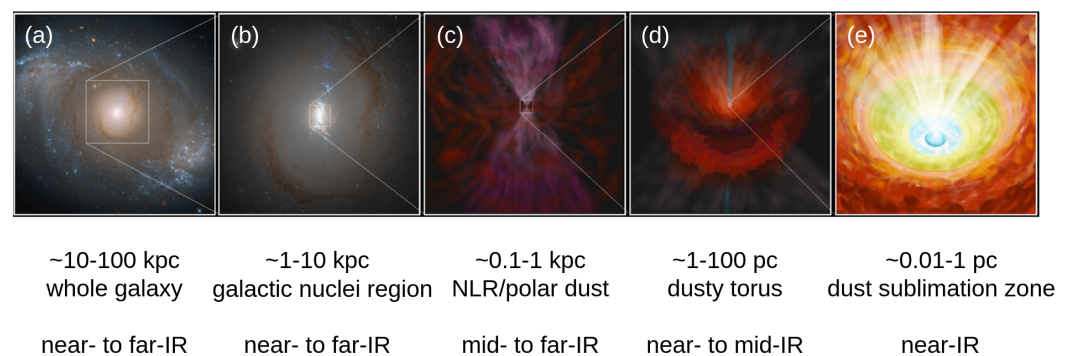


Figure 1. Illustration of various components that can contribute to the AGN IR emission at different scales, with the archetypal AGN in NGC 4151 as an example. From the left to right, Panel (a): NGC 4151 galaxy image from HST. * Stars contribute the near-IR ($1 < \lambda < 5 \mu\text{m}$) emission and HII regions can emit strongly in the mid-IR ($5 < \lambda < 30 \mu\text{m}$) and far-IR ($30 < \lambda < 500 \mu\text{m}$). Panel (b): the inner 5 kpc region of NGC 4151 as revealed by HST WFC3 images. * We can directly see the narrow-line-region (NLR) clouds near the central bright AGN, projecting along two directions, as well as two dust lanes and numerous small dust streams at different locations. Panel (c): schematic of the dust components at 1 kpc scale, featuring the NLR and polar dust in the AGN ionization cone. Outside this cone, relatively cool dust is shielded by the torus from the direct heating of the AGN. Panel (d): schematic of the dust structures at ~ 1 –100 pc scale, featuring a flared torus with possible turbulent/outflowing signatures and winds feeding the region of the NLR, which often dominate the AGN-heated dust emission from 6 to 40 μm . We also indicate a sub-mm torus extension (the circumnuclear disk) on a ~ 40 –60 pc scale detected by ALMA around many AGNs [10], not observed in NGC 4151 because it is not readily accessible to ALMA. Panel (e): schematic of the innermost region of the torus over ~ 0.01 –1 pc scales, featuring a likely turbulent disk; here, dust grains of graphite and silicates can be heated to their sublimation temperatures of 1500–2500 K and 900–1000 K, respectively, resulting in the AGN hot dust emission peaking around 2–4 μm . Modified from a figure in Lyu & Rieke [11]. (*—figure modified based on the original version from https://commons.wikimedia.org/wiki/File:NGC_4151_-_HST.png, (accessed on 25 May 2022)).

The concepts illustrated in these two figures are largely based on studies of the AGN spectral energy distributions (SEDs) and time variability, with additional insights provided by IR interferometry and other spatially resolved observations of nearby objects. We organize this review around the first two approaches, with descriptions when appropriate of how interferometry has upset previous concepts and set the thought process on a new path. Section 2 summarizes the observed characteristics of AGN IR SEDs, including a brief history, our current ideas of the general AGN IR SED features as well as possible outliers, and some discussion of IR SED decomposition and the inferred host galaxy properties. Section 3 focuses on AGN IR dust reverberation mapping and time variability studies,

discussing the challenges and the results from various campaigns. Section 4 stresses the important role of AGN IR selection to complete the AGN census with an overview of selection techniques such as color–color diagrams, SED analysis, and time variability. We briefly integrate the various AGN IR observations discussed in this review to provide a synthesis of the constraints on the AGN dusty environment in Section 5.

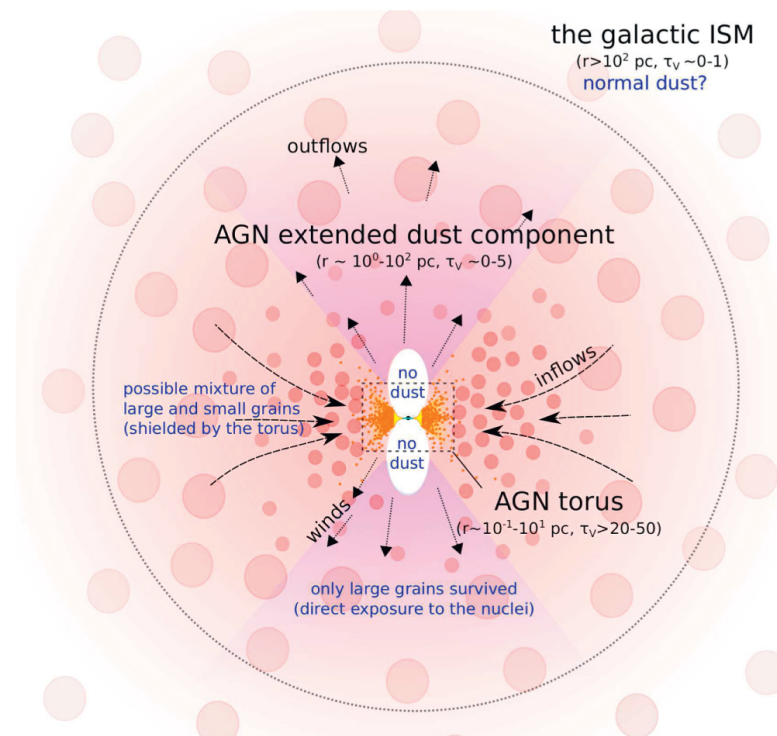


Figure 2. Cartoon illustration of the major IR-radiating components of a classical AGN [12]. The central engine and accretion disk are in the center, dwarfed in scale by the IR-emitting components. The circumnuclear “torus” is shown in cross-section and extends horizontally. We show it as a mixture of a clumpy and continuous distribution of gas and dust, heated by the emission of the accretion disk. The hottest dust, presumably of graphite, is at the inner edge of the torus, within which even carbon dust sublimates. Perpendicular and on either side of the torus, there are biconical outflows where the emission of the accretion disk can escape to excite emission lines. Dust in this region views the accretion disk directly. Close in, it is heated above its sublimation temperature and is destroyed, but further out, it can survive and is responsible for “polar dust emission” in the mid-IR. In all of these regions, the harsh environment imposed by the intense nuclear ultraviolet radiation [13], shocks [14], and sputtering due to hypersonic drift [15] probably modifies the distribution of dust grain sizes and hence the dust radiation properties.

To clarify our terminology, we use “AGN” in a general way to describe any active nucleus whose bolometric luminosity $L_{\text{bol}} \gtrsim 10^8 L_{\odot}$. “Quasar”¹ is reserved for the most energetic AGNs with $L_{\text{bol}} \gtrsim 10^{11} L_{\odot}$; the term by itself does not indicate if the nucleus is obscured or not. Relatively low-luminosity AGNs ($L_{\text{bol}} \sim 10^8\text{--}10^{11} L_{\odot}$) are termed “Seyfert nucleus/galaxy”. The word “torus” is adopted to describe the relatively compact, optically thick dusty structures that surround the BH accretion disk, although the real geometry can be very different from the classical donut cartoon. We describe the more extended structure in the same plane as the circumnuclear disk. “Polar dust” refers to the dust distribution in the AGN polar direction, including dusty winds launched from the torus as well as the more extended dusty NLRs. We define near-IR as $1 < \lambda < 5 \mu\text{m}$, mid-IR as $5 < \lambda < 30 \mu\text{m}$, and far-IR as $30 < \lambda < 500 \mu\text{m}$.

2. The IR Spectral Energy Distribution of AGNs

2.1. Origin of AGN IR Emission: Thermal or Nonthermal?

The first near- and mid-IR measurements of AGNs, in 1968, showed a roughly power-law spectrum rising steeply towards $\sim 20 \mu\text{m}$ (in the $\lambda - F_\nu$ space) [16]. In a prescient paper in 1969, Rees et al. [17] demonstrated that this behavior was consistent with the heating of circumnuclear dust through the absorption of emission by a nuclear source luminous in the optical and ultraviolet regions. Nonetheless, a nonthermal explanation for the IR emission thrived alongside the thermal one for around a decade, e.g., [18–20], bolstered by the roughly power-law IR spectral energy distributions. Rees et al. [17] derived a minimum timescale for IR variations under their hypothesis that the emission was the reradiation of nuclear energy by dust. The first measurements of IR variability, e.g., [21] suggested timescales in violation of this limit, but these measurements were very early in the development of IR astronomy and were subject to significant uncertainties.

When more complete and detailed IR photometry became available, it was apparent that the power-law SEDs were illusory, and nonthermal processes no longer needed to be invoked. The observations instead supported thermal models based on the emission from heated dust [22]. In 1981, Rieke & Lebofsky [23] reported detailed observations of NGC 4151 that confirmed the expected behavior from thermal models, including the role of hot graphite dust in the near-IR and the lack of variability at $10 \mu\text{m}$ on yearly timescales. In 1987, Barvainis [24] explained the $2 \mu\text{m}$ SED bump in quasar spectra as arising from the thermal emission of graphite dust heated to its sublimation temperature. Two years later, Clavel et al. [25] observed the expected phase lag between optical/UV variations and the IR response to them by heated dust at the expected \sim light months distance from the central engine. Hunt et al. [26] reported a search for fast timescale variations in the IR similar to those seen in the X-ray and concluded that there were none, i.e., the IR variations were consistent with reradiation by heated dust. The Infrared Astronomical Satellite (IRAS) established that many AGNs emit strongly in the far-IR, with SEDs similar to those of non-AGN star-forming galaxies, e.g., [27]. Given this resemblance and the large IRAS beams ($1.5' \times 4.7'$ at $60 \mu\text{m}$, $3' \times 5'$ at $100 \mu\text{m}$), this emission was attributed to the result of star formation in the AGN host galaxies.

These results were persuasive that dust heated by the central engine produces the majority of the near- and mid-IR emission for Seyfert galaxies, but that the far-IR probably was powered by young stars. However, the thermal/nonthermal ambiguity persisted for higher-luminosity AGNs, e.g., [1,28,29]. Neugebauer & Matthews [30] conducted variability monitoring of 25 quasars in the near-IR out to $10 \mu\text{m}$; variation at the latter wavelength would be a definitive demonstration that the emission was generated nonthermally. However, the signal to noise was inadequate for a definitive result. Thus, at the end of the twentieth century, the relative roles of the two classes of emission in various high-luminosity AGN types—radio loud/quiet, for example—were not clear. Nonetheless, it was clear that *all* AGNs have a distinctive near- and mid-IR SED compared to stars or normal galaxies, as we discuss below.

2.2. Behavior of AGN IR Emission. I: General Features

As discussed throughout this review, the form of an AGN SED is a product of how it is viewed and how dust is distributed around it. Type 1 AGNs, by definition viewed pole-on and avoiding heavy dust clouds, are not heavily obscured and hence define the intrinsic SED of this class of source. The general category of obscured AGNs is traditionally termed as Type 2 and defined as not having extremely broad ($\text{FWHM} \gtrsim 1000 \text{ km/s}$) permitted emission lines (e.g., $\text{H}\alpha$ and $\text{H}\beta$). This deficiency results from viewing the source from a perspective such that optically thick matter hides the central engine and the BLR. Spectroscopically intermediate cases are designated as Type 1.2–1.9. However, the obscured category is much larger, including many objects so obscured at visible wavelengths that they are too faint to obtain optical spectra.

2.2.1. Intrinsic Near- and Mid-IR SEDs

The near-IR SEDs of Type 1 AGNs were first determined reliably for high-luminosity AGNs, i.e., quasars, where the AGN emission is so strong that it overwhelms the stellar contribution in this spectral range [19]. Ward et al. [31] used CCD images to determine and subtract the galaxy contribution to the near-IR photometry of lower-luminosity AGNs, i.e., Seyfert galaxies. They showed that the variety of behavior was consistent with a single type of SED shape, modified by dust in the form of attenuation and IR emission. A classic paper led by Elvis [32] proposed a “standard” SED extending from the IR into the X-ray. As shown in Figure 3, which also shows examples from Richards et al. [33], Scott & Stewart [34], Shang et al. [35], subsequent determinations of the SED have been remarkably similar. This similarity extends to very high redshift, as shown by the quasar SED at $z \sim 5-6.5$ from Leipski et al. [36]. In the near-IR, the compendium of sub-arcsec measurements of Seyfert galaxies at L and M bands ($3.78 \mu\text{m}$ and $4.66 \mu\text{m}$, respectively) by Isbell et al. [37] separates the AGN from the galaxy contribution and allows the testing of this similarity for lower-luminosity AGNs. Although the wavelength separation of the two bands is too small and the signal to noise too low for a determination for each galaxy, a weighted average of the ratio of the L to M band fluxes for 22 Type 1 to 1.9 AGNs (cutting two with anomalously large ratios) is 0.9 in νf_ν , whereas the Elvis template predicts a ratio of 1.01, i.e., the agreement is excellent. In addition to these similar slopes, the rapid increase in the AGN near-SED near $2 \mu\text{m}$ (see Figure 2) is also seen generally. It is associated with the inner edge of the dusty circumnuclear torus, where graphite dust is heated to its sublimation temperature, e.g., [24,38]. That is, it appears that the shape of the AGN near-IR SEDs illustrated in Figure 3 is truly universal and insensitive to AGN luminosity or redshift. The SED shape at longer wavelengths presumably reflects the structure of this torus, although, as foreshadowed by the initial attribution of nonthermal emission to apparently power-law SEDs (as discussed in Section 2.1), the interpretations can be highly degenerate.

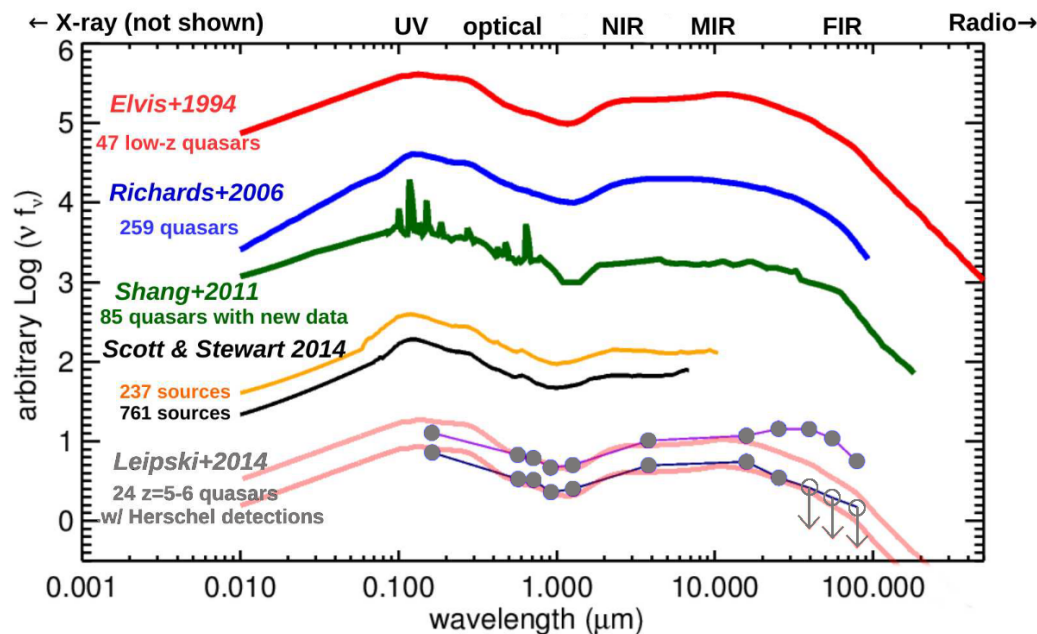


Figure 3. Comparison of empirical average SED templates derived for Type 1 quasars from Elvis et al. [32], Richards et al. [33], Shang et al. [35], and Scott & Stewart [34], as well as the averaged SEDs of $z \sim 5-6.5$ quasars with *Herschel* detections from Leipski et al. [36].

Nonetheless, there is some variation in this pattern for a modest number of AGNs. One notable example is the “dust-free” quasars reported firstly at $z \sim 6$ [39], with SEDs that have a nearly flat continuum from the optical to the mid-IR. However, these objects are not exclusive to very high redshift, e.g., [40]. A comprehensive study of the AGN intrinsic IR SED variations [41] proposes categories of hot-dust-deficient (HDD: weak emission

throughout the near- and mid-IR) and warm-dust-deficient (WDD: weak emission in the mid-IR but similar to those in Figure 3 in the near-IR), which contrast with normal quasars (e.g., those plotted in Figure 3). Figure 4 illustrates the SED characteristics of these types. Reverberation mapping shows that the near-IR output of even the most extreme HDD quasars is largely due to reradiation of the nuclear emission by hot dust [42], i.e., their behavior reflects differences in torus structure, not a change in radiation mechanism. Lyu et al. [41] conclude that the HDD quasars constitute $\sim 15\text{--}20\%$ of an IR unbiased sample. Later in this review, we will suggest that the “normal” category represents an average over all categories, with the HDD and WDD cases as subtypes within this average. There have also been suggestions of systematic intrinsic differences in the circumnuclear tori among Type 1 and Type 2 AGNs (thus, their intrinsic SEDs are consequently different), but these claims must be assessed cautiously given the potential for selection biases [43].

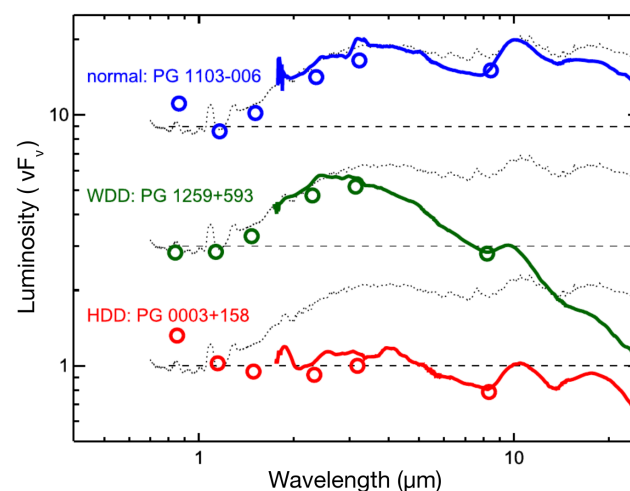


Figure 4. Near- to mid-IR spectra (solid lines) and photometry (open circles) for three representative Palomar–Green (PG) quasars to illustrate the variations in AGN intrinsic IR emission [41]. From top to bottom, PG 1103-006 is a “normal” AGN, PG 1259+593 is WDD, and PG 0003+158 is HDD. The dotted lines are the average, i.e., “normal” spectral templates for quasars compiled from the literature, as in Figure 3.

2.2.2. Obscured SEDs

Another key aspect in understanding the AGN near- to mid-IR emission is the attenuation by dust. Although some low to moderate extinction occurs for many AGNs, strong attenuation is characteristic of Type 2 or obscured AGNs.² In many cases, the galaxy stellar emission dominates the near-IR for Type 2 objects, e.g., [44], making the characterization of the AGN-heated SED behavior at these wavelengths very challenging. Two approaches are used. The first, useful at low- z , is to isolate the nuclear emission from that of the host galaxy with high spatial resolution. For example, Prieto et al. [45] present arcsec-resolution SEDs of some of the nearest Seyfert-2 galaxies, Circinus, NGC 1068, NGC 5506, NGC 7582, and build an average template for Seyfert-2 nuclei. Alonso-Herrero et al. [46] and Videla et al. [47] characterize the AGN SEDs at $\sim 1\text{--}15\ \mu\text{m}$ for a larger sample (dozens of objects) with the aid of imaging decomposition (as well as some SED decomposition). Alternatively, studies have focused on the very bright obscured quasar population at high- z , where the galaxy contamination is relatively weak. This approach includes, e.g., the torus template in the SWIRE library [48], based on *Spitzer* measurements of a heavily obscured but very luminous AGN at $z \sim 2.5$ [49], and average SEDs of IR bright AGNs ($L_{\text{IR}} \sim 10^{12}\text{--}10^{13} L_{\odot}$) based on a sample of ~ 12 obscured quasars with *Spitzer* and *Herschel* observations [50].

In the left panel of Figure 5, we show the obscured AGN IR SEDs from these works [45,47,49,50], including the average SED of the so-called hot-dust-obscured galaxies, which are believed to host the most luminous obscured AGNs [51]. Compared to the unobscured intrinsic AGN template, the SEDs of the obscured AGNs have weaker

emission, with the discrepancy increasing quickly toward shorter wavelengths. The differences are even noticeable in the mid-IR up to $\sim 10\text{--}20\ \mu\text{m}$, as evidenced by the silicate absorption features at ~ 10 and $\sim 18\ \mu\text{m}$.

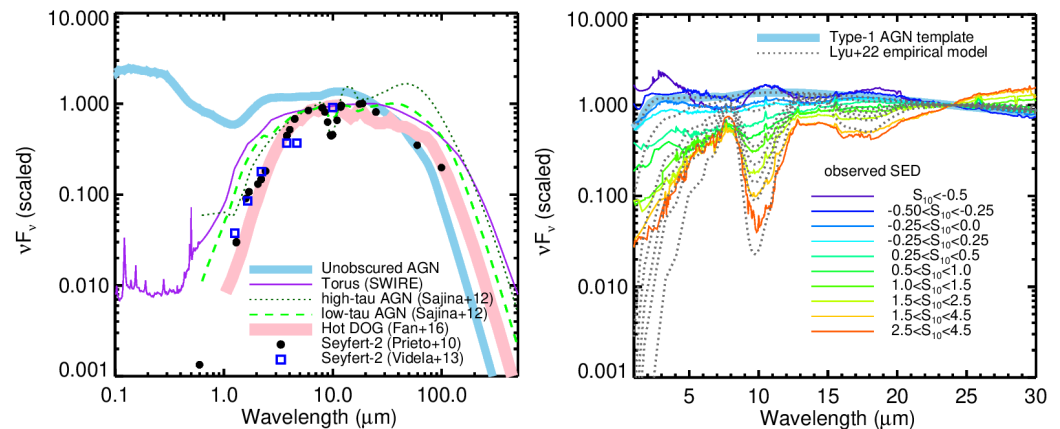


Figure 5. (Left): Type 2 AGN SEDs derived in the literature, including the average SEDs of Seyfert-2 nuclei derived by Prieto et al. [45] and Videla et al. [47], the torus template in the SWIRE library [49], the IR SED templates for high- $\tau_{9.7}$ and low- $\tau_{9.7}$ ($\tau_{9.7}$, respectively, $>$ and $<$) IR bright quasars from Sajina et al. [50], and the average SED of hot-dust-obscured galaxies from Fan et al. [51]. The SED template of unobscured AGNs from Elvis et al. [32], Xu et al. [52] is also presented as a comparison. (Right): The IR SEDs of obscured AGNs at 2–30 μm . We have computed the average SEDs of AGNs with different 10 μm silicate feature strength ($S_{10} = \log(F_{\text{obs.}}/F_{\text{cont.}}) = -0.5\text{--}4.5$) with *Spitzer*/IRS spectra and 2MASS photometry (colorful solid lines). The grey dashed lines represent the SED model after applying the Lyu & Rieke [53] AGN attenuation curve to the normal AGN template (as defined in Figures 3 and 4).

To reconcile the SED differences of unobscured and obscured AGNs, efforts have been made to generate an AGN attenuation curve. Such determinations have centered on the optical and ultraviolet (e.g., see a brief summary in Li [54]), not the near- to mid-IR that is critical to understand Type 2 objects, e.g., [55]. In the IR, the SEDs of obscured AGNs are frequently represented by obscuring a Type 1 AGN template with a foreground screen of dust with some standard extinction curve (typically similar to the extinction curve for the Small Magellanic Clouds (SMC)). However, the assumption that the extinction curves that work in the UV–optical can be extended into the IR in this simple way is not justified. The AGN accretion disk UV–optical emission and the dust IR emission come from a diverse range of physical scales and the cause of their obscuration can be quite different (for example, the accretion disk can be obscured by the dust along the polar direction, while the AGN near-IR emission is obscured by relatively cold dust in the circumnuclear torus along the equatorial plane). In addition, the properties of dust grains surrounding AGNs are likely modified by the harsh environment, as pointed out by, e.g., Laor & Draine [56] and Maiolino et al. [57], and the resulting attenuation curve is therefore likely to be unique. Moreover, the source of obscuration can also be diverse, ranging from the central dusty torus to the host galaxy ISM (see reviews by [7,58]). Given the typically unresolved observations of AGN structure, it is challenging to constrain the AGN extinction curve in this spectral range. Nevertheless, Lyu & Rieke [53] have used the AGN IR SED variations as a function of silicate absorption at $\sim 10\ \mu\text{m}$ to generate a near- to mid-IR attenuation curve, based on the behavior from unobscured to heavily obscured AGNs. This attenuation curve can be applied to the intrinsic AGN templates (Type 1, Figure 3) to reproduce the SEDs of obscured AGNs reasonably well, as illustrated in the right panel of Figure 5.

2.2.3. Polar/Extended Dust

Spatially resolved imaging reaches resolutions of a few tens of pc for nearby AGNs, using 10 m class telescopes. Emission over 50 pc or more in the mid-IR ($\sim 10 \mu\text{m}$) has been reported for many Seyfert nuclei, including Type 2 AGNs in NGC 1068 [59–61], Cygnus A [62], Circinus [63,64], NGC 1386 [64], IC 5063 and MCG-3-34-64 [65], and the Type 1.5 AGN in NGC 4151 [66], and there is evidence that it is co-spatial with the AGN NLR clouds traced by the optical [O III] lines, e.g., [59,66]. Isbell et al. [37] and Asmus et al. [67] present a comprehensive study of sub-arcsec-resolution images of AGNs in the near-IR (3–5 μm) and mid-IR (10 μm), reporting extended dust structures for many objects. Based on Point-Spread-Function (PSF) subtraction on the arcsec-resolution images of seven AGNs, Fuller et al. [68] found extended dust emission over 0.1–1 kpc at $\sim 37 \mu\text{m}$ for three AGNs (Mrk 3, NGC 4151, and NGC 4388) that might also be attributed to the NLR.

Mid-IR interferometry at 8–13 μm with spatial resolution of just a few pc for nearby AGNs often reveals a polar-elongated dust component, instead of equatorial torus-like structures. Together with the more extended polar emission, these components dominate or contribute significantly to the AGN mid-IR emission in both Type 2 (e.g., NGC 1068, Circinus galaxy, NGC 424; [69] and references therein) and Type 1 objects (NGC 3783 [70], NGC 5506 [69], ESO 323-G77 [71]). Although these studies are critical for understanding the mid-IR emission, they do not undermine the existence of the circumnuclear torus, since its outer zones may just be shadowed by the inner parts so that little energy is deposited in them to be reradiated in the mid-IR.

How this polar dust emission behaves as a function of wavelength is poorly known due to the lack of multi-band spatially resolved observations. Efforts have been made to infer the behavior through SED analysis with some simple assumptions. Figure 6 shows the SED of NGC 3783, which has strong polar emission [70]. Compared with the intrinsic AGN templates discussed in Section 2.2.1, it has a strong peak in the 20–30 μm range. A similar mid-IR spectral bump is seen in many other Seyfert nuclei [72]. Lyu & Rieke [12] attribute this feature to polar dust (e.g., a dusty wind or NLR) and propose a semi-empirical model to match the observations. They apply the obscuration of this extended dust component to the WDD AGN template, showing that this model reproduces the integrated SED and the observed mid-IR polar emission strength of NGC 3783 (Figure 6). The validity of such a simple model has been further corroborated by fitting three more prototypical Type 1 AGNs constrained by interferometry (ESO 323-77, NGC 4507) or by high-resolution imaging (NGC 4151), indicating similar properties for these objects. The fitted SED shape among these sources is very similar [12], with a peak near 25–30 μm . Most of the SED variations seen among Seyfert-1 nuclei and quasars can be reconciled by adding a similar polar dust SED onto the AGN intrinsic templates [41].

The polar emission is likely to be associated with the NLRs, as suggested by, e.g., Netzer & Laor [73]. Although there can be exceptions where a strong NLR is not associated with polar IR emission, e.g., [74], there are virtually no cases with confirmed polar emission that do not also have strong narrow emission lines. Taking advantage of this association, Asmus [75] selected galaxies with strong fluxes in the high-excitation [O IV] 25.89 μm line and found from interferometry that nearly all show polar emission in the 10 μm range. This led to the suggestion that polar emission is ubiquitous and dominant in the mid-IR for *nearly all* AGNs. However, it is not clear if the [O IV] selection biased the result.

Lyu & Rieke [76] explore in a more general way if the AGN NLR strength influences the IR SED behavior. They trace the relative strength of the NLR by the flux ratio between the mid-IR [O IV] line and the WISE W2 ($\sim 4.6 \mu\text{m}$) continuum (the latter traces the hot dust emission luminosity at a wavelength where the contamination by the stellar emission is minimized) and studied its relation to AGN IR colors such as WISE W2–W3 and W2–W4. The W3 band ($\sim 12 \mu\text{m}$) probes the wavelength range where the existence of polar dust is well established and the W4 band ($\sim 22 \mu\text{m}$) is near the suggested peak of the polar dust SED (Figure 6). They found a strong correlation toward larger color differences (more emission in W3 and W4) as the relative [O IV] line strength increases, i.e., a correlation between the

NLR as traced by [OIV] and the strength of the emission by polar dust. Lyu & Rieke [76] derived average IR SED/spectral templates, as seen in Figure 7, which show the dramatic differences in the mid-IR SEDs as a function of [OIV] relative strength. The suggestion from this behavior is that the “normal” SED represents an average, including a range from the HDD case to cases with stronger mid-IR than even indicated by the normal template. This conclusion is consistent with how the normal template is derived—as an average over a sample of AGNs without selection for individual SED behavior.

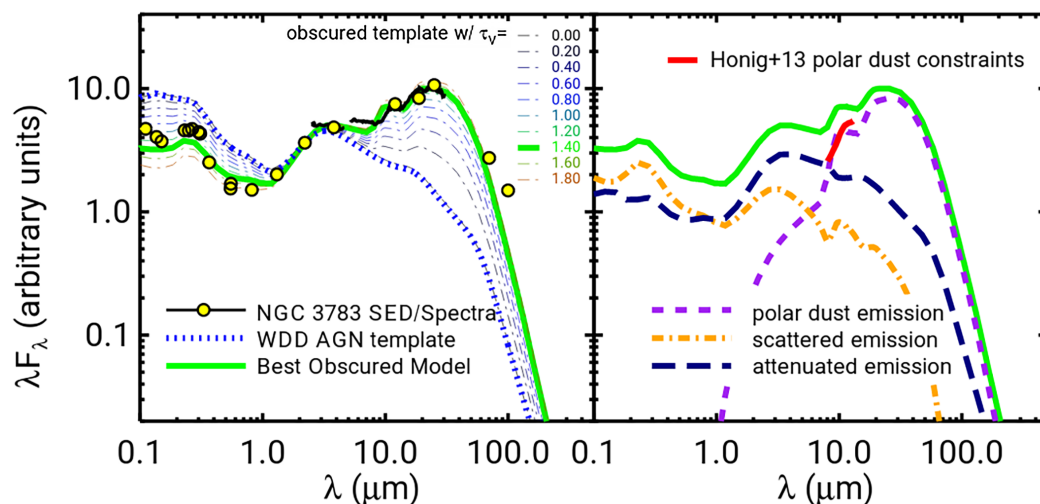


Figure 6. (Left): the observed UV-to-far-IR SED of NGC 3783 as traced by high-resolution data (yellow circles), with the SED model from Lyu & Rieke [12]. (Right): the contributions of various components of the best-fit model as a function of wavelength. The 8–13 μm polar dust emission from Hönig et al. [70] is also shown for comparison. The Lyu & Rieke [12] model obscures the intrinsic AGN template with an extended dust distribution and calculates the resulting SED, which includes three components—(1) attenuated emission of the input SED, (2) scattered, and (3) polar (i.e., reprocessed) emission from this obscuring dust component, through radiation transfer.

In contrast to spatially resolved observations of AGN polar dust that are limited to low- z objects with preferred inclination angles, SED analysis helps us to explore the incidence of polar dust among AGNs in general. For example, from a study of 64 nearby Seyfert-1 galaxies, Lyu & Rieke [12] suggested that approximately one third had SEDs consistent with strong emission by polar dust, one third showed no evidence for such emission, and the remaining third were ambiguous. An indication of the role of polar dust at higher luminosities can be derived from Xu et al. [52], who used the Elvis/normal template to fit quasar SEDs and found in some cases that a warm dust component (with strong emission at rest-frame 3–60 μm) had to be added. However, for 37% of their 99 sources, the luminosity in any fitted warm component was $<5\%$ of the total luminosity attributed to the AGN, in agreement, if slightly higher, with the fraction of the Seyfert galaxies with no evidence for polar dust. The relative strengths of AGN warm dust emission and NLR emission may both decrease towards higher AGN luminosity, e.g., [77,78], indicating a gradual decrease in the significance of the polar dust component for brighter AGNs. This suggestion is aligned with the increasing fraction of WDD AGNs [41] and the lower UV–optical extinction seen in quasars compared to Seyfert nuclei (e.g., see Figure 6 in [12]).

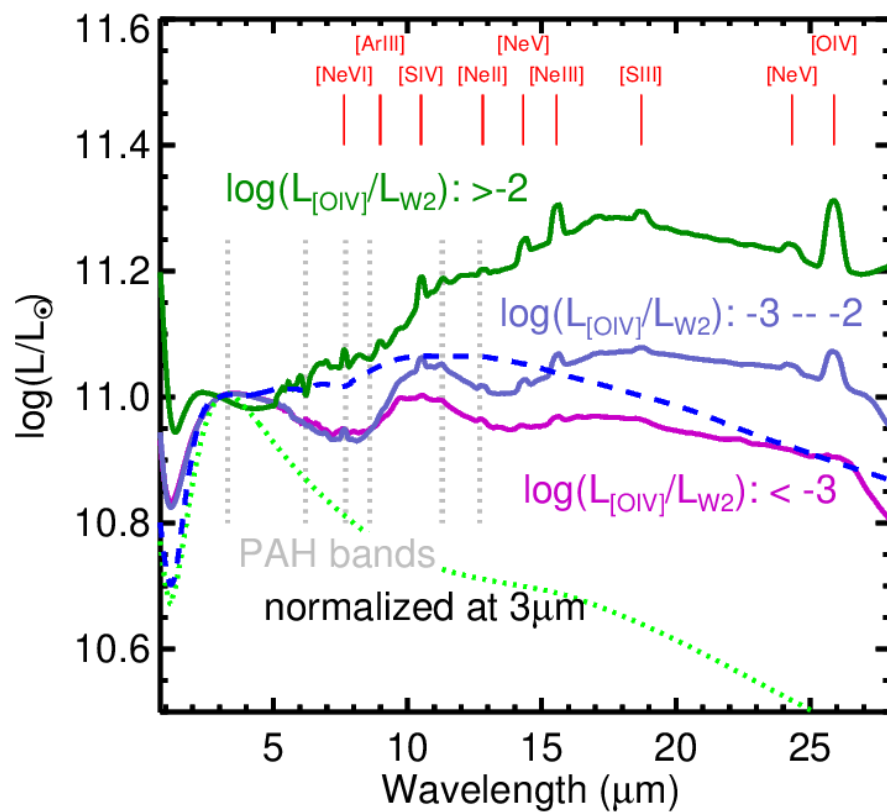


Figure 7. Average AGN mid-IR SEDs for three different bins of the luminosity in [OIV] relative to that in W2. The green dotted line and blue dashed line represent the WDD and normal AGN templates, respectively. All these SED templates are normalized at 3 μm . Based on Lyu & Rieke [76].

2.2.4. Intrinsic Far-IR Emission

The intrinsic far-IR SEDs of AGNs³ provide clues as to their surroundings on a large scale. However, determining the typical far-IR SED has been challenging. Beyond $\sim 30 \mu\text{m}$, there are often substantial contributions from emission by star-formation-heated dust in the host galaxies, e.g., [79–81], which can contaminate the AGN intrinsic SEDs. Removing this contamination is difficult given that the far-IR measurements are made with beam sizes that include both AGN and host. Three approaches have been used to meet this challenge: (1) high spatial resolution on nearby AGNs to isolate the AGN from its host galaxy; (2) use of the aromatic/PAH band(s) to estimate the SFR and its FIR contribution; and (3) use of the FIR SED itself as an estimate of the star formation contribution. Methods of the third type run the risk of being degenerate against the possibility that part of the FIR is powered by the AGN, or that some of the AGN contribution is attributed to star formation. For example, arguments that galaxies with large ratios of 30 μm to shorter-wavelength mid-IR fluxes are dominated by star formation, e.g., Sajina et al. [50], did not anticipate the ability of AGN polar dust to produce similar behavior. Although some minor differences do exist, the majority of studies agree that the intrinsic IR SED of most AGNs turns over in the 20–40 μm range and drops quickly into the far-IR, e.g., [38,72,82–92] (see left panel in Figure 8).⁴

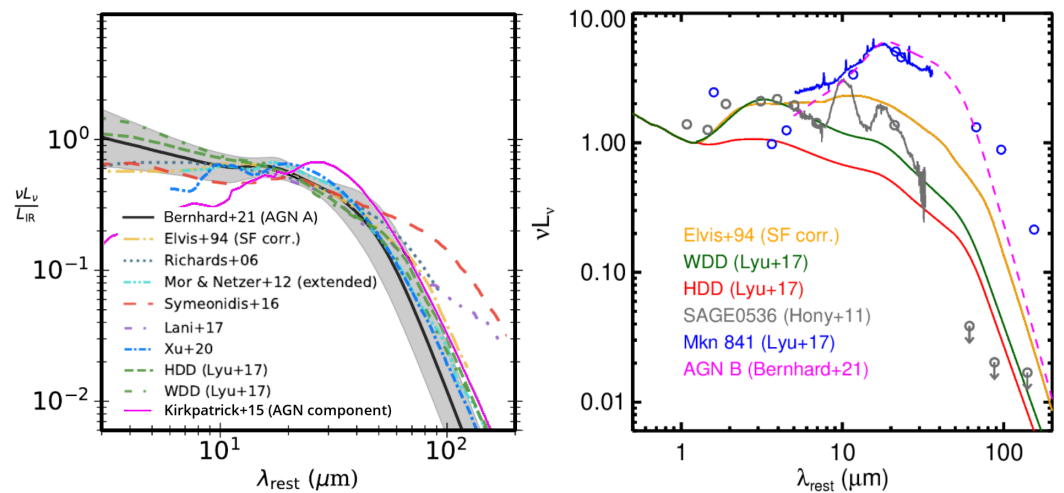


Figure 8. (Left panel): comparison of various AGN templates for relatively luminous AGNs or quasars, corrected for host galaxy contribution in the far-IR. These templates are normalized by their IR luminosity. A general agreement is revealed for most papers (modified based on Figure 14 in Bernhard et al. [82]). (Right panel): similar to the left, we only show the normal Elvis-like AGN template [52]; the WDD and HDD AGN templates [86], normalized in the optical band; the AGN-B template (for less luminous AGNs [82]); plus the observed SEDs of AGE1CJ053634.78-722658.5, an extreme AGN at $z \sim 0.14$ reported by Hony et al. [94], and of Mkn 841, a well-studied PG quasar. The spectrum for it includes a substantial contribution from the host galaxy for wavelengths short of $10 \mu m$; the AGN-only SED is shown by the open circles.

In a few nearby cases, achieving sufficiently high physical resolution to isolate the AGN emission has been possible [68,85,95–97]. With the exception of NGC 1068, however, even in these cases, an unambiguous separation is not possible past $40 \mu m$. Frequently, in the $30\text{--}40 \mu m$ range, there is extended emission that can originate either from the NLR/polar dust (and should be included in the FIR SED) or star formation (which should be excluded) [68]. The best-determined cases show SEDs that fall off beyond $30 \mu m$, similarly to the quasar SEDs in Figure 3, i.e., NGC 1068 [85,96], NGC 4151 [68,97]. Similar behavior probably also holds for Mrk 3 and NGC 3227, but the combined central and polar SED of NGC 4388 rises at least to $40 \mu m$ [68]. García-González et al. [95] used small-aperture photometry on *Herschel* data to identify a few additional candidates to have significant AGN-powered output past $40 \mu m$; we will discuss their results further in Section 2.2.5. In general, even with high spatial resolution, it is desirable to have a spectrum to confirm that circumnuclear star formation is not contributing to the flux, since AGNs may be surrounded by compact star-forming regions (see Section 2.4.4).

Many studies of much larger samples have successfully used the $11.3 \mu m$ aromatic band to estimate the SFR and thus the far-IR emission it is responsible for. Subtracting this component from the integrated SED of an AGN plus host galaxy can provide the AGN component. The basis for this approach is that the PAH band provides an independent measure of the star formation in the host galaxy that allows estimation of its contribution to the far-IR output without resolving the nucleus separately. Typically, a large number of the resulting SF-subtracted SEDs are averaged to obtain the final AGN far-IR template(s), e.g., [84,86,89,91,93].

We now elaborate on some cautions for this approach. The carriers of many aromatic features are destroyed around AGNs, e.g., [98]. However, the $11.3 \mu m$ feature is relatively robust in this environment [99–101]. There are arguments that it can be excited by the AGN [102] (but at levels generally well below the integrated output of an entire star-forming galaxy). Taking it as a valid measure of the SFR, there are still a number of practical issues in its use for this purpose. We illustrate some of them starting with the study of

Palomar–Green (PG) quasars by Petric et al. [103] that concluded that there was inadequate energy from star formation to power the far-IR from these objects.

The first issue is simply obtaining an accurate measure of the PAH feature flux. The profiles of the PAH features are very broad and blended, leading to two approaches to measure their strengths: (1) feature-free continuum points are fitted (typically with linear or spline fits) to determine a local pseudo-continuum above which the core of each individual feature is measured, assuming that these features do not have any overlap, e.g., [104]; or (2) a decomposition is employed that includes the full PAH features, cores plus wings, as exemplified by “PAHFIT” [98]. Typically, the latter approach returns higher values by factors of ~ 2 compared to the measurements based on the simple interpolated continua [98]. Ignoring these systematics can undermine the results⁵ Another concern is the conversion of IR luminosity to SFR; we take the version presented by Calzetti [108], which is a factor of 1.36 lower than that used by Petric et al. [103]. After correcting the systematics behind the $L_{\text{PAH}}-L_{\text{far-IR}}$ and $L_{\text{far-IR}}-\text{SFR}$ relations, we find that the SFR estimated from the total IR luminosity is only a factor of 1.26 greater than that through the 11.3 μm feature for the sample of Petric et al. [103]. This level of discrepancy could arise because the PAH feature lies on the wings of the silicate absorption and hence may be modestly attenuated, e.g., [84,86,109]. That is, the estimates agree within errors and there is no need for a substantial additional energy source, i.e., the AGN, to power the far-IR in the PG sample. This result is confirmed by Xie et al. [110], who use a method based on neon fine structure lines rather than the 11.3 μm feature to determine SFRs for the PG quasar host galaxies and find that the far-IR emission of the PG quasars is generally powered by star formation, not by quasar energy. The above litany of issues based on use of the 11.3 μm feature illustrate the care that must be employed to obtain accurate SFR values in this application.

The third approach to infer the AGN intrinsic far-IR SED assumes that the observed far-IR emission is largely powered by star formation and conducts SED fitting with dust emission templates of purely star-forming galaxies plus very flexible models of AGN IR emission that are suggested to include realistic AGN SEDs. The AGN model that fits the most observations is then selected as the intrinsic AGN template. This approach can be very useful in the mid-IR, where the contrast of AGN to star-forming contributions is high (as shown, for example, in the identification of AGNs as “warm” IRAS sources)⁶ e.g., [111]. However, it runs the risk of being a circular process for determining the AGN far-IR SED. Nonetheless, it returns results similar to those using the other two methods, e.g., [38,82,88,92], which supports the conclusion that the far-IR is indeed powered by star formation, as assumed.

ALMA observations in the submillimeter show a circumnuclear disk with an extent of ~ 40 pc diameter around many AGNs [10]. From spatially resolved spectral indices in the sub-mm region, the emission mechanism appears to be highly inhomogeneous with contributions from thermal emission by dust, synchrotron emission from jets, and free-free emission, e.g., [112,113]. It is unlikely, however, that this component contributes significantly in the mid-IR, since there is no trace of it in high-resolution images such as those discussed at the beginning of Section 2.2.3. It is dramatically absent in very high-resolution images of NGC 1068 [114] and the Circinus Galaxy [115].

2.2.5. Are There AGNs with Substantial Far-IR Output?

The possibility that some AGNs have substantial far-IR emission on top of the typical SEDs described above has been the subject of a number of theoretical models, e.g., [116–118]. Such models are challenged to include realistically the anisotropy of the AGN output and its orientation relative to the host galaxy. In addition, any AGN spectral templates utilized need to be free of contributions from star formation. The latter requirement not only calls for templates that remove star formation effects robustly, as discussed in Section 2.2.4, but can be made more difficult by the increased level of circumnuclear star formation possibly observed in AGNs (see Section 2.4.4 below). From an observational perspective, there is not a convincing case that AGNs power a substantial portion of the far-IR in the

typical case of host galaxies with high levels of star formation (see Section 2.2.4). Here, we discuss whether this situation might nonetheless apply to a subset of AGNs.

Indeed, some cases have been identified where the AGN is claimed to contribute significantly to the flux at 70 μm [88,95]. For [88], the cause is clearly (their Figure 5) that the far-IR contribution from star formation in these galaxies is small, and as a result, the AGN dominates at 70 μm by default; the AGN SED turns over as described in Section 2.2.4. For the second reference, we have used the “normal” template normalized at 24 μm to estimate the AGN contribution at 70 μm . The result is that the AGN may contribute $\sim 50\%$ of the 70 μm flux in the central 1 kpc region for three of nine of their candidates for this behavior (NGC 3783, 4151, and 5347), $\sim 30\%$ for IC 5063, and $\sim 15\%$ for three more (NGC 4253, 7213, and 7479). If the AGN contribution at 70 and 100 μm is removed, the ratio of fluxes at 70 and 100 μm is slightly bluer in some cases than for main sequence star-forming galaxies, based on [119,120], suggesting that IC 5063, NGC 4253, and NGC 7479 might have a detectable far-IR contribution from the AGN.

Candidates for this behavior might also appear in the sample of PG quasars analyzed by Lyu & Rieke [86] in the form of a much weaker 11.3 μm PAH band than predicted by the fits to the far-IR using star-forming templates. Among the cases measured with good signal to noise, there are three candidates for this behavior that also have adequate far-IR data to determine SEDs. Two of these (Mkn 841 and PG 1543+489) have spectral drops in the 30–40 μm range similar to the other AGNs; only PG 1149-110 has a significant far-IR excess above this behavior.

Netzer et al. [121,122] have examined this issue for the most luminous known quasars out to $z \sim 4.8$. They conclude that the far-IR emission in these cases is derived from star formation, with, in general, contributions by the AGN being significantly less important. Symeonidis [123] reanalyzed the sample of Netzer et al. [122] and concluded that their far-IR emission was powered by the AGN; however, her conclusion depends on the validity of her quasar SED template, as discussed in Section 2.2.4.

Thus, although strong far-IR emission may occasionally occur associated with AGN heating, it must be relatively rare, at least among unobscured sources. It remains an interesting possibility in heavily obscured cases, as discussed in Section 2.3.2. An important corollary of the above discussion is that if the far-IR emission of an AGN exceeds the prediction of the normal template significantly, it is very likely to arise from dust heated by recently formed stars (using the far-IR as an SFR indicator should avoid the 5–30 μm region, where the AGN can be dominant). This means that treating the far-IR of an ensemble of galaxies as being predominantly due to star formation is valid, although it may not be for individual cases, e.g., where the far-IR output is weak.

2.3. Behavior of AGN IR Emission II: Complications and Possible Outliers

Thus far, our discussion has focused on “typical” AGNs and has shown how their SED characteristics can be linked by relatively simple arguments, which is very useful in treating a large ensemble of AGNs on the assumption that “one template applies for all”. There is, however, a menagerie of possible exceptions that we discuss below, indicating that this can be a naive premise for some individual objects.

2.3.1. Compton-Thick AGNs

Compton-thick AGNs owe their name to having sufficiently large line-of-sight (LOS) gas columns, $N_H \geq 1.5 \times 10^{24} \text{ cm}^{-2}$, to be optically thick to soft X-rays. Applying a standard relation between gas column and dust extinction [124], this corresponds to $A_V \geq 7$, i.e., the visible light from the nucleus will be totally lost and the IR SED will show very strong obscuration. These sources are nearly invisible from the near IR through the soft X-ray, but have received increased attention with NuSTAR hard X-ray observations. Much of their energy is absorbed and thermalized and emerges in the mid-IR; a promising spectral region to search for them is 4–5 μm , where stellar photospheric emission from the host galaxy is low and PAH bands associated with star formation are absent, e.g., [125]. The greatly

improved IR diagnostics possible with the James Webb Space Telescope (JWST) should revolutionize their study.

Alberts et al. [126] suggest that Compton-thick AGNs can be divided, in roughly equal numbers, into two categories, both of which will have similar SED properties. One is cases where the circumnuclear torus is edge-on as we view it, blocking the view of the central engine and accretion disk with a very high gas and dust column, but potentially identified by NLRs appearing as ionization cones on either side of the central engines. They give as an example NGC 5728, studied in detail by Durré & Mould [127]. The second is truly deeply buried AGNs whose energy is thermalized in the surrounding gas and dust. A possible example is IRAS 08572+3915. This source has extremely deep silicate absorption, $\tau_{9.7} = 4.2 \pm 0.1$ [128], but an otherwise featureless continuum, including the complete absence of emission lines and aromatic features. The depth of the silicate absorption requires by radiative transfer arguments that the luminosity source be buried in the emitting cloud, rather than the emission originating through illumination from the outside the cloud [129–131], possibly indicative of a very deeply embedded AGN (discussion to be continued in the next section).

2.3.2. Embedded AGNs and FIR Emission

As an example of a case where the far-IR may be powered by an embedded AGN, along with the complexities in interpreting the observations, we continue the discussion of IRAS08572+3915; see Figure 9. Models along the line of the obscured standard AGN SEDs discussed in Section 2.2.2 fail to account for the prominent peak in the far-IR, i.e., this object does have substantial far-IR emission above the standard cases, consistent with models such as those of Roebuck et al. [118]. However, Marshall et al. [132], Spoon et al. [133] show that a very similar SED can result from extremely deeply embedded star formation. Nonetheless, Barcos-Muñoz et al. [134] find that IRAS08572+3915 has an extremely compact radio nucleus and substantial IR emission above the predictions of the IR/radio relation. In addition, Iwasawa et al. [135], Yamada et al. [136] show that it is a hard X-ray source. Thus, it appears that an embedded AGN heats the surrounding ISM to some extent, although a star-powered component to the far-IR is still possible. The radio and X-ray measurements are critical to support this interpretation.

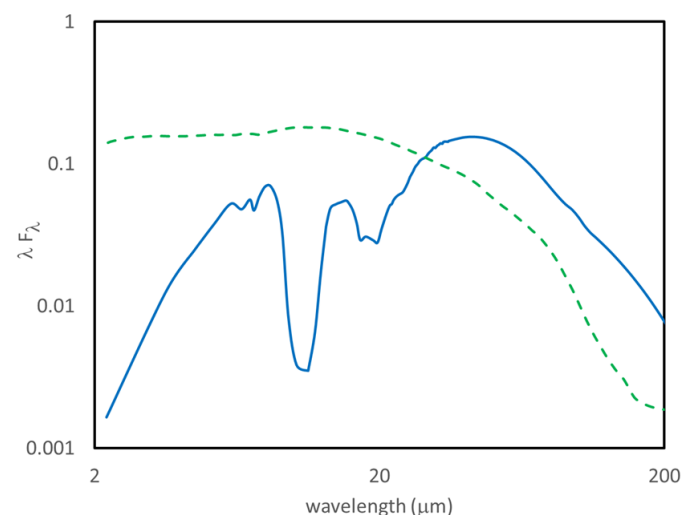


Figure 9. IR SED of IRAS08572+3915 (solid blue line) compared with “normal” template (dashed green line). The SED of IRAS08572 has been normalized to half the IR luminosity of the normal template, on the assumption that half the luminosity of the template escapes at shorter wavelengths, whereas all of the shorter-wavelength energy is captured and reradiated in IRAS08572, doubling its IR output relative to that of the template. This normalization puts the normal SED at its highest plausible level relative to IRAS08572, but nonetheless there is excess far-IR emission above it.

2.3.3. Hot-Dust-Obscured Galaxies

Eisenhardt et al. [137] discovered a class of extreme sources in WISE photometry, faint or undetected in W1 and W2 (3.4 and 4.6 μm) but well detected in W3 and W4 (12 and 22 μm). They were confirmed to be AGNs by Wu et al. [138] and termed hot-dust-obscured galaxies (hot DOGs). Subsequent work has found many more such sources, e.g., [139]. A possibly related but less extreme category of extremely red quasars (ERQs) has been reported by Ross et al. [140]. Both types of source appear to favor relatively high redshifts, $z > 2$. Yan et al. [141] confirm that these sources have huge gas columns ($\geq 10^{25} \text{ cm}^{-2}$), consistent with their having very hard but faint X-ray outputs [142,143]. They are also the sites of large, high-velocity outflows, e.g., [144,145].

Some modeling of the SEDs of hot DOGs suggests that their emission is dominated by their circumnuclear tori, which must have very large covering fractions [51]. Alternatively, it has been suggested that their extreme properties result from their very strong outflows or winds [12,146]. The relatively large ratio of $[\text{O III}]\lambda 5007\text{\AA}$ flux to $\text{H}\beta$ [141,147,148] is consistent with the latter possibility. It would not be surprising if both hypotheses were relevant. Given their exotic nature, it would be foolhardy to be very specific about the circumnuclear environment of these objects until more constraints are available.

2.3.4. Suppressed Near IR?

The Type 1.5 AGN Mkn 841 (=PG 1501+106) is a thoroughly studied example with very weak PAH emission. Not only is this apparent from the *Spitzer* IRS spectrum, but Martínez-Paredes et al. [149] searched for the 11.3 μm PAH feature on sub-arcsec scales and compared with the large-beam measurements with IRS. The feature is not detected in either case and they place an upper limit of $0.2 M_{\odot} \text{ yr}^{-1}$ for the SFR in a 400 pc region around the nucleus as well as for the entire galaxy. The SED must therefore represent purely the AGN; it is shown in the right panel of Figure 8⁷ Compared with normal AGNs, the SED of this object has strong mid-IR excess emission peaked around 20 μm , but the SED still cuts off toward longer wavelengths, as for the more typical cases. The large rise from the near-IR to this peak might be expected for an obscured AGN but is very atypical for a Type 1.5 one.

This behavior might be caused by AGN-heated extended/polar dust, but in this case, Mkn 841 is an extreme example. The ratio of fluxes in $[\text{O III}]\lambda 5007\text{\AA}$ to $\text{H}\beta$ of 0.62 [151] is relatively high but not extreme, suggesting that the necessary extreme form of polar emission is unlikely. Other geometries are possible, such as a very strong outflow approaching the situation that Lyu & Rieke [12] suggest for hot DOGs. In general, the Mkn 841 type of mid-IR SED is likely to be characteristic of any case where a substantial amount of dust near the nucleus is illuminated directly by the AGN accretion disk.

2.3.5. AGNs Deficient in 20–30 μm Output

In the opposite direction, some AGN SEDs have much less far-IR emission than discussed in Sections 2.2.1–2.2.4. For example, both HDD and WDD quasars may have considerably lower far-IR emission compared to other quasars, as seen in the right panel of Figure 8. As noted by Lyu et al. [41], normalized by the accretion disk luminosity, the HDD AGN has only $\sim 40\%$ of the dust emission at 1.25–1000 μm of a “normal” (or average) AGN and this value for WDD AGN is approximately 70%. An even more extreme case has been reported by Hony et al. [94] for the galaxy SAGE1CJ053634.78-722658.5 at $z \sim 0.14$. Although it has similar hot dust emission and mid-IR continuum as a WDD AGN, its far-IR emission drops very quickly (see the right panel of Figure 8).

2.3.6. AGN SEDs in the High-Redshift Universe

To first order, the SEDs of AGNs/quasars at very high redshift ($z \sim 6$) are very similar to those at lower redshift, as shown in Figure 3. For the examples with *Herschel* detections from Leipski et al. [36], the far-IR can very plausibly be associated with star formation in the host galaxies [152], increasing the case for strong similarities. Similar near- to mid-IR SED variations such as WDD and HDD are also seen up to these redshifts [41], further supporting the generally similar behaviors.

It might be expected that very high-redshift quasars would lie in low-metallicity galaxies and possibly be dust-poor, with reduced circumnuclear tori. This was apparently confirmed with the discovery of HDD objects in early *Spitzer* data [39], but the subsequent discovery of similar objects at much lower redshift has undermined this explanation. Another possibility is that heavily dust-embedded phases in quasar formation and evolution will be more common at high redshift, and in this regard, the tendency of hot DOGS and extremely red quasars (ERQs) to be found at high redshift is intriguing, e.g., [51], though efforts have been made to reconcile their SEDs with low- z AGNs [12]. JWST, with its enhanced mid-IR photometry capabilities used to conduct a more complete census of obscured AGNs, may provide new insights into this possibility.

2.3.7. Contamination from Nonthermal Processes

Besides dust emission, nonthermal processes such as synchrotron emission from a jet can also produce near- to far-IR emission, as seen directly in the spatially resolved images of nearby radio-loud systems, e.g., [153,154]. According to the classical unification model of radio-loud AGNs [155], the synchrotron emission can be greatly enhanced by relativistic beaming if a powerful jet points toward the observer, so this component may dominate the IR emission in some AGNs.

Some authors have explored the significance of the nonthermal contribution in the AGN IR emission by spectral/SED decomposition, e.g., [156–158]. Notably, Cleary et al. [156] decomposed the mid-IR spectra of radio systems (radio galaxies and radio-bright quasars) and claimed that the nonthermal contribution can account for 20–90% of the emission in some systems. However, as pointed out by Haas et al. [159], such analyses can be problematic given the fitting degeneracies. A more practical solution, as demonstrated in e.g., [157,158], is to extrapolate the synchrotron emission to the IR, using the constraints in the radio and millimeter bands that show power laws steepening toward higher frequency. The general conclusion is that the nonthermal emission is not dominant in the IR for most radio-loud AGNs, but with some exceptions, e.g., [157]. In fact, the standard SED decomposition techniques (see Section 2.4) have been successfully applied to study the galaxy and AGN dust-related properties in many radio-bright AGNs [158,160] and the necessity for a nonthermal component is not obvious for the majority of cases. The generally insignificant contribution of nonthermal emission is also strongly supported by the very similar average IR SEDs of radio-quiet and radio-loud AGNs, e.g., [32,33,35].

Steep-spectrum radio sources commonly do not show strong IR variability associated with a significant nonthermal source component in the IR [42]. However, the nonthermal IR contribution becomes very prominent for flat-spectrum radio sources, e.g., [42] (see Section 3.4.1). Since the AGN IR SEDs are typically not observed at the same time, the variability of the jet IR emission can cause some non-physical SED features, which complicates the interpretations for some radio-bright objects.

2.4. IR SED Decomposition and Host Galaxy Properties

At some level, the IR SEDs of all AGNs are a combination of contributions by the nuclei and the host galaxies. To constrain their properties, SED fitting or decomposition is typically desired to separate these two components over a wide wavelength range.

2.4.1. Decomposition of Galaxy SEDs with AGN Contributions

Normally, there are three dominant components responsible for the integrated IR emission of an AGN and its host galaxy: (1) stellar photospheric emission; (2) mid- and far-IR emission by dust heated by young stars; and (3) dust heated by the AGN. The first of these components has a nearly uniform spectral behavior throughout the IR and can be included robustly in SED fitting, e.g., [161–163]. The second is also reasonably uniform in spectral behavior from 1 to ~ 15 μm , where many of the challenges in SED fitting are focused, e.g., [164,165], although there is more variety at longer wavelengths. This behavior is discussed further in Section 4.2.1. The mischief lies in the third item.

For the vast majority of AGNs, the existing data provide relatively few truly independent constraints for IR SED fitting (where there are multiple measurements, e.g., points in a spectrum, they are often linked by the underlying physics and the number of independent constraints is much less than the number of spectral points). Thus, some AGN SED model or template is assumed. One popular approach is the adoption of dust radiative transfer models under the assumption that the obscuring structures can be described as smooth tori [166], clumpy tori [167], or some hybrid version [168,169]. Such theoretical models have been used by many authors to fit AGN SEDs, e.g., [170–177]. In general, models of this type have more free parameters than the limited number of independent constraints; thus, parameter degeneracy has to be considered (e.g., with the aid of Bayesian fittings). In addition, these models may lack key features that we now understand to be important but where general constraints are still not understood (e.g., emission by polar dust). Moreover, our ability to test the validity of the theoretical models is limited; in some sense, we have a classic chicken or egg problem because the predictions of the models often can only be verified through SED deconvolution. This problem is exacerbated when models representing some kind of average behavior are applied to individual sources without regard to their eccentricities. In fact, it has been shown that none of the popular models provide good SED fits to a significant subset of AGNs [178].⁸

Another useful SED fitting approach is based on empirically determined families of AGN SED templates. Tools have been developed to fit spectra, e.g., [179,180], photometry, e.g., [181,182], or a combination of both, e.g., [82,88], which have also been used over wide ranges of AGN luminosity and redshift, e.g., [41,52,152,183,184]. Ciesla et al. [185] have used a hybrid approach based on theoretical SED models but down-selected to the minimum needed to fit the range of observational parameters. The success of these approaches relies on the challenging process of the empirical characterization of the SEDs, including the possible variations, of both the pure AGN component and galaxy component. Although well-conceived approaches of this type must by definition represent the average observed behavior reasonably well, they typically do not give insight into the underlying causes of this behavior. In addition, if the number of free parameters is restricted, the empirical templates can be accurate in an average sense but not cover the range of behavior well.

Given the degeneracies and other limitations of SED fitting, it is mainly useful for deriving first-order properties, such as: (1) AGN SED shape and luminosity (already discussed); (2) host galaxy properties directly reflected by the luminosity, such as star formation rates and stellar masses (discussed below); and (3) identifying candidates for obscured AGNs (to be discussed in Section 4.2).

2.4.2. Constraining the Stellar Masses

Very high-resolution imaging can sometimes be used to subtract the AGN emission and measure the flux from the host galaxy, leading to estimates of parameters such as the stellar mass. However, this procedure is often compromised by stray light from the bright AGN component of the image.

Accurate knowledge of the AGN SED allows reasonably good measurements of host galaxy properties through SED decomposition. In the near-IR, the galaxy stellar continuum is almost identical for different galaxy types, with the SED peaking around $1 \mu\text{m}$ and dropping quickly following a Rayleigh–Jeans tail towards the mid-IR. In contrast, the AGN SED presents a dip around $1.3 \mu\text{m}$, with hot dust emission peaking at $2\text{--}4 \mu\text{m}$. With good wavelength coverage of the integrated galaxy emission, we can separate these two components accordingly and retrieve the galaxy light fraction at each band. Ciesla et al. [185] have simulated the ability of such SED fitting to return accurate estimates of the stellar contribution of the host galaxies and converted the results to mass using star formation history models. Their study focuses on galaxies with $10 < \log(M_*) < 11$ and considers AGN templates contributing a range of the total IR luminosity from 0 to 70%. The results are very promising for cases with good photometric coverage, as shown in Figure 10. As expected, the derived host galaxy properties are very well constrained for Type 2 AGNs, since the optical and near-IR emission is dominated by the stars. However, reasonably accurate values are also returned for Type 1 and intermediate cases. For a practical application, Lyu et al. [41] show that a simple SED decomposition with empirical templates can yield results consistent with dedicated AGN galaxy image decompositions for the PG quasar sample. With an assumed stellar mass-to-light ratio, the AGN host galaxy stellar masses can be reasonably determined. This approach is particularly useful for statistical studies where high-resolution image analysis is unavailable, e.g., [52].

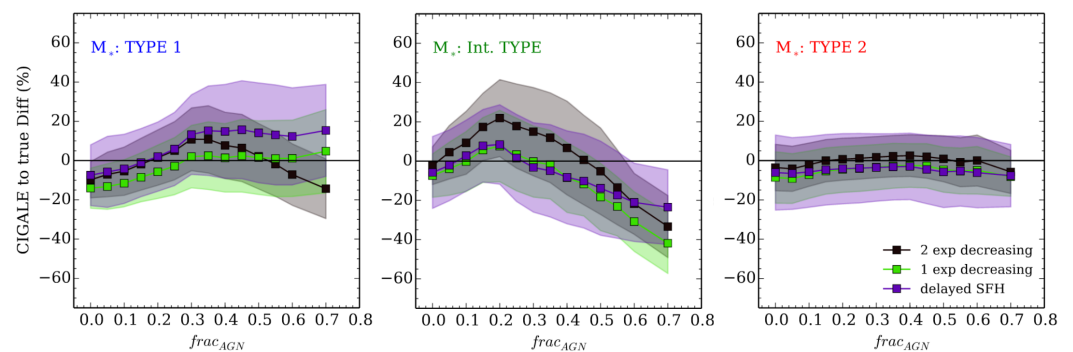


Figure 10. Fractional differences between the stellar mass derived from SED fitting code *CIGALE* and that used as an input to produce the mock photometry from simulations as a function of the AGN-to-total light fraction in the IR luminosity $frac_{AGN}$ (adopted from Figure 6 in [185], reproduced with permission © ESO). The galaxy masses are built up through star formation models as keyed to the lower right. See the original paper for details.

2.4.3. Host IR SED Properties

IR SED decomposition is widely used to measure the far-IR luminosity as an estimate of the host galaxy star formation, under the assumption that the IR SEDs of these galaxies are the same as those of normal star-forming galaxies (SFGs). Empirical SFG templates are useful, since more theoretically based ones contain more free parameters that may result in over-fitting. Based on AGN and galaxy empirical templates that are well calibrated against statistical observations, standard templates provide a satisfactory fit to the far-IR emission of quasar host galaxies at $z \gtrsim 0.5$ (e.g., [82,86,89,91]; see also Section 2.2.4). However, a model with local SFG templates does not work well for quasar host galaxies at $z \gtrsim 5$ (see Figure 11). Nevertheless, after subtracting the AGN contribution, the far-IR SEDs of these very high- z quasars resemble those of very luminous, purely star-forming galaxies at similar redshifts [152,186], still consistent with the argument that their far-IR emission is largely a result of star formation in the hosts.

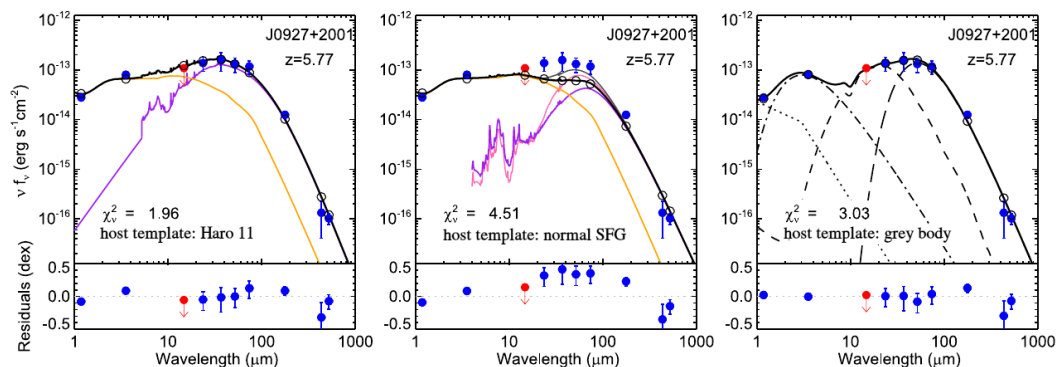


Figure 11. Example SED decomposition of a $z \sim 5.8$ quasar. A template based on the local galaxy Haro 11 has been shown to provide a reasonable fit to luminous SFGs at this redshift [186]. The left panel shows the decomposition of Haro 11 + normal AGN template, the middle panel shows the results of a local SFG + normal AGN template (which works well at low- z), and the right panel is the result from a complicated SED decomposition model used in Leipski et al. [36], where the galaxy IR emission is modeled by a grey body with $T = 47$ K. The open circles are synthetic photometry performed on the fits, while the blue filled circles are the observed photometry. The Haro 11 fit (left panel) is simpler and equally as accurate as the multi-component one, supporting the hypothesis that the far-IR is powered by star formation. This figure is adopted from Lyu et al. [152].

2.4.4. Star Formation

SFRs estimated from far-IR luminosities have been used to conclude that quasar host galaxies tend to lie on or near to the star-forming galaxy main sequence [91,171,184,187–192]. However, Xie et al. [110] recently concluded that AGN hosts predominantly lie above the main sequence. The difference lies almost entirely in the assumed width of the main sequence. For example, Xie et al. [110] take it to be ± 0.2 dex wide, while Xu et al. [91] take it to be $+0.5$ dex and -1 dex, and Zhang et al. [188] take it to be ± 0.6 dex wide. If we apply the Xu et al. [91] limits to the $z = 0.2$ main sequence in Xie et al. [110], we find that only 14/86 of the Xie et al. [110] sample lie above it. That is, there is general agreement that the quasar host galaxies overall have main sequence levels of star formation, although the sample includes a significant minority of starbursts and may lie somewhat high relative to the central main sequence. Even this small bias may be the result of selection effects; the host galaxies of X-ray-selected AGNs align more closely with the main sequence with greater scatter around it [193]. Moreover, there is some evidence that AGN hosts lie below the main sequence at low redshifts [194].

In Section 4.3, we mention a sample of AGNs selected via IRAC variability [195]. It was found that the AGN hosts have similar morphologies to those of a control sample, with perhaps a modest bias toward disturbed or asymmetric galaxies. A similar result was found by Kocevski et al. [196] using a different AGN selection method.⁹ That is, AGN hosts do not seem preferentially to be interacting/merging systems [198]. These results, as with the finding that hosts are largely on the star-forming main sequence, emphasize the *normality* of AGN host galaxies.

The one possible exception to this rather boring normality is that a number of groups have found evidence that the star formation rate in the immediate vicinity of the AGN is often elevated [101,106,199,200].

There have been many studies that find that the black hole accretion rate scales with the SFR, e.g., [187]. However, Xu et al. [91] show that this probably arises because galaxies on the main sequence have a trend of SFR with stellar mass, and the Magorrian relation between the bulge stellar mass and the SMBH mass shows the black hole mass also to grow with stellar mass. Given similar distributions of fractional Eddington luminosities, the range of SMBH masses will be reflected in a similar range of luminosities. In fact, Xu et al. [91] show that the slightly off-1:1 correlation of SFR with stellar mass indicated by the slope of the main sequence is reflected in a similar relation for the SFR vs. AGN luminosity. Dai et al. [187] confirm the slope of SFR vs. AGN luminosity that leads to this conclusion. This is evidence that the apparent linking of the SFR and SMBH luminosity may arise not through a direct causal connection, but because *both* characteristics share a dependence on stellar mass [91,201].

2.4.5. Do AGN Types Correlate with Different SFRs in Host Galaxies?

It has been suggested that the star formation in Type 2 Seyfert host galaxies is systematically higher than in Type 1 hosts. Maiolino et al. [202] found a significant enhancement in the ratio of compact to extended emission for Type 2 hosts by comparing small-aperture ground-based and IRAS measurements at 10.6 and 12 μm , respectively, suggesting that the Type 2 hosts have higher SFRs. Others have found supporting evidence, e.g., [203,204]. However, Diamond-Stanic & Rieke [106] used *Spitzer* imaging data and found no statistically significant differences between AGN types in the distributions of nuclear SFRs, extended SFRs, or total SFRs. Similarly, Masoura et al. [205] studied an X-ray-selected sample and also found no significant difference in SFRs with a nuclear N_H column.¹⁰ Observational biases might explain the apparent differences in results, such as enhanced star formation boosting the brightness of the Type 2 nuclei at 12 μm and producing an IR sample biased toward this behavior; anisotropy in the IR emission affecting the 10 μm outputs of Type 2 AGNs, e.g., [206]; or different measures of the SFRs. Zou et al. [207] provide an interesting summary of the contradictions and uncertainties revolving around the issue of systematic type-related differences in AGN host galaxies.

This issue of differences in SFRs has been examined with a large sample by Zhuang & Ho [200]. They have developed a method using the [OII] and [OIII] optical lines to determine the SFRs. They find a significant tendency toward enhanced SFR in Type 2 hosts. After examining possible selection and other biases, they conclude that their analysis “suggest[s] that, on average, the host galaxies of Type 2 AGNs have intrinsically higher SFRs than those of Type 1 AGNs”. Kalfountzou [208] used the 250 μm luminosity as an indicator of the SFR and also found a tendency for Type 2 hosts to have higher SFR rates than Type 1 hosts, with a formal probability of 0.08 for the two to be drawn from the same distribution for her high signal to noise (at 250 μm) sample (but a probability of 0.23 for a lower signal to noise sample). Zou et al. [207] have conducted another in-depth examination of this possibility, using far-IR luminosity as an indicator of SFRs. They find a tendency at the 1.4 σ level for the hosts of Type 2 AGNs to have higher SFRs than Type 1 ones. They also show that the host galaxies of Type 2 nuclei tend to be slightly more massive. These results are all tantalizing but do not establish an effect at very high confidence. The mass difference, along with the tendency for main sequence levels of star formation, suggests that any difference might simply relate to small systematic differences in host masses.

To test this latter possibility, we will look for a type-dependent difference in specific SFR (sSFR), i.e., SFR relative to the main sequence. To do so, we use the sample of galaxies with high-resolution *L*-band photometry from Isbell et al. [37] (excluding radio-bright objects, LINERs, galaxies classified as star-forming, Arp 220, and the Circinus galaxy). Given the close correlation between galaxy stellar mass and the luminosity in the 3.6 μm region, e.g., [209,210], we use the integrated flux at this wavelength as a proxy for the stellar mass. To derive this flux, we subtract the sub-arcsec-resolution *L* and *M* photometry reported by Isbell et al. [37] from integrated *L*-band fluxes for a

galaxy (from the NASA Extragalactic Database (NED)), giving the L -band flux for the bulk of its stellar population.¹¹ Next, the luminosity at 60–100 μm correlates closely to the total IR luminosity, e.g., [211], and we can use it as a proxy for the star formation rate. Thus, the ratio of the 70 and 3.5 μm luminosities, or for galaxies at low redshift, of the fluxes, becomes a proxy for sSFR. In this sample, the distribution of this ratio is offset by 0.3 dex higher for Type 2 hosts than for Type 1 ones; the Kolmogorov–Smirnov probability that these two distributions are drawn from the same population is 12%. This result and those of Zhuang & Ho [200], Zou et al. [207], Kalfountzou [208] are of modest statistical significance, but their suggestion of an effect is worthy of further investigation.

3. Probing AGN Dusty Structure with IR Reverberation Mapping and Variability

Initially, it was hypothesized that AGN IR emission might be generated nonthermally (Section 2.1). The first observations of IR variability in AGNs addressed this issue, testing for variations sufficiently rapid to require a nonthermal origin. The demonstration of phase lags in the IR relative to variations in the blue and UV, as predicted for a thermal origin, largely settled this issue, e.g., [25,212]. Attention then turned to using the observed time delays between nuclear variations and changes in the IR as circumnuclear dust absorbed and reradiated the nuclear emission—“reverberation mapping”—to learn about the structures of the material surrounding the AGN central engines.

3.1. Challenges

Reverberation mapping is applied extensively in the X-ray, ultraviolet, optical, and for both continuum and emission lines, where it has revealed aspects of the structure of the regions emitting in these spectral ranges (see a recent review by Cackett et al. [9]). From this experience, achieving unambiguous results requires a measurement sequence that samples the variations at the Nyquist rate, with this sampling extending over, as a minimum, three times the longest reverberation lag, although modest gaps in longer datasets should not strongly affect the results, e.g., [213]. With limited datasets, even longer monitoring is needed, e.g., 10 times the longest period [214]. This degree of sampling is relatively easy to achieve in the ultraviolet or optical, where the relevant lag timescales are days or at most weeks. However, the inner edges of the circumnuclear tori in Seyfert galaxies are sufficiently distant from the central engines that minimum lags of months are typical, and the lags for quasar luminosities can be years. This lag length makes it challenging in conventional ground-based campaigns to observe at high cadence over three or more cycles. Shorter sequences, or less intensive sampling, can be useful only if the free parameters in the lag determination are severely limited.

A second issue is general to reverberation mapping. The extent of the emitting region along the line of sight smooths the lag and blurs features that might be indicative of structures, as illustrated in Figure 12. An example might be a circumnuclear torus that lies with its plane along the line of sight. The part of the torus closest to the observer would then show virtually no lag, while that furthest from the observer would show a lag indicative of twice the radius of the torus. Other parts of the torus would fill in between these extremes. That is, the lag itself would be appropriate for the size of the torus but the smoothing could make it impossible to deduce much more about the structure. One way to mitigate this issue is to focus on Type 1 AGNs, where one expects the circumnuclear torus to lie closer to the plane of the sky than in Type 2 objects.

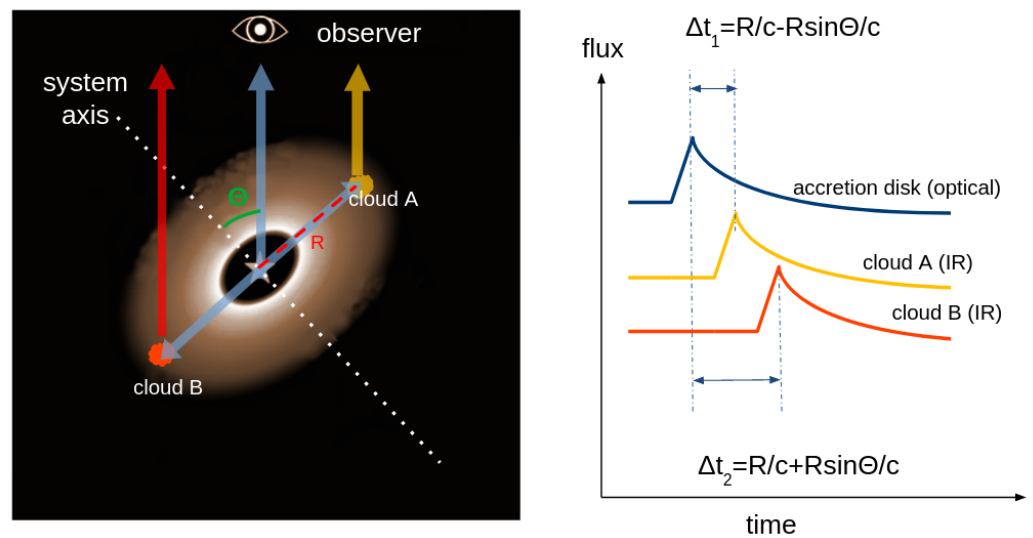


Figure 12. Illustration of the basic concepts of AGN dust reverberation mapping. Assuming two identical dusty clouds (the red and yellow clouds in the figure) at the same distance, R , to the central engine (the blue star), their IR variability signals will be relatively delayed to the optical flare from the accretion disk by $\Delta t_1 = (R/c)(1 - \sin \theta)$ (yellow lines) and $\Delta t_2 = (R/c)(1 + \sin \theta)$ (red lines), where c is the speed of light and θ is the viewing angle of the observer relative to the system axis. In a more realistic case, the IR reverberation signals seen in one band come from a composite of clouds at some ranges of distance and scale height with some possible radiation transfer effects.

3.2. Lag Measurement Campaigns and Basic Results

A pioneering and very extensive ground-based near-IR AGN monitoring effort was conducted at the Crimean Observatory of the Sternberg Astronomical Institute (SAI) from 1994 through 2018 [215–218], with some monitoring extending back to 1985 [215]. These measurements used an aperture photometer with an InSb detector, allowing not only the J (1.25 μm), H (1.65 μm), and K (2.2 μm) bands to be covered, but also the L band (3.6 μm). To mitigate the influence of atmospheric seeing on aperture observations [219], the measurements were made with a large aperture (12''), requiring an accurate correction for the galaxy emission within this aperture. Because of the long extent of the measurement series, including phases where the AGN was very faint, accurate corrections were possible, e.g., [218].

The Multicolor Active Galactic Nuclei Monitoring (MAGNUM) project [220] used a photometer specifically designed for reverberation-type observations. It fed the visible light to a CCD and the IR to an InSb detector array, allowing simultaneous observations from the U -band (0.36 μm) through the L' -band (3.6 μm). It was used to monitor a number of Type 1 Seyfert galaxies and quasars in the V -, R -, I -, J -, H -, and K - bands, e.g., [221,222], from 2001 through 2007, with the results summarized in, e.g., Koshida et al. [223] and Minezaki et al. [224]. In principle, the use of an IR array should improve the robustness against seeing fluctuations and allow subtraction of the galaxy contribution by profile fitting (but, for the latter, Lyu & Rieke [11] find that the galaxy is under-subtracted, possibly due to a strong central concentration of the stellar population).

In addition to these two large-scale reverberation mapping campaigns, there are a large number of focused studies of individual, or a few, sources utilizing near-IR photometry out to the K -band, including, e.g., 3C273 [225], NGC 5548 [226], MCG 6-30-15, [227], NGC 3783 and MR 2251-178 [228], PGC 50427, [229], 3C120 [230], H0507+164 [231], and Z229-15 [232]. K -band measurements are well suited to determining the behavior of the hottest dust (~ 1500 K) at low redshift, but to extend the study to higher redshifts and/or lower-temperature dust, it is essential to monitor at longer wavelengths. Of the ground-based observations discussed so far, only the Sternberg Astronomical Institute campaign goes to the L -band at 3.6 μm . With *Spitzer*/IRAC observations of the Seyfert-1 nucleus in

NGC 6418, Vazquez et al. [233] report dust time lags at 3.6 and 4.5 μm and find that they are roughly consistent with the K-band reverberation results.

The WISE/NEOWISE mission, which completes an all-sky survey roughly every 6 months in two photometric bands at 3.4 and 4.6 μm , offers the opportunity to conduct statistical AGN near-IR reverberation mapping with the combination of optical time domain surveys on the ground, as firstly demonstrated by Lyu et al. [42]. The low cadence of the IR light curves requires that reverberation mapping using these data must be focused on high-luminosity objects, where it is expected that the circumnuclear torus is large and hence the reverberation timescales are long. Some representative studies using these data include, e.g., PG 1302-102 [234]; 87 PG quasars [42]; ~ 690 quasars in SDSS Stripe 82 [177]. The latter two studies use different approaches to smooth and compare the visible and IR light curves, but they obtain very consistent results [177]. Lyu et al. [165] studied the IR reverberation properties of 13 changing-look AGNs and found that they follow a similar relation defined by the PG quasars [42]. Finally, Noda et al. [235] used X-ray and NEOWISE data on the Type 2 AGN NGC 2110, finding a lag consistent with those for Type 1 objects.

All of these studies are consistent with the hottest dust, i.e., the innermost region of the dusty circumnuclear torus, lying near the graphite sublimation distance from the accretion disk. This behavior is illustrated in Figure 13. Despite the different data and analyses used by different authors, the general trend between the near-IR dust time lag (i.e., the hot dust size) and AGN bolometric luminosity extends over five orders of magnitude of AGN luminosity and it follows the expected relation as $\tau \sim 200 \times (L_{\text{bol}}/10^{11}L_{\odot})^{0.5}$ days with a relatively low dispersion ($\lesssim 0.2\text{--}0.3$ dex). This conclusion is now strongly supported by interferometric data at 2 μm for many nearby AGNs that find structures—in some cases even resolved as rings—at the expected radius (Figure 13, right axis) with some additional structures in a few cases, e.g., [236–238].

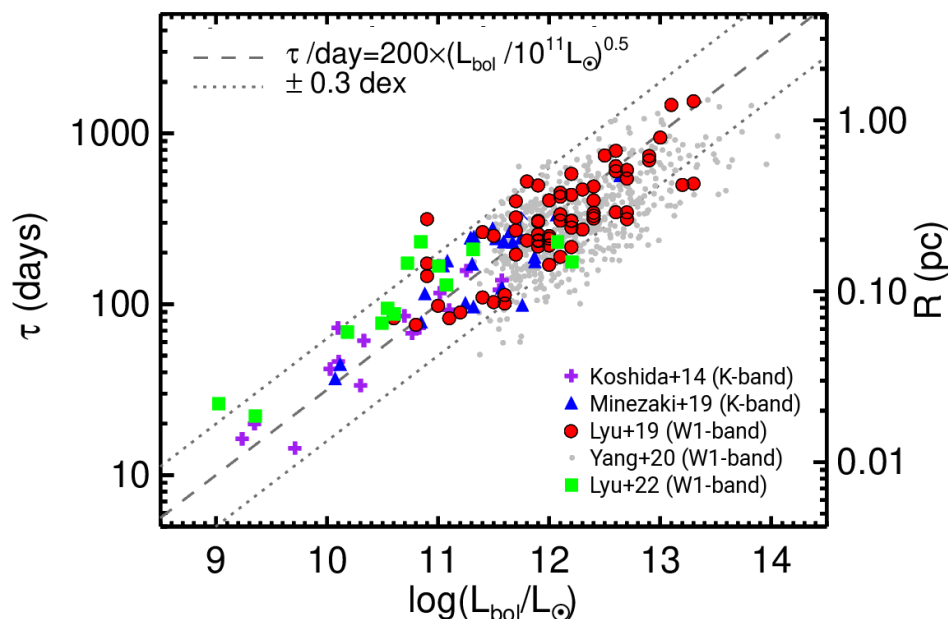


Figure 13. Correlation between the near-IR dust time lags and AGN bolometric luminosity. These measurements include the ground-based K-band ($\sim 2.2 \mu\text{m}$) reverberation mapping results of ~ 50 Seyfert-1 nuclei and quasars from the MAGNUM project [223,224], and the WISE W1-band ($\sim 3.4 \mu\text{m}$), results for 87 PG quasars [42], ~ 590 SDSS Stripe-82 quasars [177], and 13 changing-look AGNs [165]. Despite the various uncertainties and different systemics in these works, there is a strong correlation between the dust time lag and AGN luminosity over five orders of magnitude of AGN luminosity, which can be roughly described as $\tau \sim 200 \times (L_{\text{bol}}/10^{11}L_{\odot})^{0.5}$ days. On the secondary y-axis on the right, we also indicate the corresponding sizes of the dust emission regions assuming $R = \tau c$, where c is the speed of light.

Various other constraints have been reported in some studies. We will evaluate them after discussing the IR reverberation behavior of NGC 4151, which has by far the most extensive set of measurements (next section). It provides a prototype that can be helpful in evaluating the measurements of other AGNs.

3.3. NGC 4151 as a Prototype

NGC 4151 is unique in the extensive IR monitoring available, over 30–40 years; see Figure 14. Nonetheless, the full potential has not been realized because each group monitoring the behavior has tended to analyze its data alone, without merging them into a comprehensive dataset. Lyu & Rieke [11] integrated all the data and analyzed the AGN behavior from 1 through 34 μm .

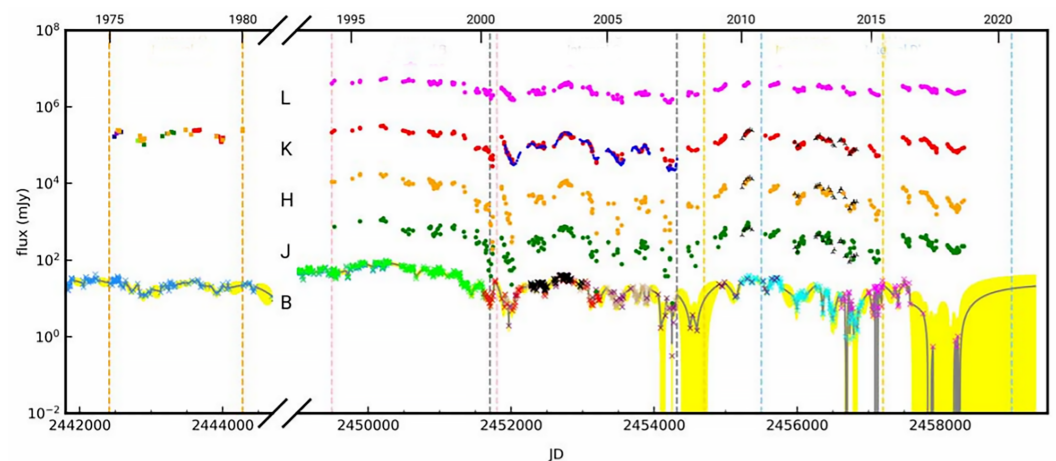


Figure 14. Historical light curves of NGC 4151 compiled from Lyu & Rieke [11]. For details on the data sources and the adjustment of the data to make all the sources consistent, see their paper.

For the near-IR reverberation signals of NGC 4151, Lyu & Rieke [11] found two distinct dust lags of ~ 41 and ~ 90 days, with the latter contribution increasing as a function of wavelength and becoming dominant in the *L*-band (see Figure 15). Lyu et al. [165] recently measured the WISE 3.4 and 4.5 μm dust time lags of NGC 4151 to be ~ 75 –100 days, consistent with the longer lag. Previous near-IR reverberation mapping of this object had led to the conclusion that the lags are wavelength-independent from *J* through the *L* band [239]. The contradiction is not complete; their work found lags generally clustered around the same two values, with 4/7 of those longer than 80 days associated with *L* and only 2/9 cases with lags < 80 days in this band. In addition, previous works report substantial changes in the time delay as summarized for NGC 4151 [240] and it and other galaxies in Oknyansky et al. [239]. In contrast, Lyu & Rieke [11] found relatively little variation over the same time interval and using the same data (see their Table 6). Again, the contradiction is not complete—all studies tend toward lags close to 40 days. To probe the cause of the discrepancies, Lyu & Rieke [11] took the period when the galaxy was being monitored by both the SAI and MAGNUM groups (generally providing Nyquist or sometimes better sampling) and repeated their analysis using only the SAI data, dropping the sampling cadence to sub-Nyquist. There was a significant effect on the lags, changing from 41 and 90 days to 30 and 48 days. As expected, adequate sampling is critical to obtaining reliable results.

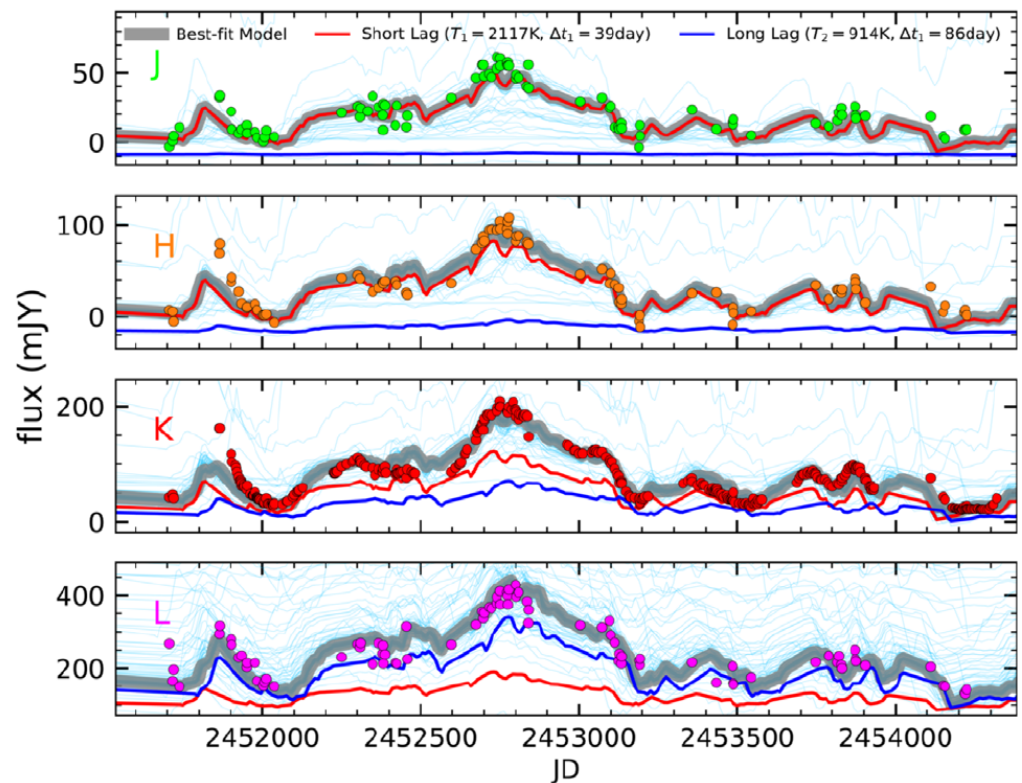


Figure 15. All the near-IR light curves for NGC 4151 in the best-sampled interval, fitted with an integrated two-black-body dust reverberation model. The observed light curves are shown as dots with different colors. The best-fit model is shown as a thick grey line and the contribution from the two different dust components as red and blue lines. The relative contribution of the long lag (blue line) gradually increases towards the longer wavelength and finally dominates the L-band variability. Based on Lyu & Rieke [11].

The detailed monitoring of NGC 4151 shows the potential of multi-wavelength IR reverberation mapping to obtain physical insights about AGNs. Lyu & Rieke [11] identify five source components: (1) one with a lag ~ 41 days and a temperature ~ 1500 K, probably associated with graphite dust at its sublimation temperature and presumably defining the inner rim of the dusty circumnuclear torus at ~ 0.033 pc from the central engine; (2) another with a lag of ~ 90 days and temperature of ~ 900 K, probably dominated by silicate dust at its sublimation temperature (see Section 3.4.4) at a distance of ~ 0.076 pc; (3) a persistent component at ~ 700 K that changes output only over long timescales—over most of the duration of the study, the emission from this component increased by $\sim 4\%$ /year, but prior to that time, it underwent a decrease from the 1980s to the early 1990s [241]; it is probably emission by dust buried in the torus; (4) a component with a lag of ~ 3000 days corresponding to a distance from the central engine of $\sim 2.2\text{--}3.3$ pc and at a temperature of ~ 285 K, possibly associated either with the outer part of a flared circumnuclear torus or as part of a polar wind; and (5) a non-variable component that dominates the output at $\lambda \geq 20 \mu\text{m}$.

These conclusions correlate with structures deduced from the SED, imaging, and interferometry. The placement of the inner edge of the dusty torus at the graphite sublimation radius agrees with the conclusions of Barvainis [24], Mor & Netzer [38] from modeling of the SED, and with interferometric measurements [242]. The long reverberation lag at $10 \mu\text{m}$ agrees with the size of the source at this wavelength measured with interferometry [243]. This behavior clarifies the relation of these structures to each other and their overall placement within AGNs. The large difference in timescales between the lags around $2 \mu\text{m}$ (41 days) and the lag at $10 \mu\text{m}$ (~ 3000 days), plus the amplitudes of the lagging

source components, presents a challenge to purely clumpy models for the torus, which generally predict only modestly longer timescales and lower amplitudes for 10 μm variations compared with those at 2 μm [244,245]. This discrepancy is discussed in Section 5.2. In comparison, the time scales are readily consistent with the wind models proposed by Hönig et al. [70], although the spectrum of the AGN does not show the expected strong silicate emission. Before discussing these issues, we extend the discussion to AGN variability in general.

3.4. Other Observations of AGN IR Variability

3.4.1. General Lack of Classical AGN Variability at 10–24 μm

If the mid-IR flux of classical AGNs arises through dust in a wind or the outer zones of a torus reprocessing the nuclear UV–optical luminosity, there is a prediction that the components dominating the output at the longer mid-IR wavelengths should have very long reverberation-type variability timescales, as demonstrated for NGC 4151. For sources more luminous than this example, the outputs at 10–20 μm should appear to be non-variable over any reasonable measurement period. This prediction has been confirmed by Lyu et al. [42]. They took advantage of the ability of the MIPS instrument on *Spitzer* to provide photometry repeatable to the <1% level in observations at 24 μm . They found that, except for blazars and flat-spectrum radio sources whose mid-IR emission could be nonthermal, the majority of AGNs have typical variation amplitudes at 24 μm of no more than 10% of that in the WISE W1 band, indicating that the dust reverberation signals damp out quickly at longer wavelengths. In particular, steep-spectrum radio quasars also lack strong 24 μm variability, consistent with the unification picture of radio-loud AGNs.

3.4.2. Ubiquitous IR Variability of Steep-Spectrum Radio Sources

Although they are not within the scope of this review, we remark that flat-spectrum radio sources—a category that includes blazars and their relations—are very commonly, perhaps ubiquitously, variable across the mid-IR [42]. This behavior is consistent with the unification of radio-loud AGNs [155] whereby the jet emission of these objects has been greatly amplified due to beaming effects with a very small inclination angle.

3.4.3. Near-IR SED of the Variable Nonthermal AGN Continuum

In the near-IR, accurate determination of the emission by the dust depends on being able to remove the nonthermal continuum associated with the central engine. Theoretically, the slope into the IR is expected to be $\propto \nu^{1/3}$ [246]. However, it has been difficult to confirm this behavior in the optical [247], and thus, there is no obvious reason to expect it in the IR. Kishimoto et al. [248] tested for this behavior on six luminous quasars, finding a spectrum $\propto \nu^{0.41 \pm 0.11}$. García-Bernete et al. [249] used very small-aperture photometry and found slopes consistent with the theoretical value. Lyu & Rieke [11] analyzed the Schülke et al. [250] data that gave simultaneous coverage of the nonthermal regime at the z band (0.9 μm) and the JHK bands extending into the thermal one and found evidence for a steeper-than-theoretical slope for the nonthermal spectrum. Fortunately, the differences among these possibilities are modest in the 1–1.3 μm range, and at longer wavelengths, the radiation by the dust overwhelms the contribution by the nonthermal continuum in any case.

3.4.4. Presence of Two Lags in Near-IR Reverberation Signals of AGNs

The influence of graphite at its sublimation temperature in the torus SED is well established. The second lag observed for NGC 4151 might be associated with a range of possible torus structures, although its relative lag suggests an association with the sublimation of silicate grains. A test of this possibility is whether there is a similar second lag in other AGNs, differing in lag time by approximately the same ratio as the two in NGC 4151. From experience fitting NGC 4151, at K-band, the longer lag component should still account for a significant fraction of the total signal. The photometry of Koshida et al. [223]

and Minezaki et al. [224] is sufficiently accurate to allow a search for such a double lag. It is necessary to discard cases with inadequate data, light curves that clearly depart from the reverberation mapping paradigm (e.g, large departures between the delayed B-band and K-band curves), and cases with poor fits. Nonetheless, the fits are successful for 14/17 of the Koshida et al. [223] sample and 19/30 of the Minezaki et al. [224] one, with overall relations to the trend of $\Delta\tau$ with bolometric luminosity of

$$\Delta\tau_{K, \text{long}} = 10^{2.14 \pm 0.02} \left(L_{\text{bol}} / 10^{11} L_{\odot} \right)^{-0.5} \quad (1)$$

and

$$\Delta\tau_{K, \text{short}} = 10^{1.77 \pm 0.02} \left(L_{\text{bol}} / 10^{11} L_{\odot} \right)^{-0.5} \quad (2)$$

The ratio of short to long lags is then 0.43 ± 0.03 , identical to that for NGC 4151, which is 0.41. The longer lags are also consistent with the reverberation results at ~ 3.4 and $4.6 \mu\text{m}$ [42], where the corresponding dust component becomes more dominant. It appears that the two-lag behavior, with a similar difference in the lags, is a general phenomenon, justifying the connection with silicate grain sublimation. That is, the inner zones of the circumnuclear tori in many/most/all(?) AGNs have structures likely governed by the sublimation of graphite and silicate grains.

4. Completing the AGN Census with IR Selection

Optical spectroscopic surveys such as SDSS enable the identification of large numbers of AGNs through their unique optical–UV emission line characteristics. They have been supplemented by selections using distinctive characteristics of AGN SEDs: UV excess; X-ray emission, particularly with a hard spectrum; or variability in the optical–UV. All these approaches are, unfortunately, biased against heavily obscured samples [7]. The unique IR SED features of AGNs, as compared with quiescent and star-forming galaxies, are central to completing the census of the whole AGN population through discovery of representative obscured objects.

4.1. Selection via Color–Color Diagrams

It was apparent early on that AGNs have characteristic IR behavior. However, a sensitive all-sky survey covering the mid-IR was required to identify AGNs using this behavior, which was provided for the first time by IRAS. These observations were used to detect luminous AGNs through the unique “warmer” SEDs that they exhibited compared with star-forming galaxies, e.g., [111,251]. The 2MASS survey provided another opportunity to identify AGNs through photometric colors; Cutri et al. [252] reported the discovery of a large number of AGNs from 2MASS data. These methods were extended further into the IR with ISO data [253,254].

Spitzer launched a variety of methods to use IR photometry to identify AGNs, most notably IRAC color–color diagrams proposed by Lacy et al. [255] and Stern et al. [256] or, at low redshift, just the 3–5 μm color, e.g., [257]. Veilleux et al. [258] proposed a color–color selection based on longer-wavelength continua measured spectroscopically. An alternative approach used fitting to the IRAC colors to identify objects with power-law SEDs [259,260]. The color and power-law methods were merged by Donley et al. [261], who proposed a more constrained selection criterion in the form of a power-law zone within the previously proposed color–color diagrams. These methods have proven quite powerful; however, because the longest IRAC band is centered at 8 μm , they lose sensitivity to obscured AGNs at modest redshift, and they are best suited to finding cases with typical Type 1 SEDs or modestly obscured Type 1 behavior [261]. To improve on this situation, Alonso-Herrero et al. [259], Donley et al. [260] selected in IRAC colors and then folded in the 24 μm flux and argued that there was an obscured population from the full SED. Using the R–[4.5] color, Hickox et al. [262] found a significant population of obscured AGNs in the Bootes field. At the same time, they show (their Figure 9) how there is a strong bias

against strongly obscured AGNs even at moderate redshift. Surprisingly, even with this limitation, a large number of sources are found that are very faint in the X-ray, indicative of strong absorption there despite the lack of evidence for strong obscuration in the optical and near-IR, e.g., [261,263].

The WISE W3 band at 12 μm improved the wavelength baseline for finding AGNs [264], with less bias against obscured nuclei, e.g., [265–272]. Recent improvements in this approach are described by Hviding et al. [273], based on an extensive study of AGNs identified through optical spectroscopy. This approach allows them to optimize the color selection method so that it can be applied in cases too obscured for reliable optical identification and to push the color selection down to lower AGN luminosities. Combining hard X-ray all-sky surveys with WISE or other mid-IR data has resulted in significant advances in finding heavily obscured AGNs locally, e.g., [265,270,274], although it is believed that the sample is still incomplete, e.g., [265,266]. WISE mid-IR measurements have also proven useful to locate and confirm Compton-thick AGNs in the NuSTAR data, e.g., [275,276]. The addition of the two mid-IR bands from Akari provided more possibilities in this direction [277]. Reliable selection can be achieved by combining mid-IR photometry from IRAC and MIPS on *Spitzer* with far-IR photometry from PACS and SPIRE on *Herschel* [278]. However, all of these methods rely on datasets that are relatively shallow, limiting the results to either very luminous or relatively nearby examples.

The color–color and power-law fitting techniques have the major advantage that they are simple and involve a minimum of free parameters. Given that they are being used with a limited set of mid-IR photometry, these features are important for returning unambiguous results. Nonetheless, there is a range of interpretations of the number and characteristics of AGNs found in this manner, as discussed in the next section. Proposals have been made to use similar approaches with the more extensive photometry that will be provided by the James Webb Space Telescope (JWST), e.g., [279,280].

Limitations of AGN IR Color Selection

IR color selection is a powerful technique to identify AGNs, including many not revealed by other methods. Used conservatively, it can be quite accurate [281]. Of course, the approach also has limitations. The methods are not very sensitive to low-luminosity AGNs that might not stand out from the host galaxy colors. In addition, with deep IRAC data, the color selection becomes degenerate with stellar continua at high redshifts, e.g., [282,283]. The limited ability to characterize SEDs is also a weakness. Finally, most popular color selection methods are unable to identify heavily obscured AGNs, but are focused on power-law SEDs with perhaps only modest reddening. Methods extending into the far-IR avoid some of these issues [278] but are limited by the availability of observations of sufficient depth.

The interest in IR selection largely arises because of the possibility of finding additional highly obscured cases. Thus far, the results are inconclusive. For example, Mendez et al. [283] concluded that only 10% of IR-selected AGNs are heavily obscured, but this result appears to be contradicted by Del Moro et al. [263], who concluded that 30% of the IRAC-selected AGN were too obscured in the X-ray to be detected there. Rather than viewing the difference as a contradiction, it is a reflection of our ignorance and it is better to take both numbers as probable lower limits. Indeed, the predictions of a very large population of heavily obscured AGNs, e.g., [284], suggest that the current methods are only finding a small fraction. The more extensive JWST color information may mitigate these issues, but using simple color–color diagrams will be a relatively primitive approach to the extensive dataset that will become available.

4.2. Selection by SED Analysis

In principle, a more powerful approach is to fit the photometry with SEDs representing the various underlying components—stars, AGNs, star-formation-powered IR excesses, extinction. Models of this type have been demonstrated by Fan et al. [51], Brown et al. [172], Azadi et al. [170], Pouliaxis et al. [174]. However, as discussed in Section 2.4, these models are characterized by large numbers of free parameters, e.g., a large number for the star-forming SEDs and 10 AGN SEDs for Brown et al. [172], or 23 free parameters listed by Pouliaxis et al. [174], and/or they are strongly based on theoretical models that themselves are subject to many free parameters and are not constrained by prior matching to observations of well-studied AGNs [170,172]. These approaches are best suited to characterizing AGNs measured at good signal to noise in multiple independent photometric bands to help remove degeneracies in the fits.

4.2.1. Inputs to SED Fitting

In general, the data to be fitted with model SEDs to search for new AGNs consist even in the most favorable case of a modest set of photometry, with many measurements linked by the underlying physics and not truly independent. Therefore, *the ability of such fitting approaches to provide unambiguous answers depends critically on selecting inputs that provide accurate fits with a minimum of free parameters*. Given the importance of this statement, we describe the approaches in detail.

Yang et al. [285] address an approach to a model for JWST data but do not apply it to existing data. They used X-CIGALE to provide a library of non-AGN galaxy SEDs. They then added an AGN using theoretical predictions from Stalevski et al. [169,286], and subjected the resulting synthetic images to JWST/MIRI simulated photometry. They used X-CIGALE for Markov Chain Monte Carlo SED fitting to the results to extract the AGNs. Their approach is thus similar to the other SED-fitting efforts in the number of free parameters and hence risk of degeneracies, as discussed in Section 2.4.1.

Lyu et al. [182] took a much more aggressive approach to limiting the free parameters in their fits. They used existing capabilities in the Bayesian fitting program Prospector [287] to fit the stellar photospheric continua. In the GOODS-S region where they have applied this approach, the data over the relevant spectral range are extensive and Prospector is thoroughly optimized to provide accurate fits. Importantly for identifying obscured AGNs in the mid-IR, the stellar photospheric SEDs of galaxies are very uniform from 1 to 5 μm , regardless of the galaxy type, e.g., [161–163].

In the mid-IR spectral region of interest for the models, the dominant feature in star-formation-heated dust is PAH bands, and in fact the bands short of $\sim 15 \mu\text{m}$, since the longer-wavelength SED is shifted beyond reach of the *Spitzer* 24 μm band (and of JWST/MIRI) at the redshifts of interest. At the redshifts (~ 2) and luminosities of interest, the variety of star-formation-heated far-IR SEDs is much less than locally [288–290]. Therefore, Lyu et al. [182] have taken the star-heated dust spectrum from the $\log(L(\text{IR})) = 11.25$ template of Rieke et al. [211], which provides a good fit to the overall IR SED of high-luminosity star-forming galaxies at the relevant redshift [186]. For \sim solar metallicities, the 6–12 μm PAH bands are usually similar in relative strength; typical variations in relative band strengths are $\sim 30\%$, $1-\sigma$ [98]. The general behavior of these bands has little dependence upon metallicity (although the 17 μm complex does change significantly), as can be seen comparing the spectra presented in Hunt et al. [291] with templates determined from solar metallicity galaxies [211]. In addition, for the narrow range of luminosities of interest and in the 2–15 μm range, the continua underlying the PAH bands are very similar, independent of luminosity [164,211]. Therefore, it is possible to fit the star-formation-heated dust emission with a single free parameter, i.e., the normalization of the spectrum.

For AGNs, the 2–5 μm region is critical, where the flux from star formation is low but there is significant flux from AGNs (Figure 4). Lyu et al. [182] use the “normal” quasar SED to minimize free parameters and because it is an appropriate average (Section 2.2.3). The application of the AGN-based attenuation curve (Section 2.2.2) allows them to fit a full range of obscuration with a single additional free parameter. In summary, their AGN fits depend on two free parameters—the normalization of the intrinsic SED type and the amount of obscuration.¹²

4.2.2. Results

Figure 16 illustrates a fit from Lyu et al. [182]. The elevated points above the photospheric level in the 3–6 μm range are an unambiguous signature of an embedded AGN; the star-forming PAH-dominated template normalized to account for these points exceeds the 24 μm point substantially. Lyu et al. [182] found that their SED analysis was responsible for >40% of the identified AGN candidates, many of them unique to this method.

The source in Figure 16 is a counterexample to the comment by Hickox & Alexander [7]: “A surprising result from the analysis of the mid-IR continuum of AGN is that obscured AGN have broadly similar mid-IR SEDs to unobscured AGN”. The SED fitting indicates that as many as ~20% of the indicated AGNs are sufficiently strongly obscured to show strong effects in the mid-IR SEDs. If confirmed once we have the more detailed JWST data between 5 and 25 μm , this would indicate that the lack of obscured SEDs is a selection bias and that there are many more such AGNs to discover.

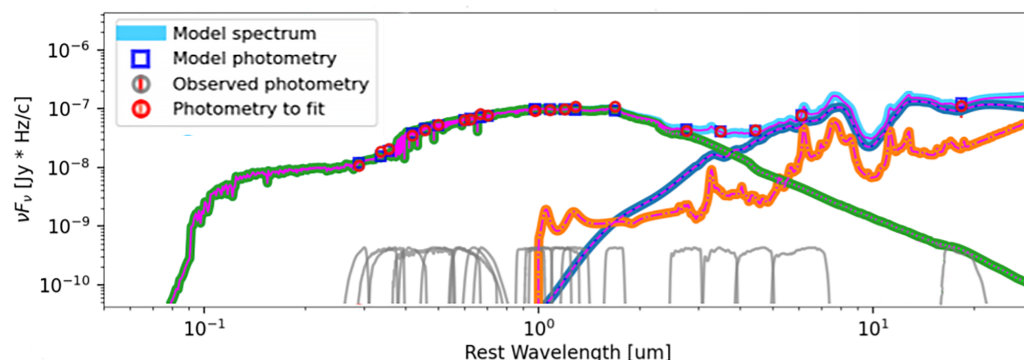


Figure 16. Heavily obscured AGN fit for 3D-HST 10260 ($z = 0.279$), from Lyu et al. [182]. For this galaxy, the stellar photospheric emission is dominant at wavelengths short of 2 μm . The measurements at 4.5–24 μm cannot be fitted by a combination of stellar and PAH band emission, as would be expected for a star-forming galaxy, because a normalization of the star-forming template in the 4.5–8 μm range makes it exceed the 24 μm point by nearly a factor of three. The strongly obscured AGN template (heavy blue line) is a far better fit; it drops sufficiently rapidly toward shorter wavelengths to be insignificant in the optical and ultraviolet.

4.3. Selection by IR Variability

AGN variability across the full spectrum is a huge subject and most of it is outside the scope of this review. However, here, we discuss the use of near- to mid-IR variability to supplement optical–UV variability surveys [1], providing another way to identify AGNs. As summarized in Section 3, although the longer IR wavelengths tend not to vary on useful timescales, the AGN near-IR (1–5 μm) emission contains the signals from the dust reverberation response to the accretion disk variability. Given that the IR wavelengths are relatively less obscured than the optical band, IR variability is expected to be very useful to identify obscured AGNs.

A pioneering investigation of this type is reported by Secret & Satyapal [292], who ironically found that variability is not a good indicator of AGNs in dwarf galaxies, possibly indicating a fundamental difference in their AGNs from those in more massive host galaxies. Early efforts with *Spitzer* include IRAC 3.6 and 4.5 μm and MIPS 24 μm variability selections

in some deep survey fields where multiple exposures have been carried out [293–295]. Kozłowski et al. [293] found a large number of AGNs using repeated IRAC photometry of the nine square degree Boötis survey. A detailed survey of multiple fields surveyed with IRAC is described by Polimera et al. [195]. At typical redshifts for their targets, the rest wavelengths are generally in the 1–3 μm range, i.e., variability could arise either from the nonthermal emission or from the reradiation by dust. They found that $\sim 1\%$ of the galaxies in multiple fields are variable, indicative of AGNs.

With the time domain surveys made accessible by the WISE/NEOWISE mission and ground-based JHK surveys, more authors have explored the use of IR variability to find AGNs, e.g., [264,296]. Recently, Elmer et al. [297] explored high- z AGN selection with long-term near-IR variability using archival UKIDSS data. This is an example of a number of investigations with ground-based JHK data; typically, at the redshifts of the sources, these studies are investigating the nonthermal source variations rather than true rest-IR variability.

Sheng et al. [298] showed that the transitions between broad H recombination lines and weak ones in changing-look AGNs are accompanied by large changes in the fluxes in the WISE bands (see also Assef et al. [264]). This behavior indicates that the IR fluxes are reradiation by the circumnuclear dust of energy absorbed from variations in the accretion disks, as confirmed by their reverberation lags [165]. The alternative explanation for the hydrogen line changes, changing obscuration, is not likely given that even larger changes would be expected in the optical continua and furthermore that the orbital period for a cloud to occult the circumnuclear torus is much too long [298,299]. Stern et al. [300] discuss causes for the changing-look behavior further. WISE data are being used to find these “changing-look” AGNs [300,301].

JWST and the Nancy Grace Roman Space Telescope will enable long-term variability determination through comparison of fluxes with these missions to those measured with *Spitzer* and ground-based near-IR surveys, respectively. There are some lessons learned for these future studies from optical variability monitoring. An alarming result is that methods of increased sophistication have failed to confirm a large majority of apparently variable AGNs, even using virtually the same optical dataset [302]. This may result from the effects of low-level electron production from cosmic ray hits [303]. In any case, it indicates the importance of self-confirmation in variability studies, e.g., by detecting the effect in more than one spectral band and separated in time.

5. Synthesis of Constraints on the AGN Dusty Environment

This section integrates what we have learned from AGN SEDs and reverberation analysis to provide insights into the dusty structures around AGN central engines. In the literature, quite a number of theoretical models relate hypothesized AGN structures and their emission in detailed ways (for impressive examples, see, e.g., the radiative transfer study of NGC 1068 by Viaene et al. [304], the library of clumpy disk models by Nikutta et al. [206], the combined clumpy disk and wind models of CAT3D-WIND [305], and the hydrodynamic models of Williamson et al. [306], among many others). In these works, with the assumed dust structures and grain properties, the resulting IR SEDs and images can be directly computed through radiation transfer calculations. To make an analogy, this approach is similar to imagining the behavior of a dragon and predicting its tracks as a test. However, such models are typically degenerate and have been challenged by recent observations (see discussions below). Our review will take an inverse approach by making largely qualitative (and more limited but perhaps more certain) descriptions of the AGN dusty structures (the dragon) based on the relevant empirical observations (the tracks).

5.1. The Uniformity of the 1–5 μm SEDs and the Radial Structure of the Inner Torus

The general similarity of AGN dust emission SEDs at 1–5 μm (Section 2.2) indicates similar properties of the inner zones of the circumnuclear torus. The same conclusion

holds to $z \gtrsim 6.5$, where the quasar hot dust emission SED shows no evidence for evolution compared with low-redshift AGNs. Reverberation mapping suggests that the hot inner dusty torus has two separated dust components. From a theoretical viewpoint, the inner radius of the dust structures defined by the sublimation of graphite grains is [24]; see also [11]:

$$R_{\text{sub,C}} = 1.3 \left(\frac{L_{\text{UV}}}{10^{46} \text{ erg s}^{-1}} \right)^{0.5} \left(\frac{T_{\text{sub,C}}}{1500 \text{ K}} \right)^{-2.8} \left(\frac{a_{\text{C}}}{0.05 \text{ } \mu\text{m}} \right)^{-0.5} \text{ pc}, \quad (3)$$

Similarly, for the silicate grains, we have

$$R_{\text{sub,S}} = 2.7 \left(\frac{L_{\text{UV}}}{10^{46} \text{ erg s}^{-1}} \right)^{0.5} \left(\frac{T_{\text{sub,S}}}{1000 \text{ K}} \right)^{-2.8} \left(\frac{a_{\text{C}}}{0.05 \text{ } \mu\text{m}} \right)^{-0.5} \text{ pc}. \quad (4)$$

If the innermost boundary is set by the sublimation of graphite dust, then we expect a second component at just over twice the radius due to sublimation of silicate grains. This prediction is consistent with the observed difference in reverberation lags of just over a factor of two (Sections 3.3 and 3.4.4).

Since the metallicities of material surrounding AGNs are high out to the highest redshifts probed [307], the relative abundance of graphite and silicates will be similar in AGN environments. The result is that the inner zones of the circumnuclear tori will be governed by the stability of the grains and will have very similar structures. That is, the similar near-IR properties among different AGNs indicate the similar temperatures, positions (adjusted for central engine luminosity), and compositions of the emitting grains in the AGN sublimation zones. However, our probing is limited because most reverberation mapping campaigns extend only to 2.2 μm ; learning more about the inner dusty torus would benefit from extending the reverberation mapping toward 5 μm .

5.2. Pure Clumpy Torus Models vs. Observations

The torus is expected to be clumpy, based on very general considerations, of which the most compelling is the variability in absorption in the X-ray [308,309], modeled in terms of clumpy models by Buchner et al. [310]. Clumps are also needed to account for the low dust temperatures seen close to the nuclei of AGNs, e.g., [311]. This possibility was anticipated in the prescient work of Krolik & Begelman [312]. A closeup version, without the intense energy input from an active AGN, is provided by the clumpy, tidally sheared circumnuclear disk in the Milky Way's Galactic Center [313].

Purely clumpy models, i.e., little or nothing between the clumps, have been successful in fitting most features of the AGN torus SED, e.g., [85,314–316]. However, as summarized by Netzer [4], “torus models contain enough free parameters to fit almost any observed SED”. Nonetheless, they have three observational shortfalls. First, they do a poor job of fitting the 1–4 μm SED [317,318]. Mor et al. [318] introduced a hot black body component associated with sublimating graphite dust to improve their fits, illustrated by the modeling of Swain et al. [319]. García-González et al. [320] show how adjustments in the standard clumpy model can produce improved fits. Almeyda et al. [245] found that the predicted torus sizes at 2.2 μm from traditional clumpy models are typically a factor of ~ 2 larger than the constrains from K-band reverberation mapping, consistent with the existence of a graphite-dominated torus innermost region. These results suggest that this issue can be addressed by augmenting the models, as discussed in Nikutta et al. [206].

A second, and more fundamental, issue is the lack of variability at wavelengths near 10 μm and longer (Sections 3.3 and 3.4.1). Variability at 10 μm is an intrinsic characteristic of most pure clumpy torus models. For an optically thick clump, the direct heating from the AGN is deposited within the first few optical depths, raising a thin layer on the central engine side of the clump to a high temperature. The remainder of the clump is warmed by diffuse radiation, e.g., from this hot layer, and can have a modest temperature gradient. Thus, the surface of the clump not heated directly emits at a much lower temperature

and can contribute substantially to the output of the torus in the mid-IR. This behavior is modeled in detail by Almeyda [244] and the predicted variations at 10 μm have amplitudes that are a significant fraction of the amplitudes in the near-IR, with modest smoothing in time. This prediction is strongly contradicted by the behavior of NGC 4151 [11] and implicitly by the general lack of variations at observed 24 μm (rest $\lambda \sim 16\text{--}24 \mu\text{m}$) for a large number of luminous traditional AGNs [86]. Hönig & Kishimoto [321] present another study of the IR variability of clumpy torus models, based on a less detailed analytic model than the model of Almeyda [244]. They predict variability at 8 μm to be an order of magnitude less than at 2.2 μm even in the favorable case of a narrow torus (i.e., density falling rapidly with radius). The behavior of NGC 4151 is also inconsistent with this prediction [11].

The third issue is that clumpy models—indeed, torus models in general—do not predict the correlation between the strength of the narrow line emission and the mid-IR excess (Section 2.2.3). This correlation implies that a substantial fraction of the mid-IR emission originates in the NLR, not in the torus. At the same time, the persistence of significant mid-IR emission (perhaps as WDD or HDD templates) even for AGNs with virtually no narrow line emission suggests that there may be a significant component due to the disk itself, with an augmentation by polar dust in cases with strong narrow line emission. The relative roles of the torus and the wind in the mid-IR emission are a central issue for future research. We need to develop means to separate these contributions in large, representative samples of AGNs. High-resolution imaging with giant telescopes can play a central role in this goal [322].

5.3. The Structure of the Torus: Clumpy, Smooth, or Both?

Krolik & Begelman [312] identified the critical issue for maintaining static clumps: resisting tidal shearing and stripping in the vicinity of the black hole. If a clump is to be long-lived, it needs to be stabilized against these effects either by gravity or magnetic fields. To put some numbers on this requirement, we treat the case of gravity, following the discussion in Elitzur [323]. To avoid severe shearing, the Jeans timescale for gravitational collapse should be less than the Keplerian period of the orbit. This leads to a density requirement on the cloud:

$$\frac{n}{10^7 \text{cm}^{-3}} > \frac{M_{\text{SMBH}}}{1 \times 10^7 M_{\odot} r_{\text{pc}}^3} \quad (5)$$

where n is the density of hydrogen atoms and r_{pc} is the radius of the orbit of the cloud around the black hole. Taking values appropriate for NGC 4151 just outside the silicate sublimation radius, say $r_{\text{pc}} = 0.1$ and $M_{\text{SMBH}} = 10^7 M_{\odot}$, the lower limit on the clump density is 10^{10}cm^{-3} .

Thus, stable clumps must be extremely dense and compact. Athena sprang from the skull of Zeus fully formed, but the analogy is not valid for interstellar clouds and clumps. Instead, on very basic grounds, the clumps must be extreme products of turbulence in the torus gas, with weaker clumps and a continuous gas background distributed between. Hybrid clumpy/smooth models have been developed by Siebenmorgen et al. [168], Stalevski et al. [169], which correspond more closely to this picture than either purely clumpy or purely smooth models. However, detailed modeling of the 10 and 20 μm spectrum of NGC 1068 [324] combined with the high-resolution imaging at 10 μm [114] reveal complexities that none of these models can account for, requiring us to consider them to be useful approximations that remain somewhat abstract. Indeed, it appears that none of the popular models are totally successful, even within the limited constraints, in accounting for the torus properties comprehensively [178].

The torus has been the subject of intense theoretical modeling, e.g., [4]. The various hydrodynamical simulations predict a violent environment featuring both inflow and outflow. The simulations of Wada [325], for example, show a circumnuclear torus dominated by turbulence and transitory density enhancements (i.e., “clumps”) embedded in a smoother gas distribution, with a density contrast of a factor of a few. They predict turbulence and winds continuously lifting significant amounts of material off the torus, which would naturally explain the long-term trends seen for NGC 4151, such as the growing (and variable) hot dust emission, as well as the maintenance of the polar dust. Other models, e.g., [305,326–329], make qualitatively similar predictions. The models also provide a unification of hybrid clumpy/smooth torus models and the driving of winds. However, much of the modeling to date has concentrated on the compact, pc-sized circumnuclear torus. ALMA finds both dust and gas in a disk on much larger scales and the future should see more models linking this outer structure with the pc-sized one and simulating the flows that feed the accretion disk.

5.4. Torus, Polar Dust, and Dusty Narrow-Line Regions

As summarized in Section 2.2.3, the extended polar dust, typically associated with the NLR, can dominate the mid-IR output of an AGN, as shown for NGC 1068 in Figure 17. On ~ 10 – 100 pc scales (left panel), its mid-IR dust emission is very extended and elongated, similar to the NLR [59]. Over ~ 0.1 – 1 pc scales, the high-resolution image [114] shows a roughly conical wind rising from the vicinity of the nucleus and sublimation zones, although, even at the resolution of MATISSE¹³ the exact geometry and any contributions by disk emission are not discernible. As another example, the MATISSE image of the Circinus galaxy [115] shows the mid-IR to be dominated by polar emission (see also [330]), with only some blobs of emission along the direction expected for a circumnuclear disk. The lack of emission from the disk in this case could, of course, result because it is shadowed by its inner structure and not sufficiently heated to emit at $10\ \mu\text{m}$, not that the disk is absent. In comparison, ring-like dust structure is clearly revealed in NGC 1068 at shorter wavelengths ($2.2\ \mu\text{m}$) [237], indicating that the relative brightness of the polar dust component is a function of wavelength. That is, for most AGNs the torus-like dust structures dominate the near-IR emission, as is supported by dust reverberation analysis and interferometry observations in the near-IR (Section 3.2), while the polar dust emission is significant at longer wavelengths (Section 2.2.3).

Alonso-Herrero et al. [74] study the relation between the torus and polar dust in additional AGNs. They compare high-resolution (typical beam diameters of ~ 40 pc) images at $\sim 10\ \mu\text{m}$ with ALMA images at $870\ \mu\text{m}$ at around three times higher resolution. ALMA traces the extended circumnuclear disk that lies parallel to and delineates the orientation of the classical torus (see Figure 1). In addition, for six of the twelve galaxies studied, there is an extended mid-IR structure on a 50 – 150 pc scale i.e., similar to that of the extended NLR, that emerges perpendicular to the plane of the torus. The presence of this latter emission correlates with indicators of conditions that can drive outflows [328], i.e., moderate Eddington ratios and moderate-to-high gas column densities.

The cases with bright NLRs but without extended mid-IR emission in Alonso-Herrero et al. [74] have lower Eddington ratios and/or have lower gas columns that allow the clearing of material through blowout. In Section 2.2.3, we also found that about one third of AGNs, particularly those with weak NLR emission, also have much fainter—or absent—polar emission. Understanding what underlies the range from those with mid-IR dominated by polar dust to those where this dust plays a much less prominent role is a major challenge to the detailed radiative modeling of the AGN IR emission.

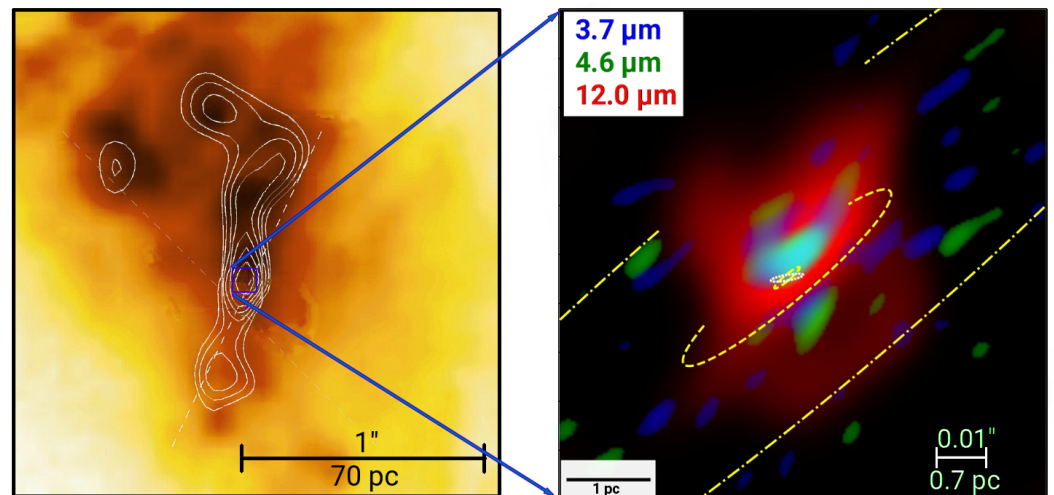


Figure 17. Optical [O III] images overlaid with contours of the extended mid-IR dust emission (at $\lambda = 12.5 \mu\text{m}$) of the archetypal Type 2 AGN in NGC 1068 (left panel) and the near- to mid-IR reconstructed images from MATISSE interferometry observations of the same nucleus at bands *L* (3–4 μm), *M* (4.5–5 μm), and *N* (8–13 μm) (right panel). Modified from the original figures published in Bock et al. [59] (their Figure 4) and Gámez Rosas et al. [114] (their Figure 1e). (Left) reproduced from Bock et al. (2000) with permission; (Right) reprinted from Gámez Rosas et al. (2022).

5.5. Torus Evolution and Its Relation to the Central Engine and Host Galaxy

Dust reverberation analysis and spatially resolved observations show that the AGN torus plus disk covers physical scales bridging from the black hole accretion zone ($\lesssim 0.01 \text{ pc}$) out to the host galaxy ISM ($\gtrsim 100 \text{ pc}$). Structures on this latter scale are indeed seen in the sub-mm [10], although their exact nature is likely to be complex, with a variety of emission sources playing a role, e.g., [112,113]. To feed the accretion disk and grow the SMBH, the dusty clouds within the torus have to migrate inward, become turbulent, and be tidally disrupted. This process can naturally produce the AGN broad-line emission [331].

The mass accretion rate of the SMBH can be estimated by

$$\dot{M}_{\text{BH}} = 0.06 \left(\frac{0.1}{\epsilon} \right) \left(\frac{L_{\text{bol}}}{10^{11} L_{\odot}} \right) M_{\odot} \text{yr}^{-1} \quad (6)$$

where ϵ is the efficiency of the conversion of mass to energy and L_{bol} is the resulting black hole luminosity. An average extended disk plus torus mass of $\sim 6 \times 10^5 M_{\odot}$ has been determined from ALMA measurements [10]. A typical AGN duty cycle is $\sim 2 \times 10^6$ years [332]. Therefore, for an average luminosity for local AGNs of $\sim 10^{11} L_{\odot}$, around 20% of the total disk plus torus mass eventually needs to be accreted by the black hole, a plausible value. The issues linking the torus as discussed here and the larger gas structures feeding it and thus the black hole are reviewed in detail by Hönig [333] and beautifully revealed by García-Burillo et al. [10].

AGNs are proposed to be borne in ultraluminous IR galaxies and emerge as the star formation dies out, e.g., [334,335]. The discovery of Compton-thick sources in the nuclei of many luminous IR galaxies [336] confirms the basic hypothesis. Predictions of how AGNs and their host galaxies co-evolve have suggested that feedback from AGNs, typically associated with (dusty) winds along the AGN polar direction, is the key to regulating the galaxy–BH relation, e.g., [337–339].

However, it is slightly embarrassing that by-and-large the hosts of non-obscured AGNs appear to be normal main sequence star-forming galaxies. They have at most only a slight tendency to be disturbed or have asymmetric morphology compared with non-AGN galaxies, and their star formation appears neither to be quenched nor substantially enhanced. Efforts to deduce a time sequence for AGN evolution have been generally

unsuccessful, e.g., [91,189]. How the AGN dusty and obscuring structures evolve is also an open question. Important clues may lie in an as-yet-undiscovered population of heavily obscured AGNs. We should find many of these AGNs with JWST, if they exist, and can look forward to answers to some of these questions.

Author Contributions: The authors have contributed equally to writing this article. All authors have read and agreed to the published version of the manuscript.

Funding: This work was supported by NASA grants NNX13AD82G and 1255094.

Data Availability Statement: Not applicable.

Acknowledgments: We received extensive and very helpful comments on an early draft from Almudena Alonso-Herrero, Kevin Hainline, Luis Ho, and Robert Nikutta. We also thank Minghao Yue, Feige Wang, and Jinyi Yang for their feedback on the readability of a later draft. We benefitted from discussions with Anna Sajina, Alexandra Pope, and Mark Lacy, and we particularly thank Sajina for her leadership on this Special Issue. This research has made use of the NASA's Astrophysics Data System Bibliographic Services and VizieR catalog access tool, CDS, Strasbourg, France. This publication has also made use of data products from the Wide-Field IR Survey Explorer, which is a joint project of the University of California, Los Angeles, and the Jet Propulsion Laboratory/California Institute of Technology, funded by the National Aeronautics and Space Administration.

Conflicts of Interest: The authors declare no conflict of interest.

Abbreviations

The following abbreviations are used in this manuscript:

AGN	Active Galactic Nucleus
ALMA	Atacama Large Millimeter Array
BH	Black Hole
BLR	Broad-Line Region
DOG	Dust Obscured Galaxy
CCD	Charge-Coupled Device
EW	Equivalent Width
FWHM	Full Width at Half Maximum
HDD	Hot Dust Deficient
HST	Hubble Space Telescope
IR	Infrared
IRAC	Infrared Array Camera (on Spitzer)
IRAS	Infrared Astronomical Satellite
IRS	Infrared Spectrograph (on Spitzer)
ISM	Interstellar Medium
ISO	Infrared Space Observatory
JWST	James Webb Space Telescope
LINER	Low-Ionization Nuclear Emission-line Region
MAGNUM	Multicolor Active Galactic Nuclei Monitoring
MATISSE	Multi AperTure mid-Infrared SpectroScopic Experiment (on the VLT)
MIPS	Multiband Imaging Photometer for Spitzer
NEOWISE	Near-Earth Object Wide-field IR Survey Explorer
NLR	Narrow-Line Region
PAH	Polycyclic Aromatic Hydrocarbon
PACS	Photoconductor Array Camera and Spectrometer (on Herschel)
PG	Palomar-Green
PSF	Point Spread Function
SAI	Sternberg Astronomical Institute

SDSS	Sloan Digital Sky Survey
SED	Spectral Energy Distribution
SFG	Star-Forming Galaxy
SFR	Star Formation Rate
SMBH	Supermassive Black Hole
SPIRE	Spectral and Photometric Imaging Receiver (on Herschel)
SWIRE	Spitzer Wide-Area Infrared Extragalactic (Survey)
UKIDSS	UKIRT Infrared Deep Sky Survey
UV	Ultraviolet
VLTI	Very Large Telescope Interferometer
WDD	Warm Dust Deficient
WISE	Wide-Field Infrared Survey Explorer

Notes

- 1 The term “quasar” has come into general use beyond the original designation of a radio source and encompasses “QSO”—quasi-stellar object.
- 2 The classical unified model attributes the obscuration to the circumnuclear torus, but in reality, there are many possibilities, such as dust in the host galaxy, dusty clouds not in the torus but along the line of sight, or, in extreme cases, a dusty cocoon.
- 3 By “intrinsic”, we refer to the product of direct energy input from the AGN, not necessarily to the integrated SED of the entire galaxy.
- 4 Despite this near-consensus, one notable exception is Symeonidis et al. [93], who predicted much weaker host galaxy far-IR output from the 11.3 μm PAH feature and thus stronger intrinsic far-IR emission from AGNs. Since its publication, this conclusion has been questioned by a number of independent groups based on studies of the same or a similar sample, e.g., [84,86,92].
- 5 To estimate the far-IR SFR from PAH strength, Petric et al. [103] put PAH strength measurements from Shi et al. [105], which used the first method, into a formula from Diamond-Stanic & Rieke [106], which is derived based on PAHFIT values. We can estimate the difference by comparing the equivalent widths (EWs) for the same objects of the 11.3 μm feature from Shi et al. [105] with those from Shi et al. [107], since the latter used a procedure similar to PAHFIT. The average ratio of the two EW measurements of the 11.3 μm PAH is 1.74. (also note that Petric et al. [103] incorrectly cite Diamond-Stanic & Rieke [100] rather than Diamond-Stanic & Rieke [106]).
- 6 These objects are defined with spectral indices between 25 and 60 μm of $-1.25 < \alpha < -0.5$; see de Grijp et al. [111] for details.
- 7 Because the host galaxy has significant photospheric stellar emission (i.e., from a relatively old stellar population), we have used the sub-arcsec measurements at L and M from Isbell et al. [37]. The H -band point is from Peletier et al. [150]; we have subtracted the galaxy as a $n = 4$ Sérsic profile (sometimes known as a de Vaucouleurs profile); the fit for the inner 3'' radius is excellent.
- 8 We may find that they have further difficulties with obscured AGNs when we have a more complete sample.
- 9 Kocevski et al. [197] suggest that abnormalities are more frequent for hosts of Compton-thick AGNs
- 10 However, the majority of their SFR estimates were based on WISE photometry, extending only to 22 μm , which is worrisome because of the potential for AGN contamination.
- 11 We test whether the L -band flux captures the integrated output by comparing with the disk flux in the integrated K_S band from 2MASS, where we subtract the nuclear emission at K_S according to the sub-arcsec L brightness and the normal template for Type 1 and 40% of this value for Type 2 (the selection of values between 0 and 100% had only a $\sim \pm 5\%$ effect on the average and median values). We correct to the expected K_S to L flux ratio if there is a deficiency.
- 12 With the additional constraints with the multiband JWST MIRI measurements, more flexibility can be added to the fits—for example, to include a HDD template and a term for polar dust.
- 13 MATISSE stands for Multi AperTure mid-Infrared SpectroScopic Experiment on the Very Large Telescope Interferometer (VLTI), an instrument that can resolve structures down to 3.5 milli-arcsecond. See more at <https://www.eso.org/sci/facilities/paranal/instruments/matisse.html>, (accessed on 25 May 2022)

References

1. Ulrich, M.-H.; Maraschi, L.; Urry, C.M. Variability of Active Galactic Nuclei. *ARAA* **1995**, *35*, 445–502. [[CrossRef](#)]
2. Alexander, D.M.; Hickox, R.C. What drives the growth of black holes? *NewAR* **2012**, *56*, 93–121. [[CrossRef](#)]
3. Heckman, T.M.; Best, P.N. The Coevolution of Galaxies and Supermassive Black Holes: Insights from Surveys of the Contemporary Universe. *Annu. Rev. Astron. Astrophys.* **2014**, *52*, 589–660. [[CrossRef](#)]
4. Netzer, H. Revisiting the Unified Model of Active Galactic Nuclei. *ARAA* **2015**, *53*, 365–408. [[CrossRef](#)]
5. Padovani, P.; Alexander, D.M.; Assef, R.J.; De Marco, B.; Giommi, P.; Hickox, R.C.; Richards, G.T.; Smolčić, V.; Hatziminaoglou, E.; Mainieri, V.; et al. Active galactic nuclei: What’s in a name? *Astron. Astrophys. Rev.* **2017**, *25*, 2–57. [[CrossRef](#)]

6. Ramos Almeida, C.; Ricci, C. Nuclear obscuration in active galactic nuclei. *NatAs* **2017**, *1*, 679–689.
7. Hickox, R.C.; Alexander, D.M. Obscured Active Galactic Nuclei. *ARAA* **2018**, *56*, 625–671. [[CrossRef](#)]
8. Lacy, M.; Sajina, A. Active galactic nuclei as seen by the Spitzer Space Telescope. *NatAs* **2020**, *4*, 352–363. [[CrossRef](#)]
9. Cackett, E.M.; Bentz, Misty, C.; Kara, E. Reverberation mapping of active galactic nuclei: From X-ray corona to dusty torus. *iScience* **2021**, *24*, 102557. [[CrossRef](#)]
10. García-Burillo, S.; Alonso-Herrero, A.; Ramos Almeida, C.; González-Martín, O.; Combes, F.; Usero, A.; Hönig, S.; Querejeta, M.; Hicks, E.K.S.; Hunt, L.K.; et al. The Galaxy Activity, Torus, and Outflow Survey (GATOS). I. ALMA images of dusty molecular tori in Seyfert galaxies. *Astron. Astrophys.* **2021**, *652*, A98–A137. [[CrossRef](#)]
11. Lyu, J.; Rieke, G.H. The Dusty Heart of NGC 4151 Revealed by $\lambda \sim 1\text{--}40 \mu\text{m}$ Reverberation Mapping and Variability: A Challenge to Current Clumpy Torus Models. *Astrophys. J.* **2021**, *912*, 126–155. [[CrossRef](#)]
12. Lyu, J.; Rieke, G.H. Polar Dust, Nuclear Obscuration, and IR SED Diversity in Type-1 AGNs. *Astrophys. J.* **2018**, *866*, 92–119. [[CrossRef](#)]
13. Baskin, A.; Laor, A. Dust inflated accretion disc as the origin of the broad line region in active galactic nuclei. *Malays. Branch R. Asiat. Soc.* **2018**, *474*, 1970–1994. [[CrossRef](#)]
14. Dors, O.L.; Contini, M.; Riffel, R.A.; Pérez-Montero, E.; Krabbe, A.C.; Cardaci, M.V.; Hägele, G.F. Chemical abundances of Seyfert 2 AGNs–IV. Composite models calculated by photoionization + shocks. *Mon. Not. R. Astron. Soc.* **2021**, *501*, 1370–1383. [[CrossRef](#)]
15. Tazaki, R.; Ichikawa, K. Dust Destruction by Drift-induced Sputtering in Active Galactic Nuclei. *Astrophys. J.* **2020**, *892*, 149–162. [[CrossRef](#)]
16. Low, J.; Kleinmann, D.E. Proceedings of the Conference on Seyfert Galaxies and Related Objects: 17. Infrared Observations of Seyfert Galaxies, Quasistellar Sources, and Planetary Nebulae. *Astrophys. J.* **1968**, *73*, 868. [[CrossRef](#)]
17. Rees, M.J.; Silk, J.I.; Werner, M.W.; Wickramasinghe, N.C. Infrared Radiation from Dust in Seyfert Galaxies. *Nature* **1969**, *223*, 788–791. [[CrossRef](#)]
18. Burbidge, G.R.; Stein, W.A. Cosmic Sources of Infrared Radiation. *Astrophys. J.* **1970**, *160*, 573–593. [[CrossRef](#)]
19. Neugebauer, G.; Oke, J.B.; Becklin, E.E.; Matthews, K. Absolute spectral energy distribution of quasi-stellar objects from 0.3 to 10 microns. *Astrophys. J.* **1979**, *230*, 79–94. [[CrossRef](#)]
20. Stein, W.A.; Weedman, D.W. The origin of ultraviolet and infrared continuum radiation from Seyfert galaxies. *Astrophys. J.* **1976**, *205*, 44–51. [[CrossRef](#)]
21. Penston, M.V.; Penston, M.J.; Neugebauer, G.X.; Tritton, K. P.; Becklin, E.E.; Visvanathan, N. Observations of NGC 4151 during 1970 in the optical and infra-red. *Mon. Not. R. Astron. Soc.* **1971**, *153*, 29–40. [[CrossRef](#)]
22. Rieke, G.H. The infrared emission of Seyfert galaxies. *Astrophys. J.* **1978**, *226*, 550–558. [[CrossRef](#)]
23. Rieke, G.H.; Lebofsky, M.J. Spectral components of NGC 4151. *Astrophys. J.* **1981**, *250*, 87–97. [[CrossRef](#)]
24. Barvainis, R. Hot Dust and the Near-Infrared Bump in the Continuum Spectra of Quasars and Active Galactic Nuclei. *Astrophys. J.* **1987**, *320*, 537–544. [[CrossRef](#)]
25. Clavel, J.; Wamsteker, W.; Glass, I.S. Hot Dust on the Outskirts of the Broad-Line Region in Fairall 9. *Astrophys. J.* **1989**, *337*, 236–250. [[CrossRef](#)]
26. Hunt, L.K.; Zhekov, S.; Salvati, M.; Mannucci, F.; Stanga, R.M. Limits on the short-timescale near-infrared variability of Seyfert 1 nuclei. *Astron. Astrophys.* **1994**, *292*, 67–75.
27. Soifer, B.T.; Sanders, D.B.; Madore, B.F.; Neugebauer, G.; Danielson, G.E.; Elias, J.H.; Lonsdale, C.J.; Rice, W.L. The IRAS Bright Galaxy Sample. II. The Sample and Luminosity Function, *Astrophys. J.* **1987**, *320*, 238. [[CrossRef](#)]
28. Kotilainen, J.K.; Ward, M.J.; Boisson, C.; Depoy, D.L.; Smith, M.G. Near-infrared imaging of hard X-ray selected active galaxies–II. The non-stellar continuum. *Mon. Not. R. Astron. Soc.* **1992**, *256*, 149–165. [[CrossRef](#)]
29. Neugebauer, G.; Green, R.F.; Matthews, K.; Schmidt, M.; Soifer, B.T.; Bennett, J. Continuum Energy Distributions of Quasars in the Palomar–Green Survey. *Astrophys. J. Suppl.* **1987**, *63*, 615–644. [[CrossRef](#)]
30. Neugebauer, G.; Matthews, K. Variability of Quasars at 10 Microns. *Astrophys. J.* **1999**, *118*, 35–45. [[CrossRef](#)]
31. Ward, M.; Elvis, M.; Fabbiano, G.; Carleton, N.P.; Willner, S.P.; Lawrence, A. The Continuum of Type 1 Seyfert Galaxies. I. A Single Form Modified by the Effects of Dust. *Astrophys. J.* **1987**, *315*, 74–91. [[CrossRef](#)]
32. Elvis, M.; Wilkes, B.J.; McDowell, J.C.; Green, R.F.; Bechtold, J.; Willner, S.P.; Oey, M.S.; Polowski, E.; Cutri, R. Atlas of Quasar Energy Distributions. *Astrophys. J. Suppl.* **1994**, *95*, 1–67. [[CrossRef](#)]
33. Richards, G.T.; Lacy, M.; Storrie-Lombardi, L.J.; Hall, P.B.; Gallagher, S.C.; Hines, D.C.; Fan, X.; Papovich, C.; Vanden Berk, D.E.; Trammell, G.B.; et al. Spectral Energy Distributions and Multiwavelength Selection of Type 1 Quasars. *Astrophys. J. Suppl.* **2006**, *166*, 470–497. [[CrossRef](#)]
34. Scott, A.E.; Stewart, G.C. Do the spectral energy distributions of type 1 active galactic nuclei show diversity? *Mon. Not. R. Astron. Soc.* **2014**, *438*, 2253–2266. [[CrossRef](#)]
35. Shang, Z.; Brotherton, M.S.; Wills, B.J.; Wills, D.; Cales, S.L.; Dale, D.A.; Green, R.F.; Runnoe, J.C.; Nemmen, R.S.; Gallagher, S.C.; et al. The Next Generation Atlas of Quasar Spectral Energy Distributions from Radio to X-Rays. *Astrophys. J. Suppl.*, **2011**, *196*, 2–24. [[CrossRef](#)]
36. Leipski, C.; Meisenheimer, K.; Walter, F.; Klaas, U.; Dannerbauer, H.; De Rosa, G.; Fan, X.; Haas, M.; Krause, O.; Rix, H.-W. Spectral Energy Distributions of QSOs at $z > 5$: Common Active Galactic Nucleus-heated Dust and Occasionally Strong Star-formation. *Astrophys. J.* **2014**, *785*, 154–175. [[CrossRef](#)]

37. Isbell, J.W.; Leonard Burtscher, L.; Asmus, D.; Pott, J.-U.; Couzy, P.; Stalevski, M.; Gámez Rosas, V.; Meisenheimer, K. Subarcsecond Mid-infrared View of Local Active Galactic Nuclei. IV. The L- and M-band Imaging Atlas. *Astrophys. J.* **2021**, *910*, 104–123. [[CrossRef](#)]
38. Mor, R.; Netzer, H. Hot graphite dust and the infrared spectral energy distribution of active galactic nuclei. *Mon. Not. R. Astron. Soc.* **2012**, *420*, 526–541. [[CrossRef](#)]
39. Jiang, L.; Fan, X.; Brandt, W.N.; Carilli, C.L.; Egami, E.; Hines, D.C.; Kurk, J.D.; Richards, G.T.; Shen, Y.; Strauss, M.A.; et al. Dust-free quasars in the early Universe. *Nature* **2010**, *464*, 380–383. [[CrossRef](#)]
40. Hao, H.; Elvis, M.; Civano, F.; Lawrence, A. Hot-dust-poor Quasars in Mid-infrared and Optically Selected Samples. *Astrophys. J.* **2011**, *733*, 108–117. [[CrossRef](#)]
41. Lyu, J.; Rieke, G.H.; Shi, Y. Dust-deficient Palomar-Green Quasars and the Diversity of AGN Intrinsic IR Emission. *Astrophys. J.* **2017**, *835*, 257–283. [[CrossRef](#)]
42. Lyu, J.; Rieke, G.H.; Smith, P.S. Mid-IR Variability and Dust Reverberation Mapping of Low-*z* Quasars. I. Data, Methods, and Basic Results. *Astrophys. J.* **2019**, *886*, 33–65. [[CrossRef](#)]
43. Elitzur, M. On the Unification of Active Galactic Nuclei. *Astrophys. J.* **2012**, *747*, L33–L35. [[CrossRef](#)]
44. Hickox, R.C.; Myers, A.D.; Greene, J.E.; Hainline, K.N.; Zakamska, N.L.; DiPompeo, M.A. Composite Spectral Energy Distributions and Infrared-Optical Colors of Type 1 and Type 2 Quasars. *Astrophys. J.* **2017**, *849*, 53. [[CrossRef](#)]
45. Prieto, M.A.; Reunanen, J.; Tristram, K.R.W.; Neumayer, N.; Fernandez-Ontiveros, J.A.; Orienti, M.; Meisenheimer, K. The spectral energy distribution of the central parsecs of the nearest AGN. *Mon. Not. R. Astron. Soc.* **2010**, *402*, 724–744. [[CrossRef](#)]
46. Alonso-Herrero, A.; Quillen, A.C.; Simpson, C.; Efstathiou, A.; Ward, M.J. The Nonstellar Infrared Continuum of Seyfert Galaxies. *Astron. J.* **2001**, *121*, 1369–1384. [[CrossRef](#)]
47. Videla, L.; Lira, P.; Andrews, H.; Alonso-Herrero, A.; Alexander, D.M.; Ward, M. Nuclear Infrared Spectral Energy Distribution of Type II Active Galactic Nuclei. *ApJS* **2013**, *204*, 23. [[CrossRef](#)]
48. Polletta, M.; Tajer, M.; Maraschi, L.; Trinchieri, G.; Lonsdale, C.J.; Chiappetti, L.; Andreon, S.; Pierre, M.; Le Fèvre, O.; Zamorani, G.; et al. Spectral Energy Distributions of Hard X-Ray Selected Active Galactic Nuclei in the XMM-Newton Medium Deep Survey. *Astrophys. J.* **2007**, *663*, 81–102. [[CrossRef](#)]
49. Polletta, M.; Wilkes, B.J.; Siana, B.; Lonsdale, C.J.; Kilgard, R.; Smith, H.E.; Kim, D.W.; Owen, F.; Efstathiou, A.; Jarrett, T.; et al. Chandra and Spitzer Unveil Heavily Obscured Quasars in the Chandra/SWIRE Survey. *Astrophys. J.* **2006**, *642*, 673–693. [[CrossRef](#)]
50. Sajina, A.; Yan, L.; Fadda, D.; Dasyra, K.; Huynh, M. Spitzer- and Herschel-based Spectral Energy Distributions of 24 μm Bright $z \sim 0.3$ – 3.0 Starbursts and Obscured Quasars. *Astrophys. J.* **2012**, *757*, 13. [[CrossRef](#)]
51. Fan, L.; Han, Y.; Nikutta, R.; Drouart, G.; Knudsen, K.K. Infrared Spectral Energy Distribution Decomposition of WISE-selected, Hyperluminous Hot Dust-obscured Galaxies. *Astrophys. J.* **2016**, *823*, 107–123. [[CrossRef](#)]
52. Xu, L.; Rieke, G.H.; Egami, E.; Pereira, M.J.; Haines, C.P.; Smith, G.P. A Herschel Study of 24 μm -Selected AGNs and Their Host Galaxies. *Astrophys. J. Suppl.* **2015**, *219*, 18–53. [[CrossRef](#)]
53. Lyu, J.; Rieke, G.H. Infrared Attenuation Curve for AGNs. *in preparation*.
54. Li, A. Dust in Active Galactic Nuclei, The Central Engine of Active Galactic Nuclei. *ASP Conf. Ser.* **2007**, *373*, 561–573.
55. Zafar, T.; Møller, P.; Watson, D.; Fynbo, J.P.U.; Krogager, J.-K.; Zafar, N.; Saturni, F.G.; Geier, S.; Venemans, B.P. Extinction curve template for intrinsically reddened quasars. *Astron. Astrophys.* **2015**, *584*, 100–107. [[CrossRef](#)]
56. Laor, A.; Draine, B.T. Spectroscopic Constraints on the Properties of Dust in Active Galactic Nuclei. *Astrophys. J.* **1993**, *402*, 441. [[CrossRef](#)]
57. Maiolino, R.; Marconi, A.; Salvati, M.; Risaliti, G.; Severgnini, P.; Oliva, E.; La Franca, F.; Vanzi, L. Dust in active nuclei. I. Evidence for “anomalous” properties. *Astron. Astrophys.* **2001**, *365*, 28–36. [[CrossRef](#)]
58. Bianchi, S.; Maiolino, R.; Risaliti, G. AGN Obscuration and the Unified Model. *Adv. Astron.* **2012**, *2012*, 782030. [[CrossRef](#)]
59. Bock, J.J.; Neugebauer, G.; Matthews, K.; Soifer, B.T.; Becklin, E.E.; Ressler, M.; Marsh, K.; Werner, M.W.; Egami, E.; Blandford, R. High Spatial Resolution Imaging of NGC 1068 in the Mid-Infrared. *Astrophys. J.* **2000**, *120*, 2904–2919. [[CrossRef](#)]
60. Braatz, J.A.; Wilson, A.S.; Gezari, D.Y.; Varosi, F.; Beichman, C.A. High-Resolution Mid-Infrared Imaging and Astrometry of the Nucleus of the Seyfert Galaxy NGC 1068. *Astrophys. J. Lett.* **1993**, *409*, 5–8. [[CrossRef](#)]
61. Cameron, M.; Storey, J.W.V.; Rotaciuc, V.; Genzel, R.; Verstraete, L.; Drapatz, S.; Siebenmorgen, R.; Lee, T.J. Subarcsecond Mid-Infrared Imaging of Warm Dust in the Narrow-Line Region of NGC 1068. *Astrophys. J.* **1993**, *419*, 136–150. [[CrossRef](#)]
62. Radomski, J.T.; Piña, R.K.; Packham, C. High-Resolution Mid-Infrared Morphology of Cygnus A. *Astrophys. J.* **2002**, *566*, 675–681. [[CrossRef](#)]
63. Packham, C.; Radomski, J.T.; Roche, P.F.; Aitken, D.K.; Perlman, E.; Alonso-Herrero, A.; Colina, L.; Telesco, C.M. The Extended Mid-Infrared Structure of the Circinus Galaxy. *Astrophys. J. Lett.* **2005**, *618*, 17–20. [[CrossRef](#)]
64. Reunanen, J.; Prieto, M.A.; Siebenmorgen, R. VLT diffraction-limited imaging at 11 and 18 μm of the nearest active galactic nuclei. *Mon. Not. R. Astron. Soc.* **2010**, *402*, 879–894. [[CrossRef](#)]
65. Hönig, S.F.; Kishimoto, M.; Gandhi, P.; Smette, A.; Asmus, D.; Duschl, W.; Polletta, M.; Weigelt, G. The dusty heart of nearby active galaxies. I. High-spatial resolution mid-IR spectro-photometry of Seyfert galaxies. *Astron. Astrophys.* **2010**, *515*, 23–44. [[CrossRef](#)]

66. Radomski, J.T.; Piña, R.K.; Packham, C. Resolved Mid-Infrared Emission in the Narrow-Line Region of NGC 4151. *Astrophys. J.* **2003**, *587*, 117–122. [[CrossRef](#)]
67. Asmus, D.; Hönic, S.F.; Gandhi, P. The Subarcsecond Mid-infrared View of Local Active Galactic Nuclei. III. Polar Dust Emission. *Astrophys. J.* **2016**, *822*, 109–121. [[CrossRef](#)]
68. Fuller, L.; Lopez-Rodriguez, E.; Packham, C.; Ichikawa, K.; Togi, A.; Alonso-Herrero, A.; Ramos-Almeida, C.; Diaz-Santos, T.; Levenson, N.A.; Radomski, J. SOFIA/FORCAST resolves 30–40 μm extended dust emission in nearby active galactic nuclei. *Mon. Not. R. Astron. Soc.* **2019**, *483*, 3404–3419. [[CrossRef](#)]
69. López-Gonzaga, N.; Burtscher, L.; Tristram, K.R.W.; Meisenheimer, K.; Schartmann, M. Mid-infrared interferometry of 23 AGN tori: On the significance of polar-elongated emission. *Astron. Astrophys.* **2016**, *591*, 47–57. [[CrossRef](#)]
70. Hönic, S.F.; Kishimoto, M.; Tristram, K.R.W.; Prieto, M.A.; Gandhi, P.; Asmus, D.; Antonucci, R.; Burtscher, L.; Duschl, W.J.; Weigelt, G. Dust in the Polar Region as a Major Contributor to the Infrared Emission of Active Galactic Nuclei. *Astrophys. J.* **2013**, *771*, 87–100. [[CrossRef](#)]
71. Leftley, J.H.; Tristram, K.R.W.; Hönic, S.F.; Kishimoto, M.; Asmus, D.; Gandhi, P. New Evidence for the Dusty Wind Model: Polar Dust and a Hot Core in the Type-1 Seyfert ESO 323-G77. *Astrophys. J.* **2018**, *862*, 17–31. [[CrossRef](#)]
72. Deo, R.P.; Richards, G.T.; Crenshaw, D.M.; Kraemer, S.B. The Mid-Infrared Continua of Seyfert Galaxies. *Astrophys. J.* **2009**, *705*, 14–31. [[CrossRef](#)]
73. Netzer, H.; Laor, A. Dust in the Narrow-Line Region of Active Galactic Nuclei. *Astrophys. J. Lett.* **1993**, *404*, L51–L54. [[CrossRef](#)]
74. Alonso-Herrero, A.; García-Burillo, S.; Hönic, S.F.; García-Berete, I.; Ramos Almeida, C.; González-Martín, O.; López-Rodríguez, E.; Boorman, P.G.; Bunker, A.J.; Burtscher, L.; et al. The Galaxy Activity, Torus, and Outflow Survey (GATOS). II. Torus and polar dust emission in nearby Seyfert galaxies. *Astron. Astrophys.* **2021**, *652*, 99–124. [[CrossRef](#)]
75. Asmus, D. New evidence for the ubiquity of prominent polar dust emission in AGN on tens of parsec scales. *Mon. Not. R. Astron. Soc.* **2019**, *489*, 2177–2188. [[CrossRef](#)]
76. Lyu, J.; Rieke, G.H. Polar Dust Emission in Quasar IR SEDs and Its Correlation with Narrow Line Regions. *Astrophys. J.* **2022**, *submitted*
77. Maiolino, R.; Shemmer, O.; Imanishi, M.; Netzer, H.; Oliva, E.; Lutz, D.; Sturm, E. Dust covering factor, silicate emission, and star formation in luminous QSOs. *Astron. Astrophys.* **2007**, *468*, 979–992. [[CrossRef](#)]
78. Stern, J.; Laor, A. Type 1 AGN at low z —II. The relative strength of narrow lines and the nature of intermediate type AGN. *Mon. Not. R. Astron. Soc.* **2012**, *426*, 2703–2718. [[CrossRef](#)]
79. Rodríguez Espinosa, J.M.; Rudy, R.; Jones, B. Star Formation in Seyfert Galaxies. *Astrophys. J.* **1987**, *312*, 555–565. [[CrossRef](#)]
80. Rowan-Robinson, M. A new model for the infrared emission of quasars. *Mon. Not. R. Astron. Soc.* **1995**, *272*, 737–748.
81. Wilson, A.S. Star formation and nuclear activity in Seyfert galaxies. *Astron. Astrophys.* **1988**, *206*, 41–46.
82. Bernhard, E.; Tadhunter, C.; Mullaney, J.R.; Grimmer, L.P.; Rosario, D.J.; Alexander, D.M. The post-Herschel view of intrinsic AGN emission: Constructing templates for galaxy and AGN emission at IR wavelengths. *Mon. Not. R. Astron. Soc.* **2021**, *503*, 2598–2621. [[CrossRef](#)]
83. Kirkpatrick, A.; Pope, A.; Sajina, A.; Roebuck, E.; Yan, L.; Armus, L.; Díaz-Santos, T.; Stierwalt, S. The Role of Star Formation and an AGN in Dust Heating of $z = 0.3$ – 2.8 Galaxies. I. Evolution with Redshift and Luminosity. *Astrophys. J.* **2015**, *814*, 9. [[CrossRef](#)]
84. Lani, C.; Netzer, H.; Lutz, D. Intrinsic AGN SED & black hole growth in the Palomar-Green quasars. *Mon. Not. R. Astron. Soc.* **2017**, *471*, 59–79.
85. Lopez-Rodriguez, E.; Fuller, L.; Alonso-Herrero, A.; Efstathiou, A.; Ichikawa, K.; Levenson, N.A.; Packham, C.; Radomski, J.; Ramos Almeida, C.; Benford, D.J.; et al. The Emission and Distribution of Dust of the Torus of NGC 1068. *Astrophys. J.* **2018**, *859*, 99–108. [[CrossRef](#)]
86. Lyu, J.; Rieke, G.H. The Intrinsic Far-infrared Continuum of Type-1 Quasars. *Astrophys. J.* **2017**, *841*, 76–89. [[CrossRef](#)]
87. Miley, G.K.; Neugebauer, G.; Soifer, B.T. IRAS observations of Seyfert galaxies. *Astrophys. J. Lett.* **1985**, *293*, 11–14. [[CrossRef](#)]
88. Mullaney, J.R.; Alexander, D.M.; Goulding, A.D.; Hickox, R.C. Defining the intrinsic AGN infrared spectral energy distribution and measuring its contribution to the infrared output of composite galaxies. *Mon. Not. R. Astron. Soc.* **2011**, *414*, 1082–1110. [[CrossRef](#)]
89. Netzer, H.; Lutz, D.; Schweitzer, M.; Contursi, A.; Sturm, E.; Tacconi, L.J.; Veilleux, S.; Kim, D.-C.; Rupke, D.; Baker, A.J.; et al. Spitzer Quasar and ULIRG Evolution Study (QUEST). II. The Spectral Energy Distributions of Palomar-Green Quasars. *Astrophys. J.* **2007**, *666*, 806–816. [[CrossRef](#)]
90. Rosario, D.J.; Santini, P.; Lutz, D.; Shao, L.; Maiolino, R.; Alexander, D.M.; Altieri, B.; Andreani, P.; Aussel, H.; Bauer, F.E.; et al. The mean star formation rate of X-ray selected active galaxies and its evolution from $z \sim 2.5$: Results from PEP-Herschel. *Astron. Astrophys.* **2012**, *545*, A45–A62. [[CrossRef](#)]
91. Xu, L.; Rieke, G.H.; Egami, E.; Haines, C. P.; Pereira, M.J.; Smith, G.P. The Relation between Luminous AGNs and Star Formation in Their Host Galaxies. *Astrophys. J.* **2015**, *808*, 159–168. [[CrossRef](#)]
92. Xu, J.; Sun, M.; Xue, Y. AGNs Are Not That Cool: Revisiting the Intrinsic AGN Far-infrared Spectral Energy Distribution. *Astrophys. J.* **2020**, *894*, 21–32. [[CrossRef](#)]
93. Symeonidis, M.; Giblin, B.M.; Page, M.J.; Pearson, C.; Bendo, G.; Seymour, N.; Oliver, S.J. AGN are cooler than you think: The intrinsic far-IR emission from QSOs. *Mon. Not. R. Astron. Soc.* **2016**, *459*, 257–276. [[CrossRef](#)]

94. Hony, S.; Kemper, F.; Woods, P.M.; van Loon, J.T.; Gorjian, V.; Madden, S.C.; Zijlstra, A.A.; Gordon, K.D.; Indebetouw, R.; Marengo, M.; et al. The Spitzer discovery of a galaxy with infrared emission solely due to AGN activity. *Astron. Astrophys* **2011**, *531*, 137–143. [[CrossRef](#)]
95. García-González, J.; Alonso-Herrero, A.; Hernán-Caballero, A.; Pereira-Santaella, M.; Ramos-Almeida, C.; Acosta-Pulido, J.A.; Díaz-Santos, T.; Esquej, P.; González-Martín, O.; Ichikawa, K.; et al. The nuclear and integrated far-infrared emission of nearby Seyfert galaxies. *Mon. Not. R. Astron. Soc.* **2016**, *458*, 4512–4529. [[CrossRef](#)]
96. Rieke, G.H.; Low, F.J. The infrared spectrum of NGC 1068. *Astrophys. J. Lett.* **1975**, *199*, L13–L17. [[CrossRef](#)]
97. Rieke, G.H.; Low, F.J. Measurements of galactic nuclei at 34 microns. *Astrophys. J. Lett.* **1975**, *200*, L67–L69. [[CrossRef](#)]
98. Smith, J.D.T.; Draine, B.T.; Dale, D.A.; Moustakas, J.; Kennicutt, R.C.; Helou, G.; Armus, L.; Roussel, H.; Sheth, K.; Bendo, G.J.; et al. The Mid-Infrared Spectrum of Star-forming Galaxies: Global Properties of Polycyclic Aromatic Hydrocarbon Emission. *Astrophys. J.* **2007**, *656*, 770–791. [[CrossRef](#)]
99. Alonso-Herrero, A.; Ramos Almeida, C.; Esquej, P.; Roche, P.F.; Hernán-Caballero, A.; Hönic, S.F.; González-Martín, O.; Aretxaga, I.; Mason, R.E.; Packham, C.; et al. Nuclear 11.3 μm PAH emission in local active galactic nuclei. *Mon. Not. R. Astron. Soc.* **2014**, *443*, 2766–2782. [[CrossRef](#)]
100. Diamond-Stanic, A.; Rieke, G.H. The Effect of Active Galactic Nuclei on the Mid-infrared Aromatic Features. *Astrophys. J.* **2010**, *724*, 140–153. [[CrossRef](#)]
101. Esquej, P.; Alonso-Herrero, A.; González-Martín, O.; Hönic, S.F.; Hernán-Caballero, A.; Roche, P.; Ramos Almeida, C.; Mason, R.E.; Díaz-Santos, T.; Levenson, N.A.; et al. Nuclear Star Formation Activity and Black Hole Accretion in Nearby Seyfert Galaxies. *Astrophys. J.* **2014**, *780*, 86–100. [[CrossRef](#)]
102. Jensen, J.J.; Hönic, S.F.; Rakshit, S.; Alonso-Herrero, A.; Asmus, D.; Gandhi, P.; Kishimoto, M.; Smette, A.; Tristram, K.R.W. PAH features within few hundred parsecs of active galactic nuclei. *Mon. Not. R. Astron. Soc.* **2017**, *470*, 3071–3094. [[CrossRef](#)]
103. Petric, A.O.; Ho, L.C.; Flagey, N.J.M.; Scoville, N.Z. Herschel Survey of the Palomar-Green QSOs at Low Redshift. *Astrophys. J. Suppl.* **2015**, *219*, 22–41. [[CrossRef](#)]
104. Brandl, B.R.; Bernard-Salas, J.; Spoon, H.W.W.; Devost, D.; Sloan, G.C.; Guilles, S.; Wu, Y.; Houck, J.R.; Weedman, D.W.; Armus, L.; et al. The Mid-Infrared Properties of Starburst Galaxies from Spitzer-IRS Spectroscopy. *Astrophys. J.* **2006**, *653*, 1129–1144. [[CrossRef](#)]
105. Shi, Y.; Ogle, P.; Rieke, G.H.; Antonucci, R.; Hines, D.C.; Smith, P.S.; Low, F.J.; Bouwman, J.; Willmer, C. Aromatic Features in AGNs: Star-forming Infrared Luminosity Function of AGN Host Galaxies. *Astrophys. J.* **2007**, *669*, 841–861. [[CrossRef](#)]
106. Diamond-Stanic, A.; Rieke, G.H. The Relationship between Black Hole Growth and Star Formation in Seyfert Galaxies. *Astrophys. J.* **2012**, *746*, 168–181. [[CrossRef](#)]
107. Shi, Y.; Rieke, G.H.; Ogle, P.M.; Su, K.Y.L.; Balog, Z. Infrared Spectra and Photometry Of Complete Samples of Palomar-Green and Two Micron All Sky Survey Quasars. *Astrophys. J. Suppl.* **2014**, *214*, 23–39. [[CrossRef](#)]
108. Calzetti, D. Star Formation Rate Indicators. In *Secular Evolution of Galaxies*; Falcón-Barroso, J., Knapen, J.H., Eds.; Cambridge University Press: Cambridge, UK, 2013; pp. 419–459.
109. Hernán-Caballero, A.; Spoon, H.W.W.; Alonso-Herrero, A.; Hatziminaoglou, E.; Magdis, G.E.; Pérez-González, P.G.; Pereira-Santaella, M.; Arribas, S.; Cortzen, I.; Labiano, Á.; et al. Extinction in the 11.2 μm PAH band and the low $L_{11.2}/L_{IR}$ in ULIRGs. *Mon. Not. R. Astron. Soc.* **2020**, *497*, 4614–4625. [[CrossRef](#)]
110. Xie, Y.; Ho, L.C.; Zhuang, M.-Y.; Shangguan, J. The Infrared Emission and Vigorous Star Formation of Low-redshift Quasars. *Astrophys. J.* **2021**, *910*, 124–134. [[CrossRef](#)]
111. de Grijp, M.H.K.; Miley, G.K.; Lub, J.; de Jong, T. Infrared Seyferts: A new population of active galaxies? *Nature* **1985**, *314*, 240–242. [[CrossRef](#)]
112. Alonso-Herrero, A.; García-Burillo, S.; Pereira-Santaella, M.; Davies, R.I.; Combes, F.; Vestergaard, M.; Raimundo, S.I.; Bunker, A.; Díaz-Santos, T.; Gandhi, P.; et al. Nuclear molecular outflow in the Seyfert galaxy NGC 3227. *Astron. Astrophys.* **2019**, *628*, 65–81. [[CrossRef](#)]
113. García-Burillo, S.; Combes, F.; Ramos Almeida, C.; Usero, A.; Alonso-Herrero, A.; Hunt, L.K.; Rouan, D.; Aalto, S.; Querejeta, M.; Viti, S.; et al. ALMA images the many faces of the NGC 1068 torus and its surroundings. *Astron. Astrophys.* **2019**, *632*, 61–88. [[CrossRef](#)]
114. Gámez Rosas, V.; Jacob, W.; Isbell, J.W.; Jaffe, W.; Petrov, R.G.; Leftley, J.H.; Hofmann, K.-H.; Millour, F.; Burtscher, L.; Meisenheimer, K.; et al. Thermal imaging of dust hiding the black hole in NGC 1068. *Nature* **2022**, *602*, 403–407. [[CrossRef](#)] [[PubMed](#)]
115. Isbell, J.W.; Meisenheimer, K.; Pott, J.-U.; Stalevski, M.; Tristram, K.R.W.; Sanchez-Bermudez, J.; Hofmann, K.-H.; Gámez Rosas, V.; Jaffe, W.; Burtscher, L.; et al. The dusty heart of Circinus: I. Imaging the circumnuclear dust in N-band. *arXiv* **2022**, arXiv:2205.01575
116. Ballantyne, D.R.; Shi, Y.; Rieke, G.H.; Donley, J.L.; Papovich, C.; Rigby, J.R. Does the AGN Unified Model Evolve with Redshift? Using the X-Ray Background to Predict the Mid-Infrared Emission of AGNs. *Astrophys. J.* **2006**, *653*, 1070–1088. [[CrossRef](#)]
117. McKinney, J.; Hayward, C.C.; Rosenthal, L.J.; Martínez-Galarza, J.R.; Pope, A.; Sajina, A.; Smith, H.A. Dust-enshrouded AGNs Can Dominate Host-galaxy-scale Cold Dust Emission. *Astrophys. J.* **2021**, *951*, 55–64. [[CrossRef](#)]
118. Roebuck, E.; Sajina, A.; Hayward, C.C.; Pope, A.; Kirkpatrick, A.; Hernquist, L.; Yan, L. The Role of Star Formation and AGN in Dust Heating of $z=0.3\text{--}2.8$ Galaxies—II. Informing IR AGN Fraction Estimates through Simulations. *Astrophys. J.* **2016**, *833*, 60–73. [[CrossRef](#)]

119. Dale, D.A.; Cook, D.O.; Roussel, H.; Turner, J.A.; Armus, L.; Bolatto, A.D.; Boquien, M.; Brown, M.J.I.; Calzetti, D.; De Looze, I.; et al. Updated 34-band Photometry for the SINGS/KINGFISH Samples of Nearby Galaxies. *Astrophys. J.* **2017**, *837*, 90–109. [[CrossRef](#)]
120. Skibba, R.A.; Engelbracht, C.W.; Dale, D.A.; Hinz, J.; Zibetti, S.; Crocker, A.; Groves, B.; Hunt, L.; Johnson, B.D.; Meidt, S.; et al. The Emission by Dust and Stars of Nearby Galaxies in the Herschel KINGFISH Survey. *Astrophys. J.* **2011**, *739*, 89–106. [[CrossRef](#)]
121. Netzer, H.; Mor, R.; Trakhtenbrot, B.; Shemmer, O.; Lira, P. Star Formation and Black Hole Growth at $z = 4.8$. *Astrophys. J.* **2014**, *791*, 34–48. [[CrossRef](#)]
122. Netzer, H.; Lani, C.; Nordon, R.; Trakhtenbrot, B.; Lira, P.; Shemmer, O. Star Formation Black Hole Growth and Dusty Tori in the Most Luminous AGNs at $z = 2–3.5$. *Astrophys. J.* **2016**, *819*, 123–145. [[CrossRef](#)]
123. Symeonidis, M. What produces the far-infrared/submillimetre emission in the most luminous QSOs?. *Mon. Not. R. Astron. Soc.* **2017**, *465*, 1401–1408. [[CrossRef](#)]
124. Güver, T.; Özel, F. The relation between optical extinction and hydrogen column density in the Galaxy. *Mon. Not. R. Astron. Soc.* **2009**, *400*, 2050–2053. [[CrossRef](#)]
125. Severgnini, P.; Caccianiga, A.; Della Ceca, R. A new technique to efficiently select Compton-thick AGN. *Astron. Astrophys.* **2012**, *542*, 46–54. [[CrossRef](#)]
126. Alberts, S.; Rujopakarn, W.; Rieke, G.H.; Jagannathan, P.; Nyland, K. Completing the Census of AGN in GOODS-S/HUDF: New Ultradeep Radio Imaging and Predictions for JWST. *Astrophys. J.* **2020**, *901*, 168–188. [[CrossRef](#)]
127. Durré, M.; Mould, J. The AGN Ionization Cones of NGC 5728. I. Excitation and Nuclear Structure. *Astrophys. J.* **2018**, *867*, 149–174. [[CrossRef](#)]
128. Armus, L.; Charmandaris, V.; Bernard-Salas, J.; Spoon, H.W.W.; Marshall, J.A.; Higdon, S.J.U.; Desai, V.; Teplitz, H.I.; Hao, L.; Devost, D.; et al. Observations of Ultraluminous Infrared Galaxies with the Infrared Spectrograph on the Spitzer Space Telescope. II. The IRAS Bright Galaxy Sample. *Astrophys. J.* **2007**, *656*, 148–167. [[CrossRef](#)]
129. Levenson, N.A.; Sirocky, M.M.; Hao, L.; Spoon, H.W.W.; Marshall, J.A.; Elitzur, M.; Houck, J.R. Deep Mid-Infrared Silicate Absorption as a Diagnostic of Obscuring Geometry toward Galactic Nuclei. *Astrophys. J. Lett.* **2007**, *654*, L45–L48. [[CrossRef](#)]
130. Nikutta, R.; Elitzur, M.; Lacy, M. On the 10 μm Silicate Feature in Active Galactic Nuclei. *Astrophys. J.* **2009**, *707*, 1550–1559. [[CrossRef](#)]
131. Sirocky, M.M.; Levenson, N.A.; Elitzur, M.; Spoon, H.W.W.; Armus, L. Silicates in Ultraluminous Infrared Galaxies. *Astrophys. J.* **2008**, *678*, 729–743. [[CrossRef](#)]
132. Marshall, J.A.; Elitzur, M.; Armus, L.; Diaz-Santos, T.; Charmandaris, V. The Nature of Deeply Buried Ultraluminous Infrared Galaxies: A Unified Model for Highly Obscured Dusty Galaxy Emission. *Astrophys. J.* **2018**, *858*, 59–78. [[CrossRef](#)]
133. Spoon, H.W.W.; Marshall, J.A.; Houck, J.R.; Elitzur, M.; Hao, L.; Armus, L.; Brandl, B.R.; Charmandaris, V. Mid-Infrared Galaxy Classification Based on Silicate Obscuration and PAH Equivalent Width. *Astrophys. J. Lett.* **2007**, *654*, L49–L52. [[CrossRef](#)]
134. Barcos-Muñoz, L.; Leroy, A.K.; Evans, A.S.; Condon, J.; Privon, G.C.; Thompson, T.A.; Armus, L.; Díaz-Santos, T.; Mazzarella, J.M.; Meier, D.S.; et al. A 33 GHz Survey of Local Major Mergers: Estimating the Sizes of the Energetically Dominant Regions from High-resolution Measurements of the Radio Continuum. *Astrophys. J.* **2017**, *843*, 117–143. [[CrossRef](#)]
135. Iwasawa, K.; Sanders, D.B.; Teng, S.H.; Armus, L.; Evans, A.S.; Howell, J.H.; Komossa, S.; Mazzarella, J.M.; Petric, A.O.; Surace, J.A.; et al. C-GOALS: Chandra observations of a complete sample of luminous infrared galaxies from the IRAS Revised Bright Galaxy Survey. *Astron. Astrophys.* **2011**, *529*, 106–155. [[CrossRef](#)]
136. Yamada, S.; Ueda, Y.; Tanimoto, A.; Imanishi, M.; Toba, Y.; Ricci, C.; Privon, G.C. Comprehensive Broadband X-Ray and Multiwavelength Study of Active Galactic Nuclei in 57 Local Luminous and Ultraluminous Infrared Galaxies Observed with NuSTAR and/or Swift/BAT. *Astrophys. J. Suppl.* **2021**, *257*, 61–128. [[CrossRef](#)]
137. Eisenhardt, P.R.M.; Wu, J.; Tsai, C.-W.; Assef, R.; Benford, D.; Blain, A.; Bridge, C.; Condon, J.J.; Cushing, M.C.; Cutri, R.; et al. The First Hyper-luminous Infrared Galaxy Discovered by WISE. *Astrophys. J.* **2012**, *755*, 173–183. [[CrossRef](#)]
138. Wu, J.; Tsai, C.-W.; Sayers, J.; Benford, D.; Bridge, C.; Blain, A.; Eisenhardt, P.R.M.; Stern, D.; Petty, S.; Assef, R.; et al. Submillimeter Follow-up of WISE-selected Hyperluminous Galaxies. *Astrophys. J.* **2012**, *756*, 96–109. [[CrossRef](#)]
139. Tsai, C.-W.; Eisenhardt, P.R.M.; Wu, J.; Stern, D.; Assef, R.J.; Blain, A.W.; Bridge, C.R.; Benford, D.J.; Cutri, R.M.; Griffith, R.L.; et al. The Most Luminous Galaxies Discovered by WISE. *Astrophys. J.* **2015**, *805*, 90–104. [[CrossRef](#)]
140. Ross, N.P.; Hamann, F.; Zakamska, N.L.; Richards, G.T.; Villforth, C.; Strauss, M.A.; Greene, J.E.; Alexandroff, R.; Brandt, W.N.; Liu, G.; et al. Extremely red quasars from SDSS, BOSS and WISE: Classification of optical spectra. *Mon. Not. R. Astron. Soc.* **2015**, *453*, 3932–3952. [[CrossRef](#)]
141. Yan, W.; Hickox, R.C.; Hainline, K.N.; Stern, D.; Lansbury, G.; Alexander, D.M.; Hviding, R.E.; Assef, R.J.; Ballantyne, D.R.; Dipompeo, M.A.; et al. NuSTAR and Keck Observations of Heavily Obscured Quasars Selected by WISE. *Astrophys. J.* **2019**, *870*, 33–43. [[CrossRef](#)]
142. Vito, F.; Brandt, W.N.; Stern, D.; Assef, R.J.; Chen, C.-T.J.; Brightman, M.; Comastri, A.; Eisenhardt, P.; Garmire, G.P.; Hickox, R.; et al. Heavy X-ray obscuration in the most luminous galaxies discovered by WISE. *Mon. Not. R. Astron. Soc.* **2018**, *474*, 4528–4540. [[CrossRef](#)]
143. Zappacosta, L.; Piconcelli, E.; Duras, F.; Vignali, C.; Valiante, R.; Bianchi, S.; Bongiorno, A.; Fiore, F.; Feruglio, C.; Lanzuisi, G.; et al. The hyperluminous Compton-thick $z \sim 2$ quasar nucleus of the hot DOG W1835+4355 observed by NuSTAR. *Astron. Astrophys.* **2018**, *618*, 28–38. [[CrossRef](#)]

144. Finnerty, L.; Larson, K.; Soifer, B.T.; Armus, L.; Matthews, K.; Jun, H.D.; Moon, D.-S.; Melbourne, J.; Gomez, P.; Tsai, C.-W.; et al. Fast Outflows in Hot Dust-obscured Galaxies Detected with Keck/NIRES. *Astrophys. J.* **2020**, *905*, 16–35. [[CrossRef](#)]
145. Hamann, F.; Zakamska, N.L.; Ross, N.; Paris, I.; Alexandroff, R.M.; Villforth, C.; Richards, G.T.; Herbst, H.; Brandt, W.N.; Cook, B.; et al. Extremely red quasars in BOSS. *Mon. Not. R. Astron. Soc.* **2017**, *464*, 3431–3463. [[CrossRef](#)]
146. Calistro Rivera, G.; Alexander, D.M.; Rosario, D.J.; Harrison, C.M.; Stalevski, M.; Rakshit, S.; Fawcett, V.A.; Morabito, L.K.; Klindt, L.; Best, P.N.; et al. The multiwavelength properties of red QSOs: Evidence for dusty winds as the origin of QSO reddening. *Astron. Astrophys.* **2021**, *649*, A102–A122. [[CrossRef](#)]
147. Jun, H. D.; Assef, R.J.; Bauer, F.E.; Blain, A.; Díaz-Santos, T.; Eisenhardt, P.R.M.; Stern, D.; Tsai, C.-W.; Wright, E.; Wu, J. Spectral Classification and Ionized Gas Outflows in $z \sim 2$ WISE-selected Hot Dustobscured Galaxies. *Astrophys. J.* **2020**, *888*, 110–131. [[CrossRef](#)]
148. Zakamska, N.L.; Hamann, F.; Pâris, I.; Brandt, W.N.; Greene, J.E.; Strauss, M.A.; Villforth, C.; Wylezalek, D.; Alexandroff, R.M.; Ross, N.P. Discovery of extreme [O III] λ 5007 outflows in high-redshift red quasars. *Mon. Not. R. Astron. Soc.* **2016**, *459*, 3144–3160. [[CrossRef](#)]
149. Martínez-Paredes, M.; Aretxaga, I.; González-Martín, O.; Alonso-Herrero, A.; Levenson, N.A.; Ramos Almeida, C.; López-Rodríguez, E. Quantifying Star Formation Activity in the Inner 1 kpc of Local MIR Bright QSOs. *Astrophys. J.* **2019**, *871*, 190–197. [[CrossRef](#)]
150. Peletier, R.F.; Knapen, J.H.; Shlosman, I.; Pérez-Ramírez, D.; Nadeau, D.; Doyon, R.; Espinosa, J.M.R.; García, A.M.P. A Subarcsecond-Resolution Near-Infrared Study of Seyfert and “Normal” Galaxies. I. Imaging Data. *Astrophys. J. Suppl.* **1999**, *125*, 363–407. [[CrossRef](#)]
151. Winter, L.M.; Karen, T.; Lewis, K.T.; Koss, M.; Veilleux, S.; Keeney, B.; Mushotzky, R.F. Optical Spectral Properties of Swift Burst Alert Telescope Hard X-Ray-Selected Active Galactic Nuclei Sources. *Astrophys. J.* **2010**, *710*, 503–539. [[CrossRef](#)]
152. Lyu, J.; Rieke, G.H.; Alberts, S. The Contribution of Host Galaxies to the Infrared Energy Output of $z \gtrsim 5.0$ Quasars. *Astrophys. J.* **2016**, *816*, 85–107.
153. McLeod, K.K.; Rieke, G.H. Near-Infrared Imaging of Low-Redshift Quasar Host Galaxies. II. High-Luminosity Quasars, *ApJ*, **1994**, *431*, 137–146 [[CrossRef](#)]
154. Uchiyama, Y.; Urry, C.M.; Cheung, C.C.; Jester, S.; Van Duyne, J.; Coppi, P.; Sambruna, R.M.; Takahashi, T.; Tavecchio, F.; Maraschi, L. Shedding New Light on the 3C 273 Jet with the Spitzer Space Telescope. *Astrophys. J.* **2006**, *648*, 910–921. [[CrossRef](#)]
155. Urry, C.M.; Padovani, P. Unified Schemes for Radio-Loud Active Galactic Nuclei, *PASP*, **1995**, *107*, 803–845 [[CrossRef](#)]
156. Cleary, K.; Lawrence, C.R.; Marshall, J.A.; Hao, L.; Meier, D. Spitzer Observations of 3C Quasars and Radio Galaxies: Mid-Infrared Properties of Powerful Radio Sources. *Astrophys. J.* **2007**, *660*, 117–145. [[CrossRef](#)]
157. Shi, Y.; Rieke, G.H.; Hines, D.C.; Neugebauer, G.; Blaylock, M.; Rigby, J.; Egami, E.; Gordon, K.D.; Alonso-Herrero, A. Far-Infrared Observations of Radio Quasars and FR II Radio Galaxies. *Astrophys. J.* **2005**, *629*, 88–99. [[CrossRef](#)]
158. Westhues, C.; Haas, M.; Barthel, P.; Wilkes, B.J.; Willner, S.P.; Kuraszkiwicz, J.; Podigachoski, P.; Leipski, C.; Meisenheimer, K.; Siebenmorgen, R.; et al. Star Formation in 3CR Radio Galaxies and Quasars at $z < 1$. *Astrophys. J.* **2016**, *151*, 120.
159. Haas, M.; Willner, S.P.; Heymann, F.; Ashby, M.L.N.; Fazio, G.G.; Wilkes, B.J.; Chini, R.; Siebenmorgen, R. Near- and Mid-Infrared Photometry of High-Redshift 3CR Sources. *Astrophys. J.* **2008**, *688*, 122–127. [[CrossRef](#)]
160. Podigachoski, P.; Barthel, P.D.; Haas, M.; Leipski, C.; Wilkes, B.; Kuraszkiwicz, J.; Westhues, C.; Willner, S.P.; Ashby, M.L.N.; Chini, R.; et al. Star formation in $z > 1$ 3CR host galaxies as seen by Herschel. *Astron. Astrophys.* **2015**, *575*, A80. [[CrossRef](#)]
161. Brown, M.J.I.; Moustakas, J.; Smith, J.-D.T.; da Cunha, E.; Jarrett, T.H.; Imanishi, M.; Armus, L.; Brandl, B.R.; Peek, J.E.G. An Atlas of Galaxy Spectral Energy Distributions from the Ultraviolet to the Mid-infrared. *Astrophys. J. Suppl.* **2014**, *212*, 18–35. [[CrossRef](#)]
162. Mannucci, F.; Basile, F.; Poggianti, B.M.; Cimatti, A.; Daddi, E.; Pozzetti, L.; Vanzi, L. Near-infrared template spectra of normal galaxies: K-corrections, galaxy models and stellar populations. *Mon. Not. R. Astron. Soc.* **2001**, *326*, 745–758. [[CrossRef](#)]
163. Willner, S.P.; Ward, M.; Longmore, A.; Lawrence, A.; Fabbiano, G.; Elvis, M. JHKL photometry of the nuclei of normal spiral galaxies. *Publ. Astron. Soc. Pac.* **1984**, *96*, 143–147. [[CrossRef](#)]
164. da Cunha, E.; Charlot, S.; Elbaz, D. A simple model to interpret the ultraviolet, optical and infrared emission from galaxies. *Mon. Not. R. Astron. Soc.* **2008**, *388*, 1595–1617. [[CrossRef](#)]
165. Lyu, B.; Wu Q.; Yan, Z.; Yu, W.; Liu, H. WISE view of changing-look AGNs: Evidence for a transitional stage of AGNs. *Astrophys. J.* **2022**, *927*, 227–240. [[CrossRef](#)]
166. Fritz, J.; Franceschini, A.; Hatziminaoglou, E. Revisiting the infrared spectra of active galactic nuclei with a new torus emission model. *Mon. Not. R. Astron. Soc.* **2006**, *366*, 767–786. [[CrossRef](#)]
167. Nenkova, M.; Sirocky, M.M.; Nikutta, R.; Ivezić, Ž.; Elitzur, M. AGN Dusty Tori. II. Observational Implications of Clumpiness. *Astrophys. J.* **2008**, *685*, 160–180. [[CrossRef](#)]
168. Siebenmorgen, R.; Heymann, F.; Efstathiou, A. Self-consistent two-phase AGN torus models: SED library for observers. *Astron. Astrophys.* **2015**, *583*, 120–137. [[CrossRef](#)]
169. Stalevski, M.; Fritz, J.; Baes, M.; Nakos, T.; Popović, L.Č. 3D radiative transfer modelling of the dusty tori around active galactic nuclei as a clumpy two-phase medium. *Mon. Not. R. Astron. Soc.* **2012**, *420*, 2756–2772. [[CrossRef](#)]
170. Azadi, M.; Wilkes, B.; Kuraszkiwicz, J.; McDowell, J.; Siebenmorgen, R.; Ashby, M.; Birkinshaw, M.; Worrall, D.; Abrams, N.; Barthel, P.; et al. Disentangling the AGN and star-formation contributions to the radio-X-ray emission of radio-loud quasars at $1 < z < 2$. *arXiv* **2020**, arXiv:2011.03130.

171. Berta, S.; Lutz, D.; Santini, P.; Wuyts, S.; Rosario, D.; Brisbin, D.; Cooray, A.; Franceschini, A.; Gruppioni, C.; Hatziminaoglou, E.; et al. Panchromatic spectral energy distributions of Herschel sources. *Astron. Astrophys.* **2013**, *551*, 100–121. [[CrossRef](#)]
172. Brown, A.; Nayyeri, H.; Cooray, A.; Ma, J.; Hickox, R.C.; Azadi, M. Infrared Contributions of X-Ray Selected Active Galactic Nuclei in Dusty Star-forming Galaxies. *Astrophys. J.* **2019**, *871*, 87–100. [[CrossRef](#)]
173. Leja, J.; Johnson, B.D.; Conroy, C.; van Dokkum, P. Hot Dust in Panchromatic SED Fitting: Identification of Active Galactic Nuclei and Improved Galaxy Properties. *Astrophys. J.* **2018**, *854*, 62–80. [[CrossRef](#)]
174. Pouliaxis, E.; Mountrichas, G.; Georgantopoulos, I.; Ruiz, A.; Yang, M.; Bonanos, A.Z. An obscured AGN population hidden in the VIPERS galaxies: Identification through spectral energy distribution decomposition. *Mon. Not. R. Astron. Soc.* **2020**, *495*, 1853–1873. [[CrossRef](#)]
175. Shangguan, J.; Ho, L.C.; Xie, Y. On the Gas Content and Efficiency of AGN Feedback in Low-redshift Quasars. *Astrophys. J.* **2018**, *854*, 158. [[CrossRef](#)]
176. Yang, G.; Boquien, M.; Brandt, W.N.; Buat, V.; Burgarella, D.; Ciesla, L.; Lehmer, B.D.; Małek, K.; Mountrichas, G.; Papovich, C.; et al. Fitting AGN/Galaxy X-Ray-to-radio SEDs with CIGALE and Improvement of the Code. *ApJ* **2022**, *927*, 192–212 [[CrossRef](#)]
177. Yang, Q.; Shen, Y.; Liu, X.; Aguena, M.; Annis, J.; Avila, S.; Banerji, M.; Bertin, E.; Brooks, D.; Burke, D.; et al. Dust Reverberation Mapping in Distant Quasars from Optical and Mid-infrared Imaging Surveys. *Astrophys. J.* **2020**, *900*, 58–74. [[CrossRef](#)]
178. González-Martín, O.; Masegosa, J. García-Bernete, I.; Ramos Almeida, C.; Rodríguez-Espinosa, J.M.; Márquez, I.; Esparza-Arredondo, D.; Osorio-Clavijo, N.; Martínez-Paredes, M.; Victoria-Ceballos, C.; et al. Exploring the Mid-infrared SEDs of Six AGN Dusty Torus Models. II. The Data. *Astrophys. J.* **2019**, *884*, 11–33. [[CrossRef](#)]
179. Hernán-Caballero, A.; Alonso-Herrero, A.; Hatziminaoglou, E.; Spoon, H.W.W.; Ramos Almeida, C.; Díaz Santos, T.; Hönig, S.F.; González-Martín, O.; Esquej, P. Resolving the AGN and Host Emission in the Mid-infrared Using a Model-independent Spectral Decomposition. *Astrophys. J.* **2015**, *803*, 109. [[CrossRef](#)]
180. Nardini, E.; Risaliti, G.; Salvati, M.; Sani, E.; Imanishi, M.; Marconi, A.; Maiolino, R. Spectral decomposition of starbursts and active galactic nuclei in 5–8 μm Spitzer-IRS spectra of local ultraluminous infrared galaxies. *Mon. Not. R. Astron. Soc.* **2008**, *385*, L130–L134. [[CrossRef](#)]
181. Calistro Rivera, G.; Lusso, E.; Hennawi, J.F.; Hogg, D.W. AGNfitter: A Bayesian MCMC Approach to Fitting Spectral Energy Distributions of AGNs. *Astrophys. J.* **2016**, *833*, 98–117. [[CrossRef](#)]
182. Lyu, J.; Alberts, S.; Rieke, G.H.; Rujopakarn, W. AGN Selection and Demographics in GOODS-S/HUDF from X-ray to Radio. *Astrophys. J.* **2022**. *submitted*.
183. Ichikawa, K.; Ricci, C.; Ueda, Y.; Bauer, F.E.; Kawamuro, T.; Koss, M.J.; Oh, K.; Rosario, D.J.; Shimizu, T.T.; Stalevski, M.; et al. BAT AGN Spectroscopic Survey. XI. The Covering Factor of Dust and Gas in Swift/BAT Active Galactic Nuclei. *Astrophys. J.* **2019**, *870*, 31. [[CrossRef](#)]
184. Mullaney, J.R.; Pannella, M.; Daddi, E.; Alexander, D.M.; Elbaz, D.; Hickox, R.C.; Bournaud, F.; Altieri, B.; Aussel, H.; Coia, D.; et al. GOODS-Herschel: The far-infrared view of star formation in active galactic nucleus host galaxies since $z \approx 3$. *Mon. Not. R. Astron. Soc.* **2012**, *419*, 95–115. [[CrossRef](#)]
185. Ciesla, L.; Charmandaris, V.; Georgakakis, A.; Bernhard, E.; Mitchell, P.D.; Buat, V.; Elbaz, D.; LeFloc'h, E.; Lacey, C.G.; Magdis, G.E.; et al. Constraining the properties of AGN host galaxies with spectral energy distribution modelling. *Astron. Astrophys.* **2015**, *576*, 10–28. [[CrossRef](#)]
186. De Rossi, M.E.; Rieke, G.H.; Shivaee, I.; Bromm, V.; Lyu, J. The Far-infrared Emission of the First Massive Galaxies. *Astrophys. J.* **2018**, *869*, 4–17. [[CrossRef](#)]
187. Dai, Y.S.; Wilkes, B.J.; Bergeron, J.; Kuraszkiewicz, J.; Omont, A.; Atanas, A.; Teplitz, H.I. Is there a relationship between AGN and star formation in IR-bright AGNs? *Mon. Not. R. Astron. Soc.* **2018**, *478*, 4238–4254. [[CrossRef](#)]
188. Zhang, Z.; Shi, Y.; Rieke, G.H.; Xia, X.; Wang, Y.; Sun, B.; Wan, L. Distributions of Quasar Hosts on the Galaxy Main Sequence Plane. *Astrophys. J. Lett.* **2016**, *819*, 27–32. [[CrossRef](#)]
189. Hatcher, C.; Kirkpatrick, A.; Fornasini, F.; Civano, F.; Lambides, E.; Kocsevski, D.; Carroll, C.M.; Giavalisco, M.; Hickox, R.; Ji, Z. Where Do Obscured AGN Fit in a Galaxy's Timeline? *Astrophys. J.* **2021**, *162*, 65–77. [[CrossRef](#)]
190. Li, J.; Xue, Y.; Sun, M.; Brandt, W.N.; Yang, G.; Vito, F.; Tozzi, P.; Vignali, C.; Comastri, A.; Shu, X.; et al. Piercing through Highly Obscured and Compton-thick AGNs in the Chandra Deep Fields. II. Are Highly Obscured AGNs the Missing Link in the Merger-triggered AGN-Galaxy Coevolution Models? *Astrophys. J.* **2020**, *903*, 49–66. [[CrossRef](#)]
191. Rosario, D.J.; Trakhtenbrot, B.; Lutz, D.; Netzer, H.; Trump, J.R.; Silverman, J.D.; Schramm, M.; Lusso, E.; Berta, S.; Bongiorno, A.; et al. The mean star-forming properties of QSO host galaxies. *Astron. Astrophys.* **2013**, *560*, 72–85. [[CrossRef](#)]
192. Santini, P.; Rosario, D.J.; Shao, L.; Lutz, D.; Maiolino, R.; Alexander, D.M.; Altieri, B.; Andreani, P.; Aussel, H.; Bauer, F.E.; et al. Enhanced star formation rates in AGN hosts with respect to inactive galaxies from PEP-Herschel observations. *Astron. Astrophys.* **2012**, *540*, A109–A128. [[CrossRef](#)]
193. Ji, Z.; Giavalisco, M.; Kirkpatrick, A.; Kocevski, D.; Daddi, E.; Delvecchio, I.; Hatcher, C. AGN Selection Methods Have Profound Impacts on the Distributions of Host-galaxy Properties. *Astrophys. J.* **2022**, *925*, 74–99. [[CrossRef](#)]
194. Barrows, R.S.; Comerford, J.M.; Stern, D.; Assef, R.J. A Catalog of Host Galaxies for WISE-selected AGN: Connecting Host Properties with Nuclear Activity and Identifying Contaminants. *Astrophys. J.* **2021**, *922*, 179–193. [[CrossRef](#)]
195. Polimera, M.; Sarajedini, V.; Ashby, M.L.N.; Willner, S.P.; Fazio, G.G. Morphologies of mid-IR variability-selected AGN host galaxies. *Mon. Not. R. Astron. Soc.* **2018**, *476*, 1111–1119. [[CrossRef](#)]

196. Kocevski, D.D.; Faber, S.M.; Mozena, M.; Koekemoer, A.M.; Nandra, K.; Rangel, C.; Laird, E.S.; Brusa, M.; Wuyts, S.; Trump, J.R.; et al. CANDELS: Constraining the AGN-Merger Connection with Host Morphologies at $z \sim 2$. *Astrophys. J.* **2012**, *744*, 148–156. [[CrossRef](#)]
197. Kocevski, D.D.; Brightman, M.; Nandra, K.; Koekemoer, A.M.; Salvato, M.; Aird, J.; Bell, E.F.; Hsu, L.-T.; Kartaltepe, J.S.; Koo, D.C.; et al. Are Compton-thick AGNs the Missing Link between Mergers and Black Hole Growth? *Astrophys. J.* **2015**, *814*, 104–115. [[CrossRef](#)]
198. Shah, E.A.; Kartaltepe, J.S.; Magagnoli, C.T.; Cox, I.G.; Wetherell, C.T.; Vanderhoof, B.N.; Calabro, A.; Chartab, N.; Conselice, C.J.; Croton, D.J.; et al. Investigating the Effect of Galaxy Interactions on the Enhancement of Active Galactic Nuclei at $0.5 < z < 3.0$. *Astrophys. J.* **2020**, *904*, 107–127.
199. Dahmer-Hahn, L.G.; Riffel, R.; Rodríguez-Ardila, A.; Riffel, R.A.; Storchi-Bergmann, T.; Marinello, M.; Davies, R.I.; Burtscher, L.; Ruschel-Dutra, D.; Rosario, D.J. Stellar populations in local AGNs: Evidence for enhanced star formation in the inner 100 pc. *Mon. Not. R. Astron. Soc.* **2022**, *509*, 4653–4668. [[CrossRef](#)]
200. Zhuang, M.-Y.; Ho, L.C. The Interplay between Star Formation and Black Hole Accretion in Nearby Active Galaxies. *Astrophys. J.* **2020**, *896*, 108–120. [[CrossRef](#)]
201. Suh, H.; Civano, F.; Hasinger, G.; Lusso, E.; Marchesi, S.; Schulze, A.; Onodera, M.; Rosario, D.J.; Sanders, D.B. Multi-wavelength Properties of Type 1 and Type 2 AGN Host Galaxies in the Chandra-COSMOS Legacy Survey. *Astrophys. J.* **2019**, *872*, 168–185. [[CrossRef](#)]
202. Maiolino, R.; Ruiz, M.; Rieke, G.H.; Keller, L.D. New Constraints on the Unified Model of Seyfert Galaxies. *Astrophys. J.* **1995**, *446*, 561–573. [[CrossRef](#)]
203. Buchanan, C.L.; Gallimore, J.F.; O’Dea, C.P.; Baum, S.A.; Axon, D.J.; Robinson, A.; Elitzur, M.; Elvis, M. Spitzer IRS Spectra of a Large Sample of Seyfert Galaxies: A Variety of Infrared Spectral Energy Distributions in the Local Active Galactic Nucleus Population. *Astrophys. J.* **2006**, *132*, 401–409.
204. Meléndez, M.; Kraemer, S.B.; Schmitt, H.R.; Crenshaw, D.M.; Deo, R.P.; Mushotzky, R.F.; Bruhweiler, F.C. Constraining the Active Galactic Nucleus Contribution in a Multiwavelength Study of Seyfert Galaxies. *Astrophys. J.* **2008**, *689*, 95–107. [[CrossRef](#)]
205. Masoura, V.A.; Mountrichas, G.; Georgantopoulos, I.; Plionis, M. Relation between AGN type and host galaxy properties. *Astron. Astrophys.* **2021**, *646*, 167–177. [[CrossRef](#)]
206. Nikutta, R.; Lopez-Rodríguez, E.; Ichikawa, K.; Levenson, N.A.; Packham, C.; Hönig, S.F.; Alonso-Herrero, A. Hypercubes of AGN Tori (HYPERCAT). I. Models and Image Morphology. *Astrophys. J.* **2021**, *919*, 136–156. [[CrossRef](#)]
207. Zou, F.; Yang, G.; Brandt, W.N.; Xue, Y. The Host-galaxy Properties of Type 1 versus Type 2 Active Galactic Nuclei. *Astrophys. J.* **2019**, *878*, 11–26. [[CrossRef](#)]
208. Kalfountzou, E. The Evolution of AGN and Their Host Galaxies. Ph.D. Thesis, University of Hertfordshire, Hertfordshire, UK, July 2015.
209. Meidt, S.E.; Schinnerer, E.; van de Ven, G.; Zaritsky, D.; Peletier, R.; Knapen, J.H.; Sheth, K.; Regan, M.; Querejeta, M.; Muñoz-Mateos, J.-C.; et al. Reconstructing the Stellar Mass Distributions of Galaxies Using S⁴G IRAC 3.6 and 4.5 μ m Images. II. The Conversion from Light to Mass. *Astrophys. J.* **2014**, *788*, 144–155. [[CrossRef](#)]
210. Wen, X.Q.; Wu, H.; Zhu, Y.N.; Lam, M.I.; Wu, C.J.; Wicker, J.; Zhao, Y.H. The stellar masses of galaxies from the 3.4 μ m band of the WISE All-Sky Survey. *Mon. Not. R. Astron. Soc.* **2013**, *433*, 2946–2957. [[CrossRef](#)]
211. Rieke, G.H.; Alonso-Herrero, A.; Weiner, B.J.; Pérez-González, P.G.; Blaylock, M.; Donley, J.L.; Marcillac, D. Determining Star Formation Rates for Infrared Galaxies. *Astrophys. J.* **2009**, *692*, 556–573. [[CrossRef](#)]
212. Sitko, M.L.; Sitko, A.K.; Siemiginowska, A.; Szczerba, R. Multifrequency Observations of the Optically Active Radio-quiet Quasar GQ Comae. II. Ultraviolet, Optical, and Infrared Continuum Variability. *Astrophys. J.* **1993**, *409*, 139–148. [[CrossRef](#)]
213. Horne, K.; Peterson, B.M.; Collier, S.J.; Netzer, H. Observational Requirements for High-Fidelity Reverberation Mapping. *Publ. Astron. Soc. Pac.* **2004**, *116*, 465–476. [[CrossRef](#)]
214. Kozłowski, S. Limitations on the recovery of the true AGN variability parameters using damped random walk modeling. *Astron. Astrophys.* **2017**, *597*, 128–134. [[CrossRef](#)]
215. Lyuty, V.M.; Taranova, O.G.; Shenavrin, V.I. Nuclear variability of NGC 4151 in UVB and JHKL: A new cycle of activity. *Ast. Lett.* **1998**, *24*, 199–205.
216. Oknyansky, V.L.; Shenavrin, V.I.; Metlova, N.V.; Gaskell, C.M. Additional Support for Relative Wavelength Independence of IR Lags in NGC 4151 Over the Past Decade. *Odessa Astron. Publ.* **2018**, *31*, 94–99. [[CrossRef](#)]
217. Shenavrin, V.I.; Taranova, O.G.; Nadzhip, A.E. Search for and study of hot circumstellar dust envelopes. *Ast. Reports* **2011**, *55*, 31–81. [[CrossRef](#)]
218. Taranova, O.G.; Shenavrin, V.I. Activity of the Seyfert galaxy NGC 4151 in the near-IR in 1994–2011. *Ast. Reports* **2013**, *57*, 71–83. [[CrossRef](#)]
219. Peterson, B.M.; Pogge, R.W.; Wanders, I.; Smith, S.M.; Romanishin, W. Aperture Effects and Limitations on the Accuracy of Ground-Based Spectrophotometry of Active Galactic Nuclei. *Publ. Astron. Soc. Pac.* **1995**, *107*, 759–769. [[CrossRef](#)]
220. Yoshii, Y.; Tomita, H.; Kobayashi, Y.; Deng, J.; Maeda, K.; Nomoto, K.; Mazzali, P.A.; Umeda, H.; Aoki, T.; Doi, M.; et al. The Optical/Near-Infrared Light Curves of SN 2002ap for the First 140 Days after Discovery. *Astrophys. J.* **2003**, *592*, 467–474. [[CrossRef](#)]

221. Minezaki, T.; Yoshii, Y.; Kobayashi, Y.; Enya, K.; Suganuma, M.; Tomita, H.; Aoki, T.; Peterson, B.A. Inner Size of a Dust Torus in the Seyfert 1 Galaxy NGC 4151. *Astrophys. J. Lett.* **2004**, *600*, 35–38. [[CrossRef](#)]
222. Suganuma, M.; Yoshii, Y.; Kobayashi, Y.; Minezaki, T.; Enya, K.; Tomita, H.; Aoki, T.; Koshida, S.; Peterson, B.A. Reverberation Measurements of the Inner Radius of the Dust Torus in Nearby Seyfert 1 Galaxies. *Astrophys. J.* **2006**, *639*, 46–63. [[CrossRef](#)]
223. Koshida, S.; Minezaki, T.; Yoshii, Y.; Kobayashi, Y.; Sakata, Y.; Sugawara, S.; Enya, K.; Suganuma, M.; Tomita, H.; Aoki, T.; et al. Reverberation Measurements of the Inner Radius of the Dust Torus in 17 Seyfert Galaxies. *Astrophys. J.* **2014**, *788*, 159–179. [[CrossRef](#)]
224. Minezaki, T.; Yoshii, Y.; Kobayashi, Y.; Sugawara, S.; Sakata, Y.; Enya, K.; Koshida, S.; Tomita, H.; Suganuma, M.; Aoki, T.; et al. Reverberation Measurements of the Inner Radii of the Dust Tori in Quasars. *Astrophys. J.* **2019**, *856*, 150–173. [[CrossRef](#)]
225. Sobrino Figaredo, C.; Haas, M.; Ramolla, M.; Chini, R.; Blex, J.; Hodapp, K.W.; Murphy, M.; Kollatschny, W.; Chelouche, D.; Kaspi, S. Dust Reverberation of 3C 273: Torus Structure and Lag-Luminosity Relation. *Astrophys. J.* **2020**, *159*, 259–276.
226. Landt, H.; Ward, M.J.; Kynoch, D.; Packham, C.; Ferland, G.J.; Lawrence, A.; Pott, J.-U.; Esser, J.; Horne, K.; Starkey, D.A.; et al. The first spectroscopic dust reverberation programme on active galactic nuclei: The torus in NGC 5548. *Mon. Not. R. Astron. Soc.* **2019**, *489*, 1572–1589. [[CrossRef](#)]
227. Lira, P.; Arévalo, P.; Uttley, P.; McHardy, I.M.M.; Videla, L. Long-term monitoring of the archetype Seyfert galaxy MCG-6-30-15: X-ray, optical and near-IR variability of the corona, disc and torus. *Mon. Not. R. Astron. Soc.* **2015**, *454*, 368–379. [[CrossRef](#)]
228. Lira, P.; Arévalo, P.; Uttley, P.; McHardy, I.M.M.; Videla, L. Optical and near-IR long-term monitoring of NGC 3783 and MR 2251-178: Evidence for variable near-IR emission from thin accretion discs. *Mon. Not. R. Astron. Soc.* **2011**, *415*, 1290–1303. [[CrossRef](#)]
229. Pozo Nuñez, F.; Ramolla, M.; Westhues, C.; Haas, M.; Chini, R.; Steenbrugge, K.; Barr Domínguez, A.; Kaderhandt, L.; Hackstein, M.; Kollatschny, W.; et al. The broad-line region and dust torus size of the Seyfert 1 galaxy PGC 50427. *Astron. Astrophys.* **2015**, *576*, A73–A83. [[CrossRef](#)]
230. Ramolla, M.; Haas, M.; Westhues, C.; Pozo Nuñez, F.; Sobrino Figaredo, C.; Blex, J.; Zetzl, M.; Kollatschny, W.; Hodapp, K.W.; Chini, R.; et al. Simultaneous H α and dust reverberation mapping of 3C 120: Testing the bowl-shaped torus geometry. *Astron. Astrophys.* **2018**, *620A*, A137–A152. [[CrossRef](#)]
231. Mandal, A.K.; Rakshit, S.; Kurian, K.S.; Stalin, C.S.; Mathew, B.; Hoenig, S.; Gandhi, P.; Sagar, R.; Pandge, M.B. Determination of the size of the dust torus in H0507+164 through optical and infrared monitoring. *Mon. Not. R. Astron. Soc.* **2018**, *475*, 5330–5337. [[CrossRef](#)]
232. Mandal, A.K.; Rakshit, S.; Stalin, C.S.; Wylezalek, D.; Patig, M.K.; Sagar, R.; Mathew, B.; Muneer, S.; Pal, I. Dust reverberation mapping of Z229-15. *Mon. Not. R. Astron. Soc.* **2021**, *501*, 3905–3915. [[CrossRef](#)]
233. Vazquez, B.; Galianni, P.; Richmond, M.; Robinson, A.; Axon, D.J.; Horne, K.; Almeyda, T.; Fausnaugh, M.; Peterson, B.M.; Bottorff, M.; et al. Spitzer Space Telescope Measurements of Dust Reverberation Lags in the Seyfert 1 Galaxy NGC 6418. *ApJ* **2015**, *801*, 127. [[CrossRef](#)]
234. Jun, H.D.; Stern, D.; Graham, M.J.; Djorgovski, S.G.; Mainzer, A.; Cutri, R.M.; Drake, A.J.; Mahabal, A.A. Infrared Time Lags for the Periodic Quasar PG 1302-102. *Astrophys. J. Lett.* **2015**, *814*, 12–16. [[CrossRef](#)]
235. Noda, H.; Kawamuro, T.; Kokubo, M.; Minezaki, T. Dust reverberation mapping of type 2 AGN NGC 2110 realized with X-ray and 3–5 μ m IR monitoring. *Mon. Not. R. Astron. Soc.* **2020**, *495*, 2921–2929. [[CrossRef](#)]
236. Dexter, J.; Shangquan, J.; Hönig, S.; Kishimoto, M.; Lutz, D.; Netzer, H.; Davies, R.; Sturm, E.; Pfuhl, O.; Amorim, A.; et al. The resolved size and structure of hot dust in the immediate vicinity of AGN. *Astron. Astrophys.* **2020**, *635*, 92–105.
237. Pfuhl, O.; Davies, R.; Dexter, J.; Netzer, H.; Hönig, S.; Lutz, D.; Schartmann, M.; Sturm, E.; Amorim, A.; Brandner, W.; et al. An image of the dust sublimation region in the nucleus of NGC 1068. *Astron. Astrophys.* **2020**, *634*, 1–12.
238. Amorim, A.; Bauböck, M.; Brandner, W.; Bolzer, M.; Clénet, Y.; Davies, R.; de Zeeuw, P.T.; Dexter, J.; Drescher, A.; Eckart, A.; et al. The central parsec of NGC 3783: A rotating broad emission line region, asymmetric hot dust structure, and compact coronal line region. *Astron. Astrophys.* **2021**, *648*, 117–140.
239. Oknyansky, V.L.; Gaskell, C.M.; Shimanovskaya, E.V. The Relative Wavelength Independence of IR Lags in Active Galactic Nuclei: Implications for the Distribution of the Hot Dust. *Odessa Astron. Publ.* **2015**, *28*, 175–180. [[CrossRef](#)]
240. Koshida, S.; Yoshii, Y.; Kobayashi, Y.; Minezaki, T.; Sakata, Y.; Sugawara, S.; Enya, K.; Suganuma, M.; Tomita, H.; Aoki, T.; et al. Variation of Inner Radius of Dust Torus in NGC4151. *Astrophys. J. Lett.* **2009**, *700*, 109–113. [[CrossRef](#)]
241. Oknyanskij, V.L.; Lyuty, V.M.; Taranova, O.G.; Shenavrin, V.I. Correlation between the infrared and optical variations of NGC 4151 in 30 years: Change in the sizes of the infrared source. *Astron. Lett.* **1999**, *25*, 483–492.
242. Hönig, S.F.; Watson, D.; Kishimoto, M.; Hjorth, J. A dust-parallax distance of 19 megaparsecs to the supermassive black hole in NGC 4151. *Nature* **2014**, *515*, 528–530. [[CrossRef](#)]
243. Burtscher, L.; Jaffe, W.; Raban, D.; Meisenheimer, K.; Tristram, K.R.W.; Röttgering, H. Dust Emission from a Parsec-Scale Structure in the Seyfert 1 Nucleus of NGC 4151. *Astrophys. J. Lett.* **2009**, *705*, 53–57. [[CrossRef](#)]
244. Almeyda, T.R. Dusty Donuts: Modeling the Reverberation Response of the Circumnuclear Dusty Torus Emission in AGN. Ph.D. Thesis, Rochester Institute of Technology, Rochester, NY, USA, 2017.
245. Almeyda, T.R.; Robinson, A.; Richmond, M.; Nikutta, R.; McDonough, B. Modeling the Infrared Reverberation Response of the Circumnuclear Dusty Torus in AGNs: An Investigation of Torus Response Functions. *Astrophys. J.* **2020**, *891*, 26–63. [[CrossRef](#)]
246. Shakura N.I.; Sunyaev R.A. Black holes in binary systems. Observational appearance. *Astron. Astrophys.* **1973**, *24*, 33–51.

247. Gaskell, C.M. Accretion Disks and the Nature and Origin of AGN Continuum Variability. *Nucl. Reg. Host Galaxy Environ. Act. Galaxies* **2008**, *32*, 1–11.
248. Kishimoto, M.; Antonucci, R.; Blaes, O.; Lawrence, A.; Boisson, C.; Albrecht, M.; Leipski, C. The characteristic blue spectra of accretion disks in quasars as uncovered in the infrared. *Nature* **2008**, *454*, 492–494. [[CrossRef](#)]
249. García-Bernete, I.; Ramos Almeida, C.; Alonso-Herrero, A.; Ward, M.J.; Acosta-Pulido, J.A.; Pereira-Santaella, M.; Hernán-Caballero, A.; Asensio Ramos, A.; González-Martín, O.; Levenson, N.A.; et al. Torus model properties of an ultra-hard X-ray selected sample of Seyfert galaxies. *Mon. Not. R. Astron. Soc.* **2019**, *486*, 4917–4935. [[CrossRef](#)]
250. Schnülle, K.; Pott, J.-U.; Rix, H.-W.; Peterson, B.M.; De Rosa, G.; Shappee, B. Monitoring the temperature and reverberation delay of the circumnuclear hot dust in NGC 4151. *Astron. Astrophys.* **2015**, *578*, A57–A74. [[CrossRef](#)]
251. Osterbrock, D.E.; De Robertis, M.M. Optical spectra of IRAS “warm” galaxies. *Publ. Astron. Soc. Pac.* **1985**, *97*, 1129–1141. [[CrossRef](#)]
252. Cutri, R.M.; Nelson, B.O.; Huchra, J.P.; Smith, P.S. The 2MASS Red AGN Survey. *Bull. Am. Astron. Soc.* **2000**, *197*, ID 74.08. [[CrossRef](#)]
253. Laurent, O.; Mirabel, I.F.; Charmandaris, V.; Gallais, P.; Madden, S.C.; Sauvage, M.; Vigroux, L.; Cesarsky, C. Mid-infrared diagnostics to distinguish AGNs from starbursts. *Astron. Astrophys.* **2000**, *359*, 887–899.
254. Leipski, C.; Haas, M.; Meusinger, H.; Siebenmorgen, R.; Chini, R.; Scheyda, C.M.; Albrecht, M.; Wilkes, B.J.; Huchra, J.P.; Ott, S.; et al. The ISO-2MASS AGN survey: On the type-1 sources. *Astron. Astrophys.* **2005**, *440*, L5–L8. [[CrossRef](#)]
255. Lacy, M.; Storrie-Lombardi, L.J.; Sajina, A.; Appleton, P.N.; Armus, L.; Chapman, S.C.; Choi, P.I.; Fadda, D.; Fang, F.; Frayer, D.T.; et al. Obscured and Unobscured Active Galactic Nuclei in the Spitzer Space Telescope First Look Survey. *Astrophys. J. Suppl.* **2004**, *154*, 166–169. [[CrossRef](#)]
256. Stern, D.; Eisenhardt, P.; Gorjian, V.; Kochanek, C.S.; Caldwell, N.; Eisenstein, D.; Brodwin, M.; Brown, M.J.I.; Cool, R.; Dey, A.; et al. Mid-Infrared Selection of Active Galaxies. *Astrophys. J.* **2005**, *631*, 163–168. [[CrossRef](#)]
257. İköz, T.; Peletier, R.F.; Barthel, P.D.; Yeşilyaprak, C. Infrared-detected AGNs in the local Universe. *Astron. Astrophys.* **2020**, *640*, 68–77. [[CrossRef](#)]
258. Veilleux, S.; Rupke, D.S.N.; Kim, D.-C.; Genzel, R.; Sturm, E.; Lutz, D.; Contursi, A.; Schweitzer, M.; Tacconi, L.J.; Netzer, H.; et al. Spitzer Quasar and Ulirg Evolution Study (QUEST). IV. Comparison of 1 Jy Ultraluminous Infrared Galaxies with Palomar-Green Quasars. *Astrophys. J. Suppl.* **2009**, *182*, 628–666. [[CrossRef](#)]
259. Alonso-Herrero, A.; Pérez-González, P.G.; Alexander, D.M.; Rieke, G.H.; Rigopoulou, D.; Le Floch, E.; Barmby, P.; Papovich, C.; Rigby, J.R.; Bauer, F.E.; et al. Infrared Power-Law Galaxies in the Chandra Deep Field-South: Active Galactic Nuclei and Ultraluminous Infrared Galaxies. *Astrophys. J.* **2006**, *640*, 167–184. [[CrossRef](#)]
260. Donley, J.L.; Rieke, G.H.; Pérez-González, P.G.; Rigby, J.R.; Alonso-Herrero, A. Spitzer Power-Law Active Galactic Nucleus Candidates in the Chandra Deep Field-North. *Astrophys. J.* **2007**, *660*, 167–190. [[CrossRef](#)]
261. Donley, J.L.; Koekemoer, A.M.; Brusa, M.; Capak, P.; Cardamone, C.N.; Civano, F.; Ilbert, O.; Impey, C.D.; Kartaltepe, J.S.; Miyaji, T.; et al. Identifying Luminous Active Galactic Nuclei in Deep Surveys: Revised IRAC Selection Criteria. *Astrophys. J.* **2012**, *748*, 142–163. [[CrossRef](#)]
262. Hickox, R.C.; Jones, C.; Forman, W.R.; Murray, S.S.; Brodwin, M.; Brown, M.J.I.; Eisenhardt, P.R.; Stern, D.; Kochanek, C.S.; Eisenstein, D.; et al. A Large Population of Mid-Infrared-selected, Obscured Active Galaxies in the Boötes Field. *Astrophys. J.* **2007**, *671*, 1365–1387. [[CrossRef](#)]
263. Del Moro, A.; Alexander, D.M.; Bauer, F.E.; Daddi, E.; Kocevski, D.D.; McIntosh, D.H.; Stanley, F.; Brandt, W.N.; Elbaz, D.; Harrison, C.M.; et al. Mid-infrared luminous quasars in the GOODS-Herschel fields: A large population of heavily obscured, Compton-thick quasars at $z \approx 2$. *Mon. Not. R. Astron. Soc.* **2016**, *456*, 2105–2125. [[CrossRef](#)]
264. Assef, R.J.; Stern, D.; Noirot, G.; Jun, H.D.; Cutri, R.M.; Eisenhardt, P.R.M. The WISE AGN Catalog. *Astrophys. J. Suppl.* **2018**, *234*, 23–44. [[CrossRef](#)]
265. Asmus, D.; Greenwell, C.L.; Gandhi, P.; Boorman, P.G.; Aird, J.; Alexander, D.M.; Assef, R.J.; Baldi, R.D.; Davies, R.I.; Höning, S.F.; et al. Local AGN survey (LASr): I. Galaxy sample, infrared colour selection, and predictions for AGN within 100 Mpc. *Mon. Not. R. Astron. Soc.* **2020**, *494*, 1784–1816. [[CrossRef](#)]
266. Carroll, C.M.; Hickox, R.C.; Masini, A.; Lanz, L.; Assef, R.J.; Stern, D.; Chen, C.-T.J.; Ananna, T.T. A Large Population of Luminous Active Galactic Nuclei Lacking X-Ray Detections: Evidence for Heavy Obscuration? *Astrophys. J.* **2021**, *908*, 185–196. [[CrossRef](#)]
267. Hainline, K.N.; Hickox, R.C.; Carroll, C.M.; Myers, A.D.; DiPompeo, M.A.; Trouille, L. A Spectroscopic Survey of WISE-selected Obscured Quasars with the Southern African Large Telescope. *Astrophys. J.* **2014**, *795*, 124–142. [[CrossRef](#)]
268. Hviding, R.E.; Hickox, R.C.; Hainline, K.N.; Carroll, C.M.; DiPompeo, M.A.; Yan, W.; Jones, M.L. Characterizing the WISE-selected heavily obscured quasar population with optical spectroscopy from the Southern African Large Telescope. *Mon. Not. R. Astron. Soc.* **2018**, *474*, 1955–1969. [[CrossRef](#)]
269. Jarrett, T.H.; Cohen, M.; Masci, F.; Wright, E.; Stern, D.; Benford, D.; Blain, A.; Carey, S.; Cutri, R.M.; Eisenhardt, P.; et al. The Spitzer-WISE Survey of the Ecliptic Poles. *Astrophys. J.* **2011**, *735*, 112–144. [[CrossRef](#)]
270. Mateos, S.; Alonso-Herrero, A.; Carrera, F.J.; Blain, A.; Watson, M.G.; Barcons, X.; Braitto, V.; Severgnini, P.; Donley, J.L.; Stern, D. Using the Bright Ultrahard XMM-Newton survey to define an IR selection of luminous AGN based on WISE colours. *Mon. Not. R. Astron. Soc.* **2012**, *426*, 3271–3281. [[CrossRef](#)]

271. Secrest, N.J.; Dudik, R.P.; Dorland, B.N.; Zacharias, N.; Makarov, V.; Fey, A.; Frouard, J.; Finch, C. Identification of 1.4 Million Active Galactic Nuclei in the Mid-Infrared using WISE Data. *Astrophys. J. Suppl.* **2015**, *221*, 12–21. [[CrossRef](#)]
272. Stern, D.; Assef, R.J.; Benford, D.J.; Blain, A.; Cutri, R.; Dey, A.; Eisenhardt, P.; Griffith, R.L.; Jarrett, T.H.; Lake, S.; et al. Mid-infrared Selection of Active Galactic Nuclei with the Wide-Field Infrared Survey Explorer. I. Characterizing WISE-selected Active Galactic Nuclei in COSMOS. *Astrophys. J.* **2012**, *753*, 30–47. [[CrossRef](#)]
273. Hviding, R.E.; Hainline, K.N.; Rieke, M.; Juneau, S.; Lyu, J.; Pucha, R. A New Infrared Criterion for Selecting Active Galactic Nuclei to Lower Luminosities. *AJ* **2022**, *163*, 224–248 [[CrossRef](#)]
274. Gandhi, P.; Horst, H.; Smette, A.; Hönig, S.; Comastri, A.; Gilli, R.; Vignali, C.; Duschl, W. Resolving the mid-infrared cores of local Seyferts. *Astron. Astrophys.*, **2009** *502*, 457–472. [[CrossRef](#)]
275. Boorman, P.G.; Gandhi, P.; Alexander, D.M.; Annuar, A.; Ballantyne, D.R.; Bauer, F.; Boggs, S.E.; Brandt, W.N.; Brightman, M.; Christensen, F.E.; et al. IC 3639—A New Bona Fide Compton-Thick AGN Unveiled by NuSTAR. *Astrophys. J.* **2016**, *833*, 245–262. [[CrossRef](#)]
276. LaMassa, S.M.; Yaqoob, T.; Boorman, P.G.; Tzanavaris, P.; Levenson, N.A.; Gandhi, P.; Ptak, A.F.; Heckman, T.M. NuSTAR Uncovers an Extremely Local Compton-thick AGN in NGC 4968. *Astrophys. J.* **2019**, *887*, 173–186. [[CrossRef](#)]
277. Lam, A.; Malkan, M.; Wright, E. Far-infrared dust properties of highly dust-obscured active galactic nuclei from the AKARI and WISE all-sky surveys. *PASJ* **2019**, *71*, 9–24. [[CrossRef](#)]
278. Kirkpatrick, A.; Pope, A.; Charmandaris, V.; Daddi, E.; Elbaz, D.; Hwang, H.S.; Pannella, M.; Scott, D.; Altieri, B.; Aussel, H.; et al. GOODS-Herschel: Separating High-redshift Active Galactic Nuclei and Star-forming Galaxies Using Infrared Color Diagnostics. *Astrophys. J.* **2013**, *763*, 123–134. [[CrossRef](#)]
279. Kirkpatrick, A.; Alberts, S.; Pope, A.; Barro, G.; Bonato, M.; Kocevski, D.D.; Pérez-González, P.; Rieke, G.H.; Rodríguez-Muñoz, L.; Sajina, A.; et al. The AGN-Star Formation Connection: Future Prospects with JWST. *Astrophys. J.* **2017**, *849*, 111–125. [[CrossRef](#)]
280. Messias, H.; Afonso, J.; Salvato, M.; Mobasher, B.; Hopkins, A.M. A New Infrared Color Criterion for the Selection of $0 < z < 7$ AGNs: Application to Deep Fields and Implications for JWST Surveys. *Astrophys. J.* **2012**, *754*, 120–135.
281. Satyapal, S.; Abel, N.P.; Secrest, N.J. Star-forming Galaxies as AGN Imposters? A Theoretical Investigation of the Mid-infrared Colors of AGNs and Extreme Starbursts. *Astrophys. J.* **2018**, *858*, 38–49. [[CrossRef](#)]
282. Donley, J.L.; Rieke, G.H.; Pérez-González, P.G.; Barro, G. Spitzer’s Contribution to the AGN Population. *Astrophys. J.* **2008**, *687*, 111–132. [[CrossRef](#)]
283. Mendez, A.J.; Coil, A.L.; Aird, J.; Diamond-Stanic, A.M.; Moustakas, J.; Blanton, M.R.; Cool, R.J.; Eisenstein, D.J.; Wong, K.C.; Zhu, G. PRIMUS: Infrared and X-Ray AGN Selection Techniques at $0.2 < z < 1.2$. *Astrophys. J.* **2013**, *770*, 40–64.
284. Ananna, T.T.; Treister, E.; Urry, C.M.; Ricci, C.; Kirkpatrick, A.; LaMassa, S.; Buchner, J.; Civano, F.; Tremmel, M.; Marchesi, S. The Accretion History of AGNs. I. Supermassive Black Hole Population Synthesis Model. *Astrophys. J.* **2019**, *871*, 240–262. [[CrossRef](#)]
285. Yang, G.; Papovich, C.; Bagley, M.B.; Buat, V.; Burgarella, D.; Dickinson, M.; Elbaz, D.; Finkelstein, S.L.; Fontana, A.; Grogin, N.A.; et al. JWST/MIRI Simulated Imaging: Insights into Obscured Star Formation and AGNs for Distant Galaxies in Deep Surveys. *Astrophys. J.* **2021**, *908*, 144–170. [[CrossRef](#)]
286. Stalevski, M.; Ricci, C.; Ueda, Y.; Lira, P.; Fritz, J.; Baes, M. The dust covering factor in active galactic nuclei. *Mon. Not. R. Astron. Soc.* **2016**, *458*, 2288–2302. [[CrossRef](#)]
287. Leja, J.; Johnson, B.D.; Conroy, C.; van Dokkum, P.G.; Byler, N. Deriving Physical Properties from Broadband Photometry with Prospector: Description of the Model and a Demonstration of its Accuracy Using 129 Galaxies in the Local Universe. *Astrophys. J.*, **2017**, *837*, 170–204. [[CrossRef](#)]
288. Rujopakarn, W.; Rieke, G.H.; Eisenstein, D.J.; Juneau, S. Morphology and Size Differences Between Local and High-redshift Luminous Infrared Galaxies. *Astrophys. J.* **2011**, *726*, 93–103. [[CrossRef](#)]
289. Rujopakarn, W.; Rieke, G.H.; Weiner, B.J.; Pérez-González, P.; Rex, M.; Walth, G.L.; Kartaltepe, J.S. Mid-infrared Determination of Total Infrared Luminosity and Star Formation Rates of Local and High-redshift Galaxies. *Astrophys. J.* **2013**, *767*, 73–87. [[CrossRef](#)]
290. Shipley, H.V.; Papovich, C.; Rieke, G.H.; Brown, M.J.I.; Moustakas, J. A New Star Formation Rate Calibration from Polycyclic Aromatic Hydrocarbon Emission Features and Application to High-redshift Galaxies. *Astrophys. J.* **2016**, *818*, 60–79. [[CrossRef](#)]
291. Hunt, L.K.; Thuan, T.X.; Izotov, Y.I.; Sauvage, M. The Spitzer View of Low-Metallicity Star Formation. III. Fine-Structure Lines, Aromatic Features, and Molecules. *Astrophys. J.* **2010**, *712*, 164–187. [[CrossRef](#)]
292. Secrest, N.J.; Satyapal, S. A Low Incidence of Mid-infrared Variability in Dwarf Galaxies. *Astrophys. J.* **2020**, *900*, 56–63. [[CrossRef](#)]
293. Kozłowski, S.; Kochanek, C.S.; Ashby, M.L.N.; Assef, R.J.; Brodwin, M.; Eisenhardt, P.R.; Jannuzi, B.T.; Stern, D. Quasar Variability in the Mid-Infrared. *Astrophys. J.* **2016**, *817*, 119–132. [[CrossRef](#)]
294. García-González, J.; Alonso-Herrero, A.; Pérez-González, P.G.; Hernán-Caballero, A.; Sarajedini, V.L.; Villar, V. Selection of AGN candidates in the GOODS-South Field through Spitzer/MIPS 24 μm variability. *Mon. Not. R. Astron. Soc.* **2015**, *446*, 3199–3223. [[CrossRef](#)]
295. Kozłowski, S.; Kochanek, C.S.; Stern, D.; Ashby, M.L.N.; Assef, R.J.; Bock, J.J.; Borys, C.; Brand, K.; Brodwin, M.; Brown, M.J.I.; et al. Mid-infrared Variability from the Spitzer Deep Wide-field Survey. *Astrophys. J.* **2010**, *716*, 530–543. [[CrossRef](#)]
296. Ward, C.; Gezari, S.; Nugent, P.; Bellm, E.C.; Dekany, R.; Drake, A.; Duev, D.A.; Graham, M.J.; Kasliwal, M.M.; Kool, E.C.; et al. Variability-selected intermediate mass black hole candidates in dwarf galaxies from ZTF and WISE. *arXiv* **2021**, arXiv:2110.13098.

297. Elmer, E.; Almaini, O.; Merrifield, M.; Hartley, W.G.; Maltby, D.T.; Lawrence, A.; Botti, I.; Hirst, P. Long-term NIR variability in the UKIDSS Ultra Deep Survey: A new probe of AGN activity at high redshift. *Mon. Not. R. Astron. Soc.* **2020**, *493*, 3026–3035. [[CrossRef](#)]
298. Sheng, Z.; Wang, T.; Jiang, N.; Yang, C.; Yan, L.; Dou, L.; Peng, B. Mid-infrared Variability of Changing-look AGNs. *Astrophys. J. Lett.* **2017**, *846*, L7–L13. [[CrossRef](#)]
299. LaMassa, S.M.; Cales, S.; Moran, E.C.; Myers, A.D.; Richards, G.T.; Eracleous, M.; Heckman, T.M.; Gallo, L.; Urry, C. M. The Discovery of the First “Changing Look” Quasar: New Insights Into the Physics and Phenomenology of Active Galactic Nucleus. *Astrophys. J.* **2015**, *800*, 144–153. [[CrossRef](#)]
300. Stern, D. McKernan, B.; Graham, M.J.; Ford, K.E.S.; Ross, N.P.; Meisner, A.M.; Assef, R.J.; Baloković, M.; Brightman, M.; Dey, A.; et al. A Mid-IR Selected Changing-look Quasar and Physical Scenarios for Abrupt AGN Fading. *Astrophys. J.* **2018**, *864*, 27–35. [[CrossRef](#)]
301. Sheng, Z.; Wang, T.; Jiang, N.; Ding, J.; Cai, Z.; Guo, H.; Sun, L.; Dou, L.; Yang, C. Initial Results from a Systematic Search for Changing-look Active Galactic Nuclei Selected via Mid-infrared Variability. *Astrophys. J.* **2020**, *889*, 46–54. [[CrossRef](#)]
302. Pouliaxis, E. Identification of Active Galactic Nuclei through Different Selection Techniques. Ph.D. Thesis, National and Kapodistrian University of Athens, Athens, Greece, February 2020.
303. Hagan, J.B.; Rieke, G.H.; Fox, O.D.; Noriega-Crespo, A.; Hines, D.C.; Cracraft, M.; García Marín, M. Cosmic-ray-related Signals from Detectors in Space: The Spitzer/IRAC Si:As IBC Devices. *Publ. Astron. Soc. Pac.* **2021**, *133*, 40–70. [[CrossRef](#)]
304. Viaene, S.; Nersesian, A.; Fritz, J.; Verstocken, S.; Baes, M.; Bianchi, S.; Casasola, V.; Cassarà, L.; Clark, C.; Davies, J.; et al. High-resolution, 3D radiative transfer modelling. IV. AGN-powered dust heating in NGC 1068. *Astron. Astrophys.* **2020**, *638*, 150–166. [[CrossRef](#)]
305. Hönig, S.F.; Kishimoto, M. Dusty Winds in Active Galactic Nuclei: Reconciling Observations with Models. *Astrophys. J. Lett.* **2017**, *838*, 20–25. [[CrossRef](#)]
306. Williamson, D.; Hönig, S.; Venanzi, M. Radiation Hydrodynamics Models of Active Galactic Nuclei: Beyond the Central Parsec. *Astrophys. J.* **2020**, *897*, 26–45. [[CrossRef](#)]
307. Maiolino, R.; Mannucci, F. De re metallica: The cosmic chemical evolution of galaxies. *ARAA* **2019**, *27*, 3–141. [[CrossRef](#)]
308. Laha, S.; Markowitz, A.G.; Krumpe, M.; Nikutta, R.; Rothschild, R.; Saha, T. The Variable and Non-variable X-ray Absorbers in Compton-thin Type II Active Galactic Nuclei. *Astrophys. J.* **2020**, *897*, 55–120. [[CrossRef](#)]
309. Markowitz, A.G.; Krumpe, M.; Nikutta, R. First X-ray-based statistical tests for clumpy-torus models: Eclipse events from 230 years of monitoring of Seyfert AGN. *Mon. Not. R. Astron. Soc.* **2014**, *439*, 1403–1458. [[CrossRef](#)]
310. Buchner, J.; Brightman, M.; Nandra, K.; Nikutta, R.; Bauer, F.E. X-ray spectral and eclipsing model of the clumpy obscurer in active galactic nuclei. *Astron. Astrophys.* **2019**, *629*, 16–29. [[CrossRef](#)]
311. Poncelet, A.; Perrin, G.; Sol, H. A new analysis of the nucleus of NGC 1068 with MIDI observations. *Astron. Astrophys.* **2006**, *450*, 483–494. [[CrossRef](#)]
312. Krolik, J.H.; Begelman, M.C. Molecular Tori in Seyfert Galaxies: Feeding the Monster and Hiding It. *Astrophys. J.* **1988**, *329*, 702–711. [[CrossRef](#)]
313. Tsuboi, M.; Kitamura, Y.; Uehara, K.; Tsutsumi, T.; Miyawaki, R.; Miyoshi, M.; Miyazaki, A. ALMA view of the circumnuclear disk of the Galactic Center: Tidally disrupted molecular clouds falling to the Galactic Center. *PASJ* **2018**, *70*, 85–115. [[CrossRef](#)]
314. Alonso-Herrero, A.; Ramos, Almeida, C.; Mason, R.; Asensio Ramos, A.; Roche, P.F.; Levenson, N.A.; Elitzur, M.; Packham, C.; Rodríguez Espinosa, J.M.; Young, S.; et al. Torus and Active Galactic Nucleus Properties of Nearby Seyfert Galaxies: Results from Fitting Infrared Spectral Energy Distributions and Spectroscopy. *Astrophys. J.* **2011**, *736*, 82–111. [[CrossRef](#)]
315. Ramos Almeida, C.; Levenson, N.A.; Rodríguez Espinosa, J.M.; Alonso-Herrero, A.; Asensio Ramos, A.; Radomski, J.T.; Packham, C.; Fisher, R.S.; Telesco, C.M. The Infrared Nuclear Emission of Seyfert Galaxies on Parsec Scales: Testing the Clumpy Torus Models. *Astrophys. J.* **2009**, *702*, 1127–1149. [[CrossRef](#)]
316. Ramos Almeida, C.; Levenson, N.A.; Alonso-Herrero, A.; Asensio Ramos, A.; Rodríguez Espinosa, J.M.; Pérez García, A.M.; Packham, C.; Mason, R.; Radomski, J.T.; Díaz-Santos, T. Testing the Unification Model for Active Galactic Nuclei in the Infrared: Are the Obscuring Tori of Type 1 and 2 Seyferts Different? *Astrophys. J.* **2011**, *731*, 92–115. [[CrossRef](#)]
317. Hernán-Caballero, A.; Hatziminaoglou, E.; Alonso-Herrero, A.; Mateos, S. The near-to-mid infrared spectrum of quasars. *Mon. Not. R. Astron. Soc.* **2016**, *463*, 2064–2078. [[CrossRef](#)]
318. Mor, R.; Netzer, H.; Elitzur, M. Dusty Structure Around Type-I Active Galactic Nuclei: Clumpy Torus Narrow-line Region and Near-nucleus Hot Dust. *Astrophys. J.* **2009**, *705*, 298–313. [[CrossRef](#)]
319. Swain, S.; Shalima, P.; Latha, K.V.P.; Swamy, K.B.S. Hot graphite dust in the inner regime of NGC 4151. *Mon. Not. R. Astron. Soc.* **2021**, *503*, 5877–5893. [[CrossRef](#)]
320. García-González, J.; Alonso-Herrero, A.; Hönig, S.F.; Hernán-Caballero, A.; Ramos Almeida, C.; Levenson, N.A.; Roche, P.F.; González-Martín, O.; Packham, C.; Kishimoto, M. A mid-infrared statistical investigation of clumpy torus model predictions. *Mon. Not. R. Astron. Soc.* **2017**, *470*, 2578–2598. [[CrossRef](#)]
321. Hönig, S.F.; Kishimoto, M. Constraining properties of dusty environments by infrared variability. *Astron. Astrophys.* **2011**, *534*, 121–128. [[CrossRef](#)]
322. Nikutta, R.; Lopez-Rodríguez, E.; Ichikawa, K.; Levenson, N.A.; Packham, C.; Hönig, S.F.; Alonso-Herrero, A. Hypercubes of AGN Tori (HYPERCAT). II. Resolving the Torus with Extremely Large Telescopes. *Astrophys. J.* **2021**, *923*, 127–143. [[CrossRef](#)]

323. Elitzur, M. The toroidal obscuration of active galactic nuclei. *New Astron. Rev.* **2008**, *52*, 274–288. [[CrossRef](#)]
324. Victoria-Ceballos, C.I.; González-Martín, O.; Fritz, J.; Ramos Almeida, C.; López-Rodríguez, E.; García-Burillo, S.; Alonso-Herrero, A.; Martínez-Paredes, M.; Esparza-Arredondo, D.; Osorio-Clavijo, N. The Complex Infrared Dust Continuum Emission of NGC 1068: Ground-based N- and Q-band Spectroscopy and New Radiative Transfer Models. *ApJ* **2022**, *926*, 192–211 [[CrossRef](#)]
325. Wada, K. Radiation-driven Fountain and Origin of Torus around Active Galactic Nuclei. *Astrophys. J.* **2012**, *758*, 66. [[CrossRef](#)]
326. Namekata, D.; Umemura, M. Sub-parsec-scale dynamics of a dusty gas disc exposed to anisotropic AGN radiation with frequency-dependent radiative transfer. *Mon. Not. R. Astron. Soc.* **2016**, *460*, 980–1018. [[CrossRef](#)]
327. Takasao, S.; Shuto, Y.; Wada, K. Spontaneous Formation of Outflows Powered by Rotating Magnetized Accretion Flows in a Galactic Center. *Astrophys. J.* **2022**, *926*, 50–70. [[CrossRef](#)]
328. Venanzi, M.; Hönic, S.; Williamson, D. The Role of Infrared Radiation Pressure in Shaping Dusty Winds in AGNs. *Astrophys. J.* **2020**, *900*, 174–185. [[CrossRef](#)]
329. Vollmer, B.; Schartmann, M.; Burtscher, L.; Marin, F.; Hönic, S.; Davies, R.; Goosmann, R. Thick turbulent gas disks with magnetocentrifugal winds in active galactic nuclei. Model infrared emission and optical polarization. *Astron. Astrophys.* **2018**, *615*, 164–196. [[CrossRef](#)]
330. Stalewski, M.; Tristram, K.R.W.; Asmus, D. Dissecting the active galactic nucleus in Circinus–II. A thin dusty disc and a polar outflow on parsec scales. *Mon. Not. R. Astron. Soc.* **2019**, *484*, 3334–3355. [[CrossRef](#)]
331. Wang, J.-M.; Du, P.; Brotherton, M.S.; Hu, C.; Songsheng, Y.-Y.; Li, Y.-R.; Shi, Y.; Zhang, Z.-X. Tidally disrupted dusty clumps as the origin of broad emission lines in active galactic nuclei. *Nat. Astron.* **2017**, *1*, 775–783. [[CrossRef](#)]
332. Khrykin, I.; Hennawi, J.F.; Worseck, G.; Davies, F.B. The first measurement of the quasar lifetime distribution. *Mon. Not. R. Astron. Soc.* **2021**, *505*, 649–662. [[CrossRef](#)]
333. Hönic, S.F. Redefining the Torus: A Unifying View of AGNs in the Infrared and Submillimeter. *Astrophys. J.* **2019**, *884*, 171–183. [[CrossRef](#)]
334. Hopkins, P.F.; Hernquist, L.; Cox, T.J.; Di Matteo, T.; Robertson, B.; Springel, V. A Unified, Merger-driven Model of the Origin of Starbursts, Quasars, the Cosmic X-Ray Background, Supermassive Black Holes, and Galaxy Spheroids. *ApJS* **2006**, *163*, 1–49. [[CrossRef](#)]
335. Sanders, D.B.; Soifer, B.T.; Elias, J.H.; Madore, B.F.; Matthews, K.; Neugebauer, G.; Scoville, N.Z. Ultraluminous Infrared Galaxies and the Origin of Quasars. *Astrophys. J.* **1988**, *325*, 74. [[CrossRef](#)]
336. Ricci, C.; Privon, G.C.; Pfeifle, R.W.; Armus, L.; Iwasawa, K.; Torres-Albà, N.; Satyapal, S.; Bauer, F.E.; Treister, E.; Ho, L.C.; et al. A hard X-ray view of luminous and ultra-luminous infrared galaxies in GOALS–I. AGN obscuration along the merger sequence. *Mon. Not. R. Astron. Soc.* **2021**, *506*, 5935–5950. [[CrossRef](#)]
337. Hopkins, P.F.; Hayward, C.C.; Narayanan, D.; Hernquist, L. The origins of active galactic nuclei obscuration: The ‘torus’ as a dynamical, unstable driver of accretion. *Mon. Not. R. Astron. Soc.* **2012**, *420*, 320–339. [[CrossRef](#)]
338. Hopkins, P.F.; Torrey, P.; Faucher-Giguère, C.-A.; Quataert, E.; Murray, N. Stellar and quasar feedback in concert: Effects on AGN accretion, obscuration, and outflows. *Mon. Not. R. Astron. Soc.* **2016**, *458*, 816–831. [[CrossRef](#)]
339. Trebitsch, M.; Volonteri, M.; Dubois, Y. Black hole obscuration and duty-cycles mediated by AGN feedback in high-redshift galaxies. *Mon. Not. R. Astron. Soc.* **2019**, *487*, 819–831. [[CrossRef](#)]